

AD-A151 059

EFFECTS OF STRUCTURAL AND STRESS ANISOTROPY ON VELOCITY  
OF LOW-AMPLITUDE (U) TEXAS UNIV AT AUSTIN GEOTECHNICAL  
ENGINEERING CENTER S H LEE ET AL JUN 84

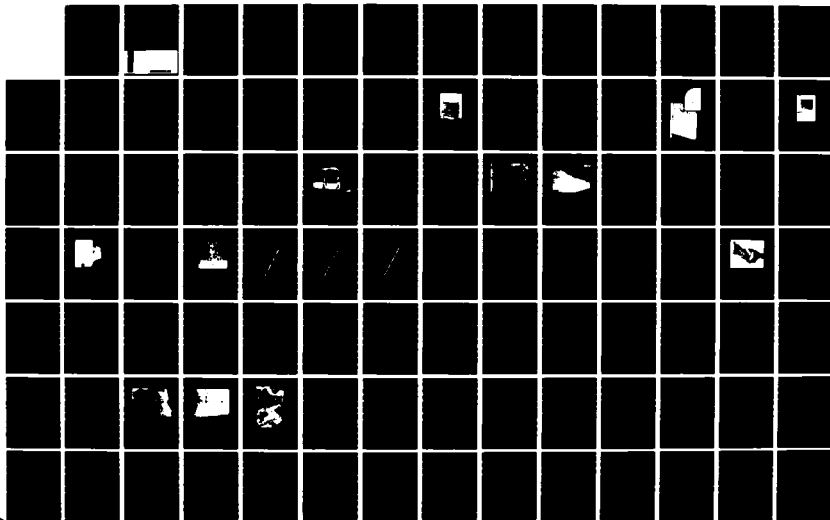
1/2

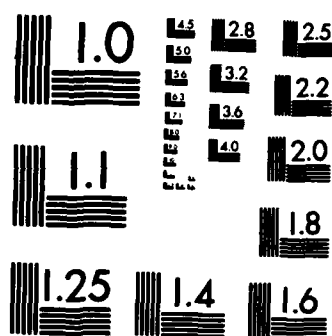
UNCLASSIFIED

AFOSR-TR-85-0089 AFOSR-83-0062

F/G 8/13

NL





MICROCOPY RESOLUTION TEST CHART  
NATIONAL BUREAU OF STANDARDS-1963-A

2

ETH

EFFECTS OF STRUCTURAL AND STRESS ANISOTROPY ON  
VELOCITY OF LOW-AMPLITUDE COMPRESSION WAVES  
PROPAGATING ALONG  
PRINCIPAL STRESS DIRECTIONS IN DRY SAND

AD-A151 059

HERBERT YIU-FAI CHU  
SHANNON HSIEN-HENG LEE  
supervised by  
KENNETH H. STOKOE, II

a report on research  
sponsored by  
United States Air Force  
Office of Scientific Research  
Bolling Air Force Base

DTIC  
ELECTE  
FEB 28 1985  
A

Approved for public release;  
distribution unlimited.

DTIC FILE COPY

85 02 13 030

# REPORT DOCUMENTATION PAGE

1a. REPORT SECURITY CLASSIFICATION <b>UNCLASSIFIED</b>		1b. RESTRICTIVE MARKINGS	
2a. SECURITY CLASSIFICATION AUTHORITY		3. DISTRIBUTION/AVAILABILITY OF REPORT Approved for Public Release; Distribution Unlimited.	
2b. DECLASSIFICATION/DOWNGRADING SCHEDULE			
4. PERFORMING ORGANIZATION REPORT NUMBER(S)		5. MONITORING ORGANIZATION REPORT NUMBER(S) <b>AFOSR-TR- 85 - 0089</b>	
6a. NAME OF PERFORMING ORGANIZATION UNIVERSITY OF TEXAS, AUSTIN	6b. OFFICE SYMBOL (If applicable)	7a. NAME OF MONITORING ORGANIZATION <i>Same as #8</i>	
6c. ADDRESS (City, State and ZIP Code) DEPARTMENT OF CIVIL ENGINEERING AUSTIN, TEXAS 78712		7b. ADDRESS (City, State and ZIP Code)	
8a. NAME OF FUNDING/SPONSORING ORGANIZATION AIR FORCE OFFICE OF SCIENTIFIC RESEARCH	8b. OFFICE SYMBOL (If applicable) AFOSR/NA	9. PROCUREMENT INSTRUMENT IDENTIFICATION NUMBER (AFOSR-83-0062)	
8c. ADDRESS (City, State and ZIP Code) BOLLING AFB, DC 20332		10. SOURCE OF FUNDING NOS.	
		PROGRAM ELEMENT NO. 61102F	PROJECT NO. 2307
		TASK NO. C1	WORK UNIT NO.
11. TITLE (Include Security Classification) EFFECTS OF STRUCTURAL AND STRESS ANISOTROPY ON VELOCITY OF LOW-AMPLITUDE COMPRESSION ...		UNCLASSIFIED	
12. PERSONAL AUTHOR(S) SHANNON HSIEN-HENG LEE, HERBERT YIU-FAI CHU, and KENNETH H. STOKOE, II			
13a. TYPE OF REPORT ANNUAL	13b. TIME COVERED FROM 2-1-83 TO 2-15-84	14. DATE OF REPORT (Yr., Mo., Day) June 1984	15. PAGE COUNT 176
16. SUPPLEMENTARY NOTATION			
17. COSATI CODES		18. SUBJECT TERMS (Continue on reverse if necessary and identify by block number)	
FIELD	GROUP	SUB. GR.	
19. ABSTRACT (Continue on reverse if necessary and identify by block number) A 7-ft cubical sample of dry sand was tested using the triaxial testing device constructed by Kopperman et al (1982) and Knox et al (1982). The sand was the same as that used used by Kopperman and Knox. A new raining device was fabricated and used to construct this sand sample which resulted in a more uniform sample than prepared earlier. Improvements were also made to the excitation ports in order to have better control.  Extensive tests were performed under the following different stress states: isotropic, biaxial and triaxial. In each case, velocities of P-waves propagating along all principal stress directions were measured. Results from these tests lead to the following conclusions: 1. the effect of stress history on P-wave velocity is negligible, 2. the sample can be treated as a cross-anisotropic material under isotropic confinement due to structural anisotropy, 3. complete anisotropy resulted			
20. DISTRIBUTION/AVAILABILITY OF ABSTRACT UNCLASSIFIED/UNLIMITED <input checked="" type="checkbox"/> SAME AS RPT. <input type="checkbox"/> DTIC USERS <input type="checkbox"/>		21. ABSTRACT SECURITY CLASSIFICATION <b>UNCLASSIFIED</b>	
22a. NAME OF RESPONSIBLE INDIVIDUAL Lt Col Lawrence D Hokanson		22b. TELEPHONE NUMBER (Include Area Code) 202/767-4935	22c. OFFICE SYMBOL AFOSR/NA

UNCLASSIFIED

by the coupling of stress anisotropy and structural anisotropy, and 4. P-wave velocity depends on the principal effective stress in the direction of propagation, with principal stresses perpendicular to the direction of propagation having a negligible effect on velocity.

UNCLASSIFIED

EFFECTS OF STRUCTURAL AND STRESS ANISOTROPY ON VELOCITY OF  
LOW-AMPLITUDE COMPRESSION WAVES PROPAGATING ALONG  
PRINCIPAL STRESS DIRECTIONS IN DRY SAND

HERBERT YIU-FAI CHU

SHANNON HSIEN-HENG LEE

supervised by

KENNETH H. STOKOE, II

a report on research

sponsored by

United States Air Force

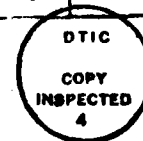
Office of Scientific Research

Bolling Air Force Base

Accession For	
NTIS GRA&I	<input checked="checked" type="checkbox"/>
DTIC TAB	<input type="checkbox"/>
Unannounced	<input type="checkbox"/>
Justification	
Distribution/	
Availability Codes	
Avail and/or	
Dist	Special

June, 1984

Geotechnical Engineering Report GR84-6  
Geotechnical Engineering Center  
Civil Engineering Department  
The University of Texas at Austin  
Austin, Texas



AIR FORCE OFFICE OF SCIENTIFIC RESEARCH (AFSC)  
NOTICE OF TRANSMITTAL TO DTIC  
This technical report has been reviewed and is  
approved for public release IAW AFR 190-12.  
Distribution is unlimited.  
MATTHEW J. KERPER  
Chief, Technical Information Division

## ACKNOWLEDGMENTS

The writer wishes to acknowledge the following people for their invaluable assistance in this project:

- Dr. Jose M. Roeset for his assistance and advice.
- Ms. Lisa C. Merrit and Mrs. Teresa Tice-Boggs for typing and aid in the completion of this thesis on time.
- Mr. Fred Redd for drafting.
- fellow graduate students, especially Stuart E. Kopperman, David P. Knox, Tony S. Kwok and James Bierschwale,
- staff of the Phil Ferguson Laboratory, Balcones Research Center, University of Texas at Austin, especially Mrs. Laurie Goldin,
- technical staff of the Department of Civil Engineering, University of Texas at Austin, especially James Stewart, Marvin Howse and Tom Phillips,
- the United States Air Force Office of Scientific Research (AFQSR), Bolling Air Force Base, Washington, D.C., for supporting this research under grant AFQSR 83-0062, Major Jhon J. Allen was the initial project manager, and then Lt. Col. Dale Kokanson was the project manager.

## ABSTRACT

A 7-ft cubical sample of dry sand was tested using the tri-axial testing device constructed by Kopperman et al (1982) and Knox et al (1982). The sand was the same as that used by Kopperman and Knox. A new raining device was fabricated and used to construct this sand sample which resulted in a more uniform sample than prepared earlier. Improvements were also made to the excitation ports in order to have better control of the stress states.

Extensive tests were performed under the following different stress states: isotropic, biaxial and triaxial. In each case, velocities of P-waves propagating along all principal stress directions were measured. Results from these tests lead to the following conclusions:

1. the effect of stress history on P-wave velocity is negligible,
2. the sample can be treated as a cross-anisotropic material under isotropic confinement due to structural anisotropy,
3. complete anisotropy resulted by the coupling of stress anisotropy and structural anisotropy,
- and 4. P-wave velocity depends on the principal effective stress in the direction of propagation, with principal stresses perpendicular to the direction of propagation having a negligible effect on velocity.



## TABLE OF CONTENTS

	Page
ACKNOWLEDGEMENTS . . . . .	iv
ABSTRACT . . . . .	v
TABLE OF CONTENTS . . . . .	vi
LIST OF TABLES . . . . .	x
LIST OF FIGURES . . . . .	xi
CHAPTER 1. INTRODUCTION . . . . .	1
1.1 BACKGROUND INFORMATION . . . . .	1
1.2 PRESENT TESTING . . . . .	11
CHAPTER 2. IMPROVEMENTS OF TESTING FACILITIES . . . . .	14
2.1 INTRODUCTION . . . . .	14
2.2 STORAGE OF SAND . . . . .	15
2.3 SOIL PALCEMENT . . . . .	17
2.4 EXCITATION PORTS . . . . .	22
2.5 MONITORING AND RECORDING SYSTEM . . . . .	32
.1 Digital Oscilloscopes . . . . .	33
.2 Accelerometers . . . . .	33
.3 Accelerometer Blocks . . . . .	34
.4 Charge Amplifiers . . . . .	38
.5 Stress Cells . . . . .	40
.6 Strain Sensors . . . . .	42
2.6 SUMMARY . . . . .	46

	Page
CHAPTER 3. TESTING PROGRAM AND PROCEDURES . . . . .	49
3.1 INTRODUCTION . . . . .	49
3.2 EMPTYING OF THE TRIAXIAL DEVICE . . . . .	50
3.3 SAMPLE CONSTRUCTION . . . . .	52
3.4 DYNAMIC TESTING . . . . .	61
3.5 COMPRESSION WAVE ANALYSIS . . . . .	67
.1 Determination of Propagation Velocity . . .	67
.2 Determination of Predominant Frequency . .	70
.3 Determination of Peak Acceleration . . . .	72
.4 Determination of Strain Amplitude . . . . .	73
.5 Determination of Wavelengths . . . . .	74
3.6 SUMMARY . . . . .	76
CHAPTER 4. ISOTROPIC CONFINEMENT . . . . .	77
4.1 INTRODUCTION . . . . .	77
4.2 EFFECT OF STRESS HISTORY . . . . .	80
4.3 EFFECT OF STRUCTURAL ANISOTROPY . . . . .	84
4.4 EFFECT OF ISOTROPIC CONFINEMENT . . . . .	87
4.5 SUMMARY . . . . .	89
CHAPTER 5. STRESS-STRAIN BEHAVIOR AND CROSS-ANISOTROPIC MODEL	94
5.1 INTRODUCTION . . . . .	94
5.2 NOTATION FOR STRESSES, STRAINS AND WAVE VELOCITIES . . . . .	95
5.3 PERFORMANCE OF STRESS CELLS . . . . .	100

	Page
5.4 PERFORMANCE OF STRAIN SENSORS . . . . .	105
5.5 CROSS-ANISOTROPY . . . . .	107
.1 Evaluation of Constants by Stress-Strain Data and Wave Velocities . . . . .	109
.2 Estimation of Constants by Wave Velocities . . . . .	113
5.6 SUMMARY . . . . .	115
CHAPTER 6. BIAXIAL CONFINEMENT . . . . .	117
6.1 INTRODUCTION . . . . .	117
6.2 VARIATION OF STRESS IN ONE PRINCIPAL DIRECTION . . . . .	123
.1 Effect of Stress History . . . . .	123
.2 Effect of Structural Anisotropy . . . . .	126
.3 Effect of Biaxial Confinement . . . . .	128
.4 Effect of Intermediate Principal Effective Stress . . . . .	134
6.3 VARIATION OF STRESS IN TWO PRINCIPAL DIRECTIONS . . . . .	136
6.4 SUMMARY . . . . .	140
CHAPTER 7. TRIAXIAL CONFINEMENT . . . . .	147
7.1 INTRODUCTION . . . . .	147
7.2 VARIATION OF STRESS IN ONE PRINCIPAL DIRECTION . . . . .	149
.1 Effect of Intermediate Principal Stress . . . . .	150
7.3 VARIATION OF STRESS IN TWO PRINCIPAL DIRECTIONS . . . . .	152
.1 Effect of Major and Minor Principal Stresses . . . . .	152
7.4 VARIATION OF STRESS IN ALL PRINCIPAL DIRECTIONS . . . . .	153
.1 Effect of Principal Stresses . . . . .	155
7.5 SUMMARY . . . . .	158

	Page
CHAPTER 8. SUMMARY AND CONCLUSIONS . . . . .	161
8.1 SUMMARY . . . . .	161
8.2 CONCLUSIONS . . . . .	162
APPENDIX A. STRAIN CALIBRATION FOR STRAIN SENSOR . . . . .	166

## LIST OF TABLES

Table		Page
3.1	Densities and Void Ratios of Sand at Various Elevations in the Triaxial Device . . . . .	60
3.2	Loading Pressure Sequences . . . . .	62
3.3	Distances Between Accelerometers Inside the Triaxial Device . . . . .	68
4.1	Compression Wave Velocities Measured at Different Times Under Similar Isotropic States of Stress . . .	83
4.2	Comparison of Constants and Slopes for Equation 4.2 with Those Reported by Kopperman et al (1982) . . . .	91
6.1	Comparison of Constants and Slopes for Equations Relating $V_p$ to $\bar{\sigma}_o$ for Isotropic Confinement and $V_p$ to $\bar{\sigma}_a$ for Biaxial Confinement with Variation of Stress in One Principal Direction . . . . .	132
6.2	Comparison of Constants and Slopes for Equations Relating $V_p$ to $\bar{\sigma}_a$ for Isotropic Confinement and $V_p$ to $\bar{\sigma}_a$ for Biaxial Confinement with Variation of Stress in Two Principal Directions . . . . .	141
6.3	Comparison of Constants and Slopes for Eq. 6.1 Relating $V_p$ to $\bar{\sigma}_a$ for Biaxial Confinement with Those Reported by Kopperman et al (1982) . . . . .	146
7.1	Comparison of Constants and Slopes for Equations Relating $V_p$ to $\bar{\sigma}_o$ for Isotropic Confinement and $V_p$ to $\bar{\sigma}_a$ for Triaxial Confinement . . . . .	160
8.1	Summary of Constants and Slopes for Eq. 8.2 Relating $V_p$ to $\bar{\sigma}_a$ for Various Confinements . . . . .	165

## LIST OF FIGURES

Figure		Page
1.1	Cut-Away, Isometric View of Triaxial Device Showing Top Reinforcement Details (From Kopperman et al, 1982) . . . . .	2
1.2	Isometric View of Triaxial Device Showing Side Reinforcement Details (From Kopperman et al, 1982). .	3
1.3	Completed Triaxial Device (From Kopperman et al, 1982)	4
1.4	Schematic Diagram of Triaxial Device and Associated Systems (After Kopperman et al, 1982) . . . . .	6
1.5	Membrane Used to Apply Load to Sand Specimen in Triaxial Device (From Kopperman et al, 1982) . . . .	8
1.6	Schematic of Air/Water System Used to Pressurize Membranes (From Kopperman et al, 1982) . . . . .	9
1.7	Panel Board Used to Pressurize Membranes in Triaxial Device (From Kopperman et al, 1982) . . . . .	10
1.8	Schematic of Monitoring and Recording Systems (After Kopperman et al, 1982) . . . . .	12
2.1	Completed Storage Bin . . . . .	16
2.2	View of New Rainer Loaded with Sand and in Place for Raining . . . . .	19
2.3	Raining Sand into Triaxial Device Using New Rainer	20
2.4	Top View of New Rainer . . . . .	21
2.5	Clamping Tool and Excitation Port . . . . .	24
2.6	Completed Excitation Port In Place . . . . .	26

Figure		Page
2.7	Set-Up for Calibrating Strain Gages on Each Excitation Port . . . . .	28
2.8	Calibration Curve for Strain Gages on TB Excitation Port . . . . .	29
2.9	Calibration Curve for Strain Gages on NS Excitation Port . . . . .	30
2.10	Calibration Curve for Strain Gages on EW Excitation Port . . . . .	31
2.11	Schematic View of Instrumentation Locations . . . . .	35
2.12	Accelerometer Being Assembled in Aluminum Accelerometer Block Which is Part of NS Excitation Port . . . . .	37
2.13	Accelerometer Block Used to Monitor Oblique Shear Waves . . . . .	39
2.14	Electric Set-Up for Calibrating Endevco Model 2735 Charge Amplifiers . . . . .	41
2.15	Calibration Curve for Stress Cell SS-1 . . . . .	43
2.16	Calibration Curve for Stress Cell SS-2 . . . . .	44
2.17	Calibration Curve for Stress Cell SS-3 . . . . .	45
2.18	Strain Calibration for Strain Sensor SN-1 . . . . .	47
3.1	Instrumentation at Mid-Depth Plane in Triaxial Device	54
3.2	Instruments Being Placed at the Mid-Depth Plane . . .	55
3.3	View Showing Stress Cells in North-South Direction	56
3.4	View of Working Platform Supported by Ropes Attached to Rainer . . . . .	57

Figure		Page
3.5	Locations of Density Measurements Performed During Filling of Triaxial Device . . . . .	59
3.6	Loading History in Each Principal Stress Direction from Start of Testing Until Membrane Raptured . . . . .	65
3.7	Loading History in Each Principal Stress Direction After New Membrane Installation . . . . .	66
3.8	Determination of Compression Wave Travel Times from a Set of Three Accelerometer Records . . . . .	69
3.9	Determination of Particle Amplitudes and Predominant Periods from a Typical Accelerometer Record . . . . .	71
4.1	Effect of Stress History on Variation of P-wave Velocity with Isotropic Confining Pressure . . . . .	82
4.2	Effect of Structural Anisotropy on Variation of P-wave Velocity with Isotropic Confining Pressure . . . . .	86
4.3	Comparison of P-wave Velocities with Results from Kopperman et al (1982) . . . . .	92
5.1	Orientation of Positive Stresses Acting on a Soil Element . . . . .	96
5.2	Notation Used to Describe Wave Velocities . . . . .	99
5.3	Comparison of Principal Stress Measured by Stress Cell SS-1 with Applied Stress in the Triaxial Device	101
5.4	Comparison of Principal Stress Measured by Stress Cell SS-2 with Applied Stress in the Triaxial Device	102
5.5	Comparison of Principal Stress Measured by Stress Cell SS-3 with Applied Stress in the Triaxial Device	103
5.6	Stress-Strain Behavior Along Each Principal Direction Under Isotropic Confinement . . . . .	106



Figure		Page
6.1	Initial Subset of First Series of Biaxial Confinement Tests with Variation of Stress in One Principal Direction . . . . .	119
6.2	Second Subset of First Series of Biaxial Confinement Tests with Variation of Stress in One Principal Direction . . . . .	120
6.3	Second Series of Biaxial Confinement Tests with Variation of Stresses in Two Principal Directions . .	121
6.4	Effect of Stress History on P-wave Velocity Under Biaxial Confinement with Variation of Stress in One Direction . . . . .	125
6.5	Effect of Structural Anisotropy on P-wave Velocities Under Biaxial Confinement with Variation of Stress in One Direction . . . . .	127
6.6	Variation in P-wave Velocities Under Biaxial Conditions for Stress Increasing Along z-direction	129
6.7	Variation in P-wave Velocities Under Biaxial Conditions for Stress Increasing Along x-direction	130
6.8	Variation in P-wave Velocities Under Biaxial Conditions for Stress Increasing Along y-direction	131
6.9	Effect of Complete Anisotropy on P-wave Velocities Under Biaxial Condition with Different Horizontal Confining Stresses . . . . .	135
6.10	Effect of Intermediate Principal Stress on $V_p$ with Stress Increasing Along the z-direction . . . . .	137
6.11	Effect of Intermediate Principal Stress on $V_p$ with Stress Increasing Along the x-direction . . . . .	138
6.12	Variation in P-wave Velocities Along Directions of Increasing Stress Under Biaxial Confinement with Two Principal Stresses Changing . . . . .	139

Figure		Page
6.13	Variation in P-wave Velocities Along Directions of Constant Stress Under Biaxial Confinement with Two Principal Stresses Changing . . . . .	142
6.14	Effect of Structural Anisotropy on $V_p$ Under Biaxial Confinement . . . . .	144
7.1	Loading Conditions for Triaxial Confinement Tests . .	148
7.2	Variation of Compression Wave Velocities Under Triaxial Confinement When Only One Principal Stress Varied . . . . .	151
7.3	Variation of Compression Wave Velocities Under Triaxial Confinement When Two Principal Stresses Varied . . . . .	154
7.4	Variation of Compression Wave Velocities Under Triaxial Confinement When All Principal Stresses Varied . . . . .	156
7.5	Comparison of Wave Velocities Under Isotropic and Triaxial Confinements . . . . .	159
A.1	Strain Calibration for Strain Sensor SN-2 . . . . .	167
A.2	Strain Calibration for Strain Sensor SN-3 . . . . .	168
A.3	Strain Calibration for Strain Sensor SN-4 . . . . .	169
A.4	Strain Calibration for Strain Sensor SN-5 . . . . .	170
A.5	Strain Calibration for Strain Sensor SN-6 . . . . .	171
A.6	Strain Calibration for Strain Sensor SN-7 . . . . .	172
A.7	Strain Calibration for Strain Sensor SN-8 . . . . .	173

## CHAPTER ONE

### INTRODUCTION

A large-scale triaxial testing device was designed and constructed during 1980 and 1981 under the sponsorship of a grant from the United States Air Force Office of Scientific Research (AFOSR). With this device, laboratory studies of the effects of isotropic, biaxial and triaxial states of stress on the velocity of compression and shear waves propagating through soil can be performed. An initial series of tests with dry sand was performed by Kopperman et al (1982) on compression waves and by Knox et al (1982) on shear waves. The objectives of the research reported herein are: 1. to check the validity of the conclusions reported by Kopperman et al on compression waves (P-waves), and 2. to extend this earlier work by performing additional tests under anisotropic states of stress.

#### 1.1 BACKGROUND INFORMATION

The triaxial testing device is essentially a reinforced steel box with interior dimensions of 7 ft (2.1 m) on each side. Sketches of the device are shown in Figs. 1.1 and 1.2, and the completed device is shown in Fig. 1.3. Equipment associated with the device is used to : 1. place sand into the device, 2. pressurize the

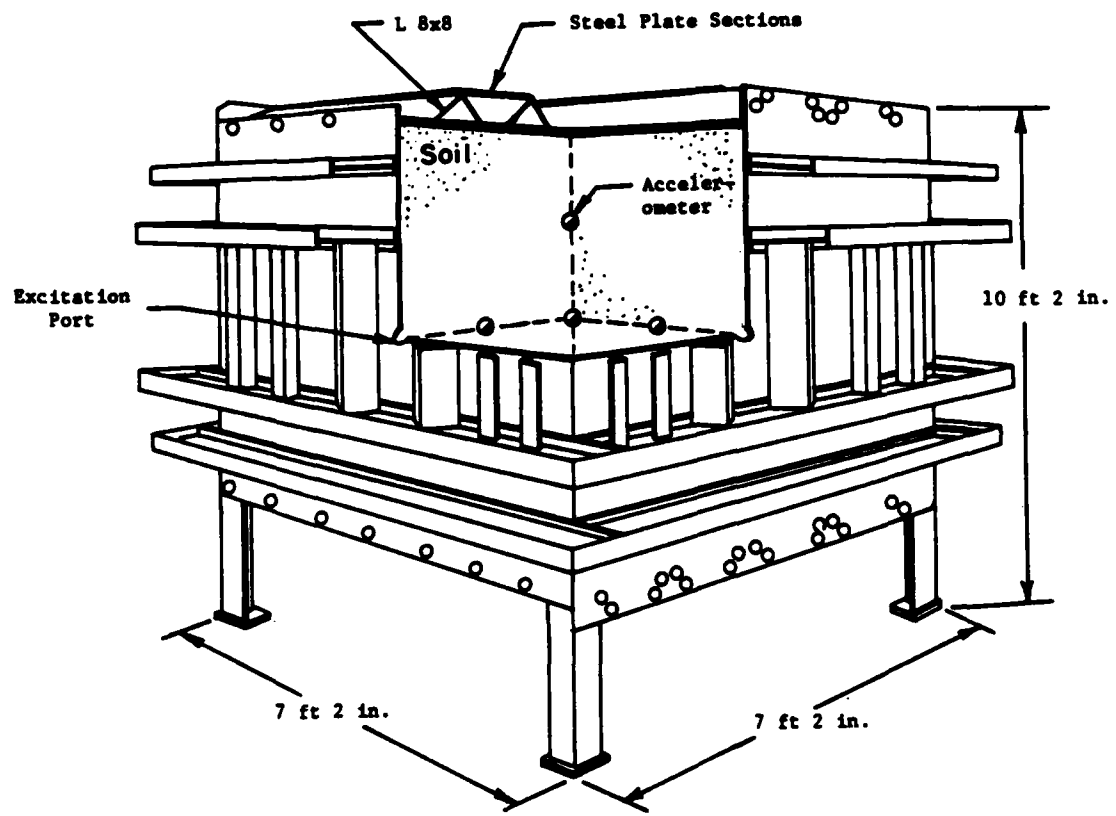


Fig. 1.1 - Cut-Away, Isometric View of Triaxial Device  
Showing Top Reinforcement Details (From  
Kopperman et al, 1982)

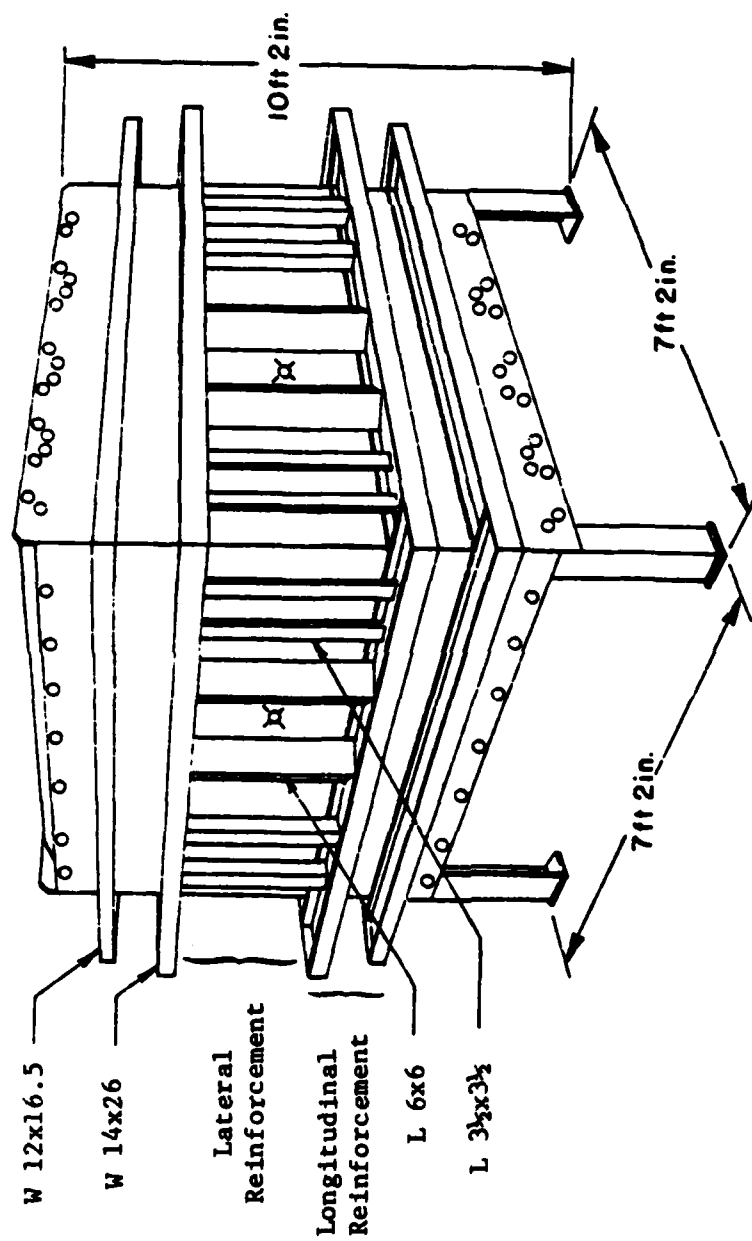


Fig. 1.2 - Isometric View of Triaxial Device Showing Side Reinforcement Details  
(From Kopperman et al, 1982)

Horizontal  
Excitation  
Port at the  
East Wall

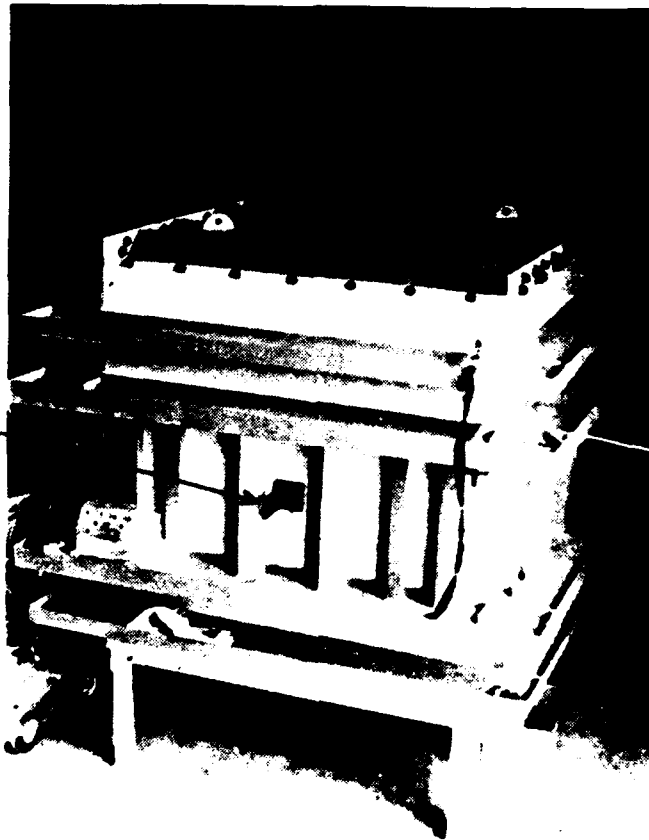


Fig. 1.3 - Completed Triaxial Device (From  
Kopperman et al, 1982)

sand mass to the desired stress state, 3. generate compression or shear waves in the sand mass, 4. monitor and digitally record these waveforms, and 5. monitor stress and strain throughout the sand sample during testing. A schematic drawing of the triaxial device and associated systems is shown in Fig. 1.4.

A new raining device was designed and constructed as part of the work reported herein (Section 2.3). This was done in an attempt to place the sand into the triaxial device in a more uniform state than possible by Knox and Kopperman. With the new rainer, the rate of sand flowing into the device during sample construction was carefully controlled. As a result, the density of the sand specimen increased by about six percent compared to the earlier tests (Section 3.3), and the specimen was very uniform with a maximum variation in density of less than 6.3 percent.

Each wall of the triaxial device is designed to represent a principal plane so that axes perpendicular to the walls of the device represent principal directions. To permit independent control of the pressure in each of the three principal directions, confining pressures are applied to the sand mass using three membranes (water pressure bags) placed on the inside of the triaxial device : one on the top and one on each of two adjacent sides, namely the north and west sides

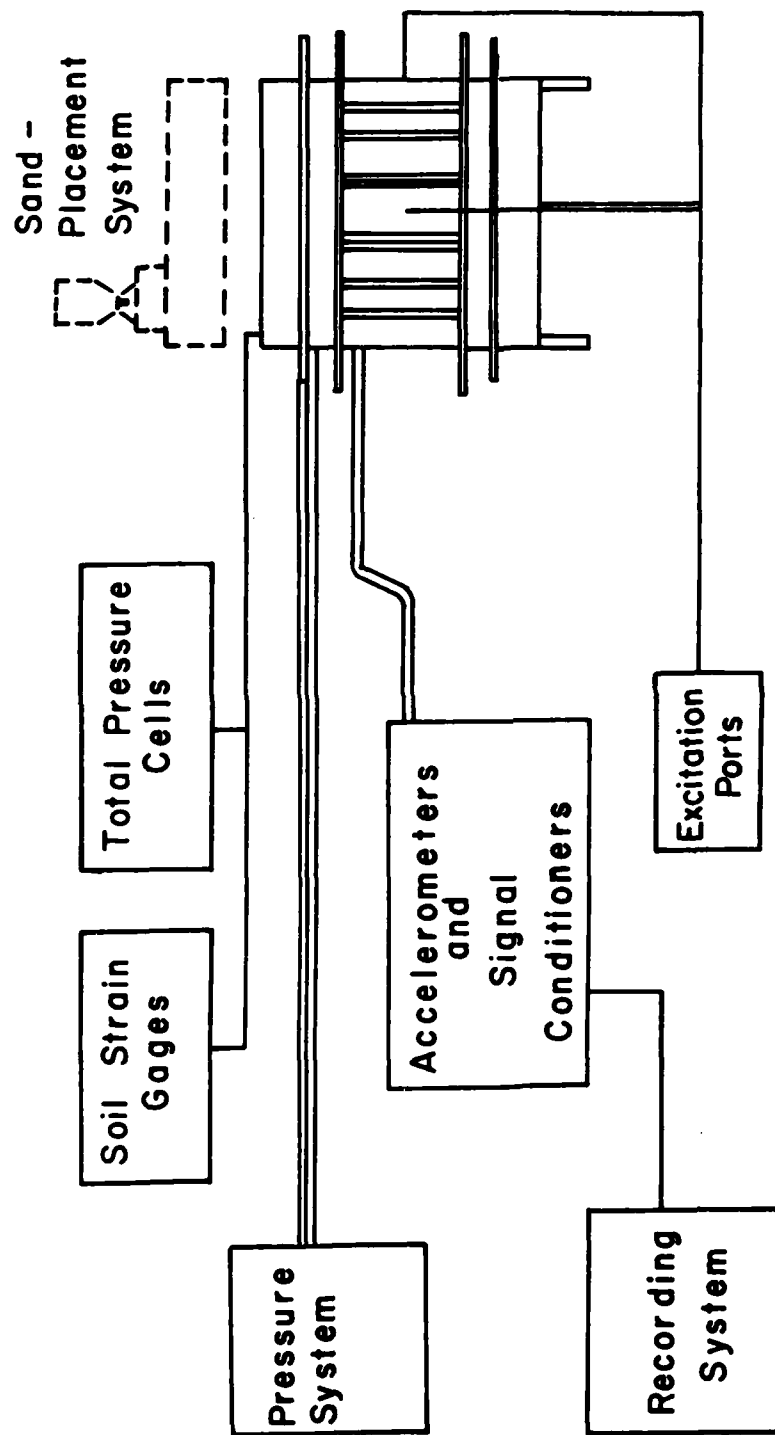


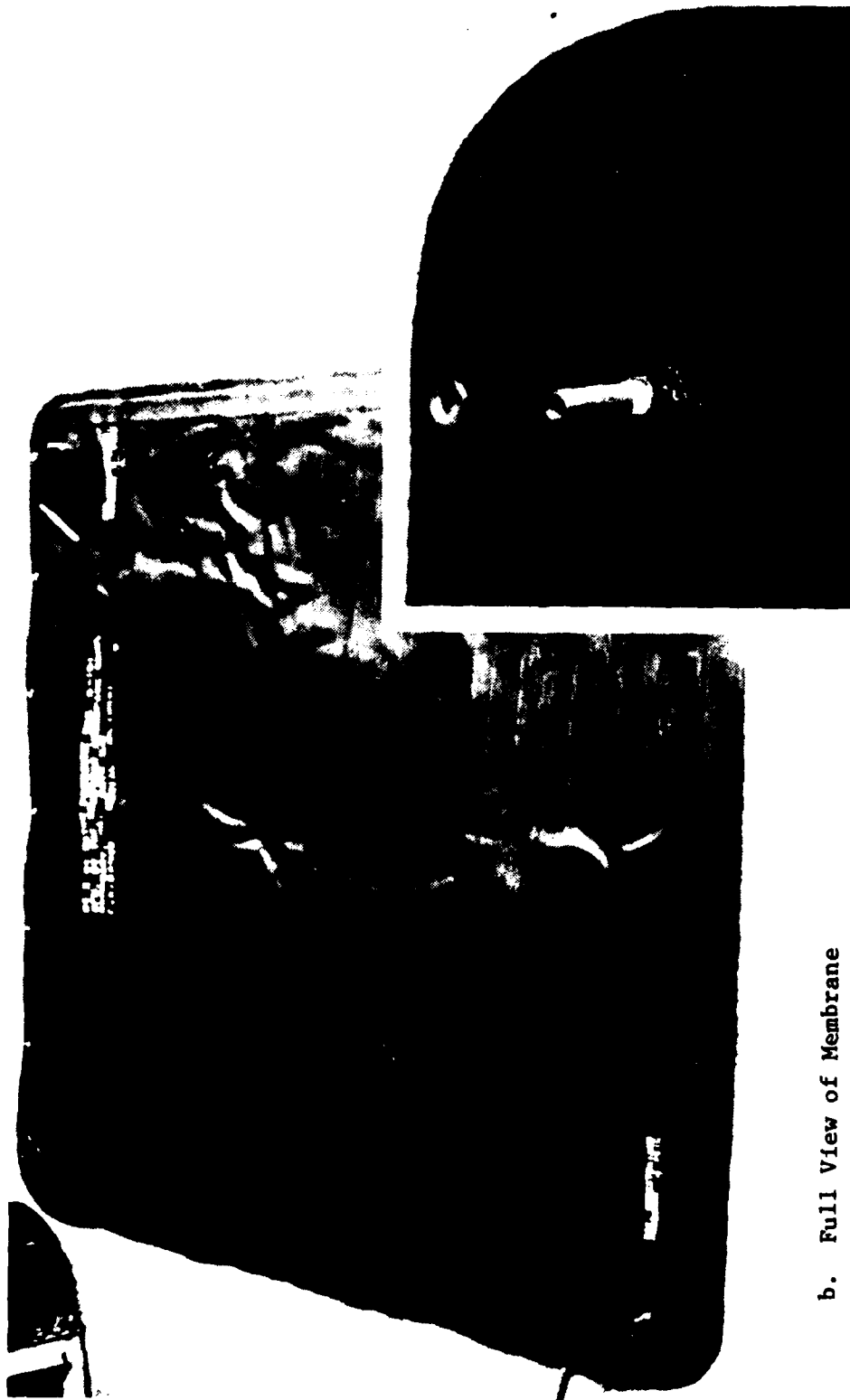
Fig. 1.4 - Schematic Diagram of Triaxial Device and Associated Systems  
(After Kopperman et al, 1982)



of the device. Each membrane has two ports located at opposite corners so that water can be allowed to fill up or drain from the membrane. One of these membrane is shown in Fig. 1.5. When the membranes full of water, air pressure from the building air supply is used to pressurize the membranes. The air pressure is monitored using air regulators together with a 12-in. (30.5 cm) diameter, Heise type CM pressure gauge (accurate to within  $\pm 0.1$  percent of full-scale reading). A schematic drawing of the pressurizing system is shown in Fig. 1.6, and a picture of the control panel is shown in Fig. 1.7.

Since the overall objective of this research is to study body waves (compression and shear waves) propagating through a soil mass, a mechanism for generating these waves at the soil boundaries is necessary. To achieve this goal, excitation ports were placed in the center of the three mutually perpendicular sides of the triaxial device which were not covered by membranes : the bottom, and the south and east sides. The excitation ports were modified and improved from those used by Kopperman et al (1982) as discussed in Section 2.4. (A detailed sketch of an excitation port is shown in Fig. 2.5.)

Compression and shear waves propagating through the sand mass are monitored and recorded with the electronics shown schemat-



b. Full View of Membrane

a. Close-up View of Port

Fig. 1.5 - Membrane Used to Apply Load to Sand Specimen in Triaxial Device  
(From Kopperman et al, 1982)

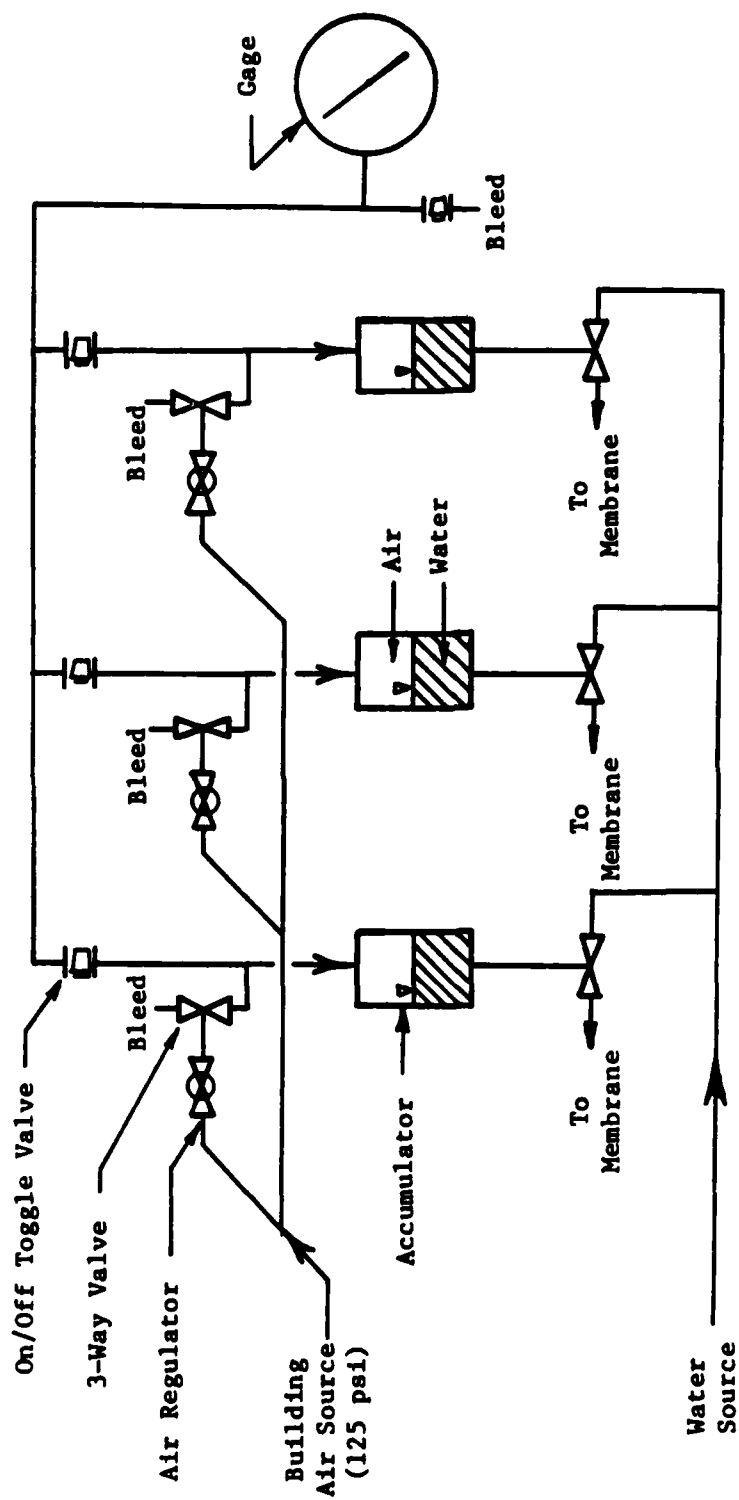


Fig. 1.6 - Schematic of Air/Water System  
Used to Pressurize Membranes  
(From Kopperman et al, 1982)

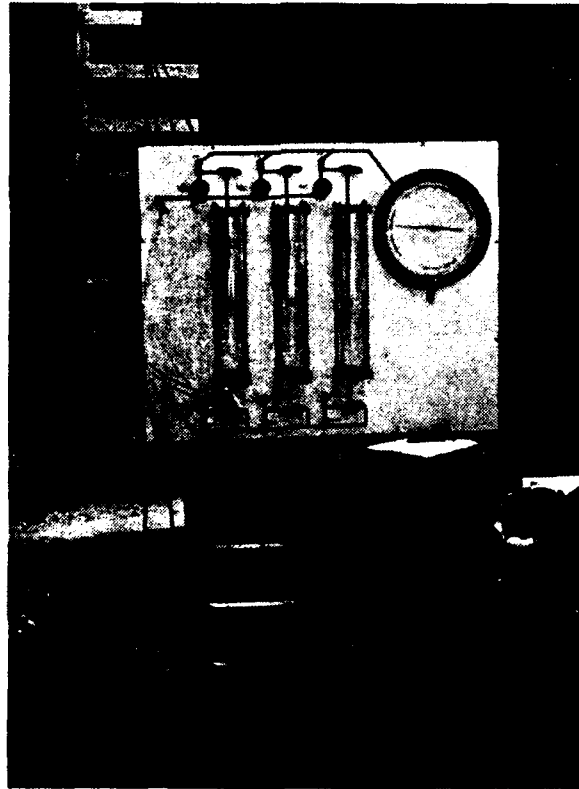


Fig. 1.7 - Panel Board Used  
to Pressurize Membranes in Triaxial Device  
(From Kopperman et al, 1982)

ically in Fig. 1.8. Improvements and recalibration of instruments in this monitoring and recording system are discussed in Section 2.5.

## 1.2 PRESENT TESTING

Once all modifications and calibrations were completed, tests with various states of confinement were performed. The procedures and results for isotropic, biaxial and triaxial confinement states are presented in Chapters 4, 6 and 7, respectively.

The effects of stress history and structural anisotropy on P-wave velocity were determined first before any conclusion about the effects of confinement on P-wave velocity could be reached. These effects are most easily seen in the results presented in Chapter 4 for isotropic confinement. The effect of stress history on P-wave velocity is small and can be neglected. Due to structural anisotropy, the sand sample under isotropic confinement can be treated as a cross-anisotropic material with P-wave velocities in the horizontal directions equal and about 17 percent higher than the velocity in the vertical direction. A mathematical treatment for the stress-strain relationship in cross-anisotropic model is presented in Chapter 5.

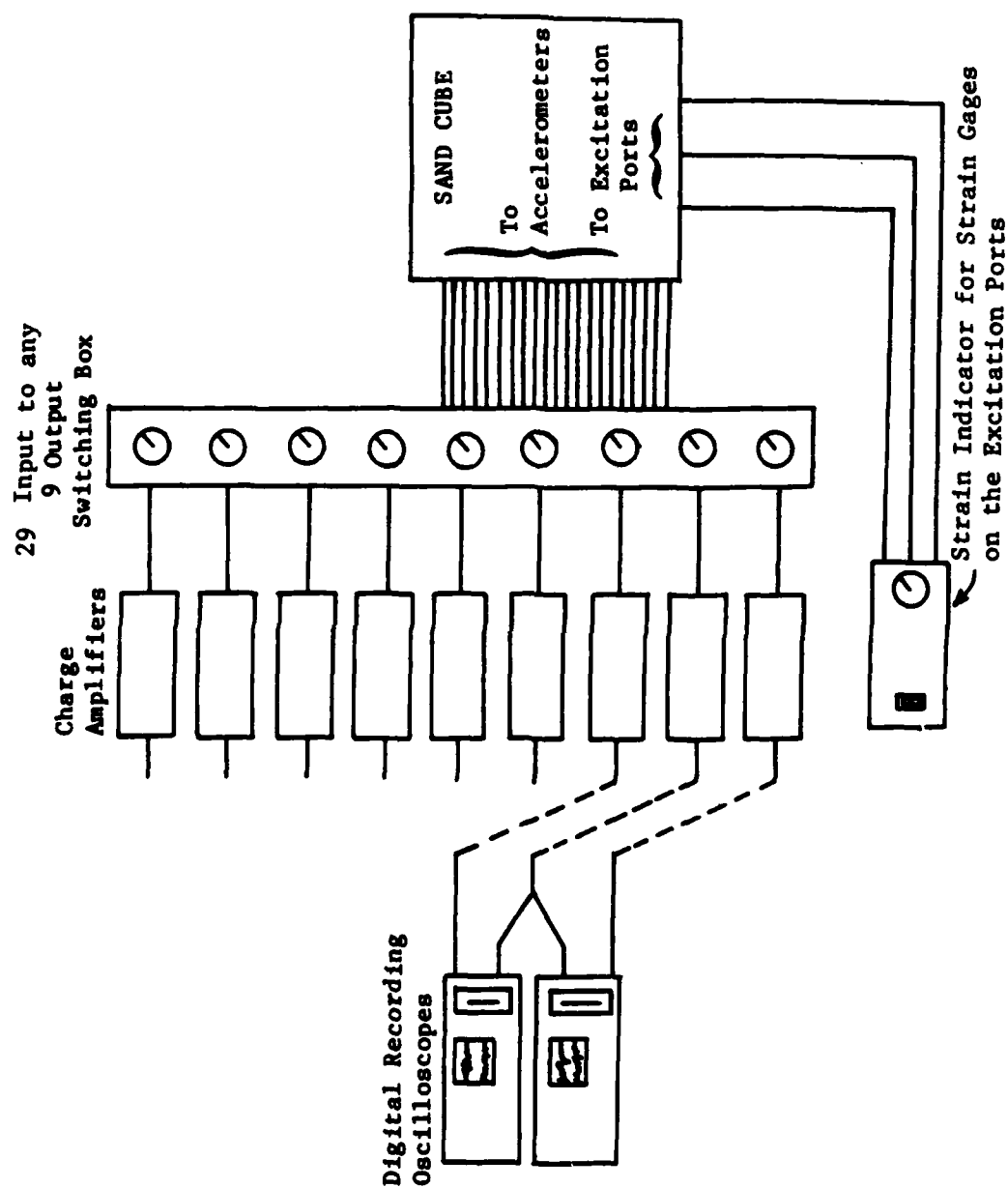


Fig. 1.8 - Schematic of Monitoring and Recording Systems

The results of P-wave velocity measured under isotropic, biaxial and triaxial confinement states lead to the same conclusion: that is, P-wave velocity is proportional to the effective principal stress in the direction of wave propagation raised to a positive power less than unity. The normal principal stresses perpendicular to the direction of wave propagation have a negligible effect on P-wave velocity. This confirms the earlier work by Kopperman et al (1982) in a more complete fashion.

## CHAPTER TWO

### IMPROVEMENTS OF TESTING FACILITIES

#### 2.1 INTRODUCTION

Considerable effort was expended on this project to improve the triaxial loading device and associated systems used by Kopperman et al (1982) and Knox et al (1982). This work was done so that duplicate tests could be performed under more carefully controlled conditions than possible in the earlier tests. In addition, larger variations in tests under anisotropic loading were performed than done earlier because of time limitations. Improvements were made in the following areas : 1. construction of a storage facility in which the sand could be kept dry, 2. development of a new raining device used to build specimens, 3. addition of the capability to control the load applied at each excitation port, 4. calibration of the accelerometers, stress cells and strain cells, and 5. inclusion of additional accelerometers to provide more complete data for an attenuation study and for an initial study of shear waves which are polarized obliquely (at some angles other than parallel to the principal stress axes).



## 2.2 STORAGE OF SAND

One of the time-consuming problems encountered in the earlier study was drying of moist sand (which was stored outdoors) before sample construction. Therefore, it was decided to construct some type of storage facility. A corrugated-steel bin measuring about six ft (1.83 m) in diameter and six ft (1.83 m) in height was available at no cost in Cockrell Hall. The bin was, therefore, moved to the Balcones Research Center and was located outside the Phil M. Ferguson Structural Laboratory, next to the west wall and close to the north truck entrance of the Laboratory. This is a convenient location since the triaxial device is located at the north-west corner inside the Laboratory.

To keep the sand in the bin dry, the bin was placed on top of a steel table as shown in Fig. 2.1. The top of the table was made of a 6.33-ft (1.93 m) square plate with a thickness of 0.25 in. (0.64 cm). Four legs and a framework for the table top were built of W18X10 I-beams. The legs were 2-ft (61.0 cm) high and were welded to the framework at the top and to 0.5-in. (1.27 cm) thick, 1-ft (30.5 cm) square steel plates at the bottom. The bottom plates were used to distribute load from each leg to a concrete footing which was also 1-ft (30.5 cm) square and about 1.5-ft (45.7 cm) deep.

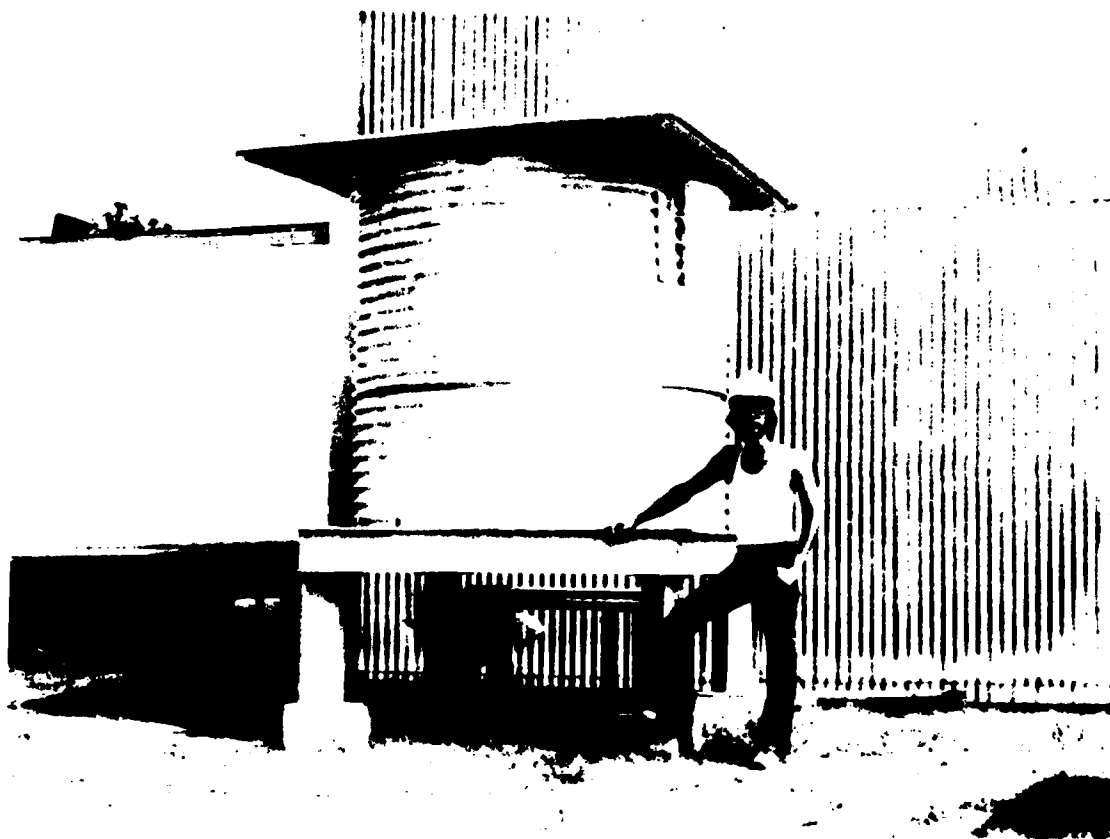


Fig. 2.1 Completed Storage Bin

The lower edge of the bin was fixed to the top of the steel table with small pieces of angle iron with bolt connections. An opening of about 8 in. (20.3 cm) by 11 in. (27.9 cm) was cut near the bottom edge of the bin. A trap door with hinges at the top was bolted to the bin to cover the opening. Styrofoam was glued under the perimeter of the door to prevent sand leakage and to provide a moisture seal. The trap door could be opened to any desired position with the control of a bolt connection. Once the trap door was opened, dry sand would flow out of the bin into a concrete bucket seated next to it. This greatly improved the sample construction process (Section 3.3).

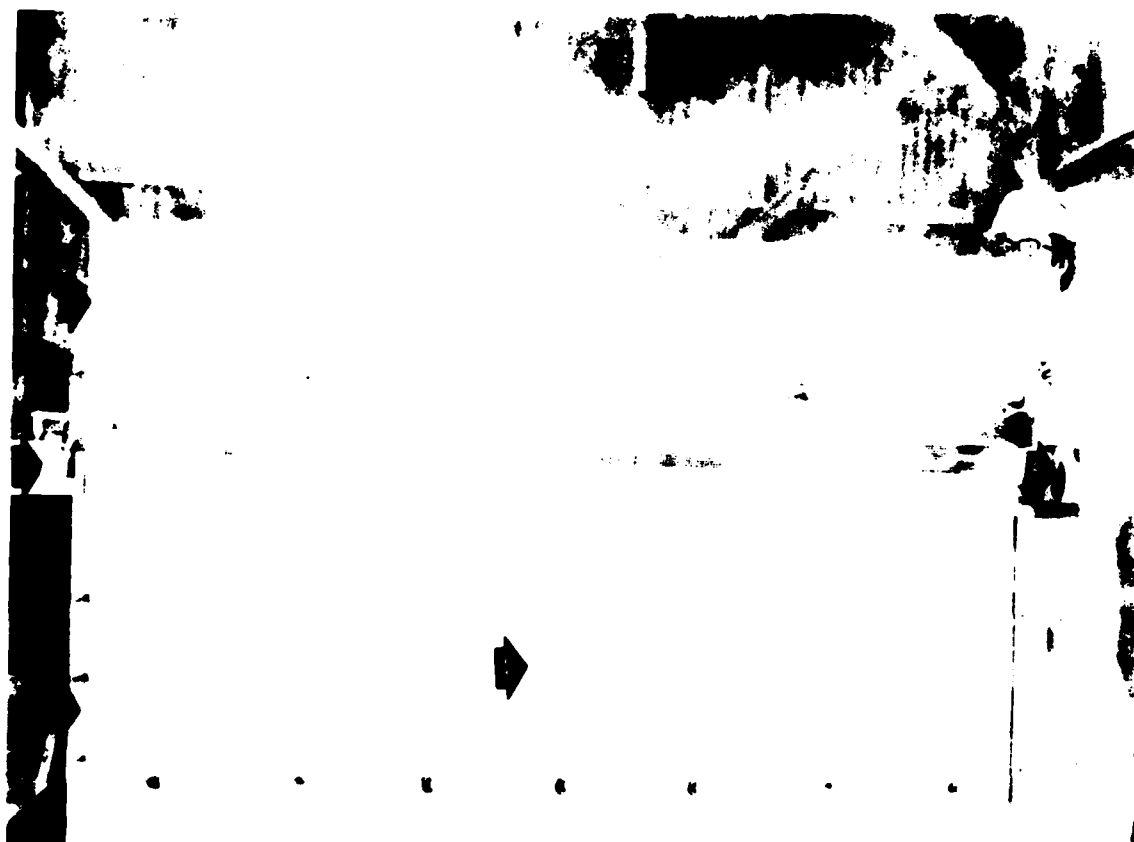
A 6.5-ft (1.9 m) square top was built for the bin with plywood covered by sheet metal. It was decided that this was the most economical way to provide a waterproof top for the bin. Two handles were bolted to the top so that it could be removed and replaced easily with the use of a fork-lift.

## 2.3 SOIL PLACEMENT

Since the old rainer constructed by Knox and Kopperman could not control the amount the hopper gate opened and hence could not control the flow rate of the sand (Kopperman et al, 1982), a new rainer

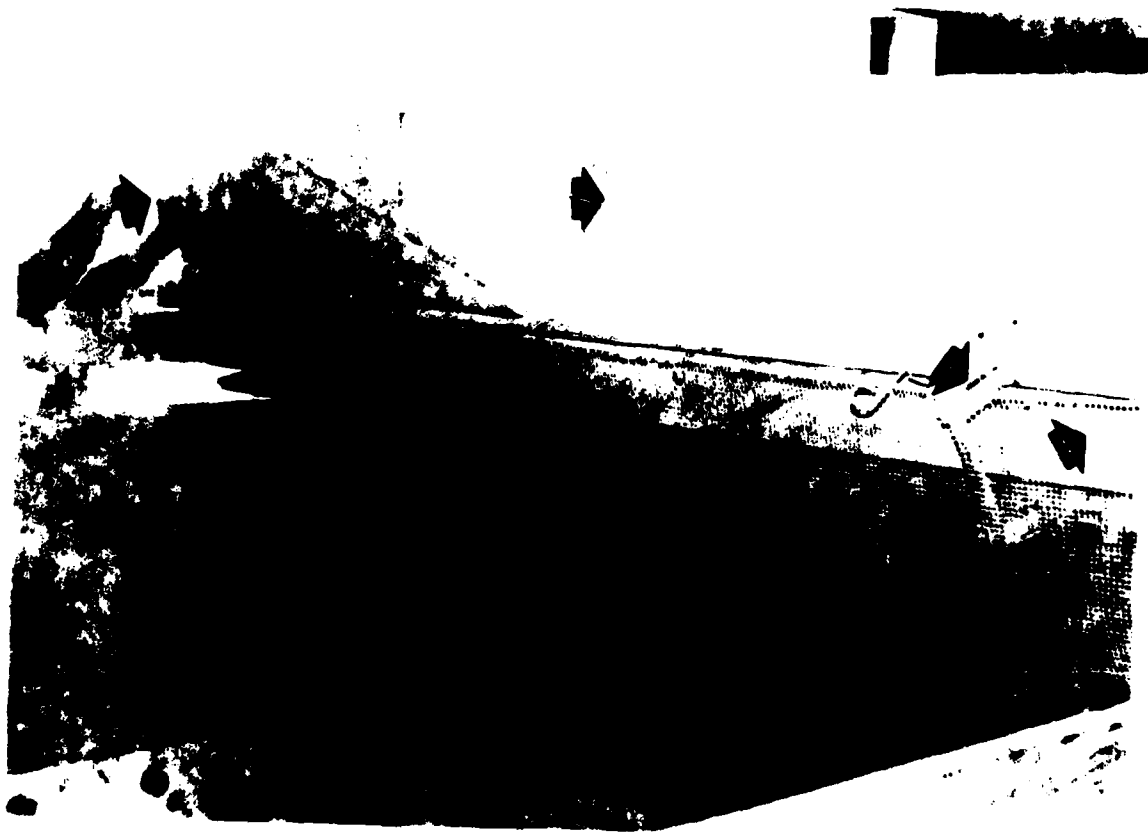
was designed and constructed. The rainer is simply an open rectangular box measuring 7.25-ft (2.21 m) long, 1.75-ft (53.3 cm) wide and 1.5-ft (45.7 cm) deep. The box is made of plywood and has a steel framework on the outside as shown in Figs. 2.2 and 2.3. The plywood bottom has four rows of 0.75-in. (1.91 cm) diameter holes drilled in it in the pattern shown in Fig. 2.4. Each end of the rainer has a 3.42-ft (104.1 cm) long angle (L3X3) welded to the lower edge of the steel framework. Heavy-duty castors are fixed to each end of the L3X3 angle. These extended portions with castors add to the stability of the rainer when it is being moved during the raining operation. Four trap doors were built under the plywood bottom, each covering two rows of holes as shown in Fig. 2.4. The amount the trap door is opened is controlled by a lever-arm system. The lever-arm system can be securely fixed with the trap doors closed or with the trap doors opened to the selected position to allow the desired flow rate of sand. A wire mesh with openings of 0.25 in. (6.4 mm) was placed below the rainer as shown in Fig. 2.3. The wire mesh acts as a dispersing screen since sand striking the mesh will bounce off randomly, hence constructing a more uniform specimen. The screen also keeps foreign materials like gravels and organics from becoming part of the sand sample.

The same wooden collar used by Knox and Kopperman was used to obtain the same range of drop height of the sand into the triaxial



- Legend:
1. Steel framework of the new rainer
  2. Rail along which rainer travels
  3. Angle irons (L2X2) along the corners of the wooden collar
  4. Wooden collar
  5. Castor of rainer

Fig. 2-2 View of New Rainer Loaded with Sand and in Place for Raining



- Legend:
1. New rainer
  2. Control Arm (see Fig. 2.4)
  3. Lever connection to trap doors
  4. Wire mesh used as dispersing screen

Fig. 2.3 Raining Sand into Triaxial Device Using New Rainer

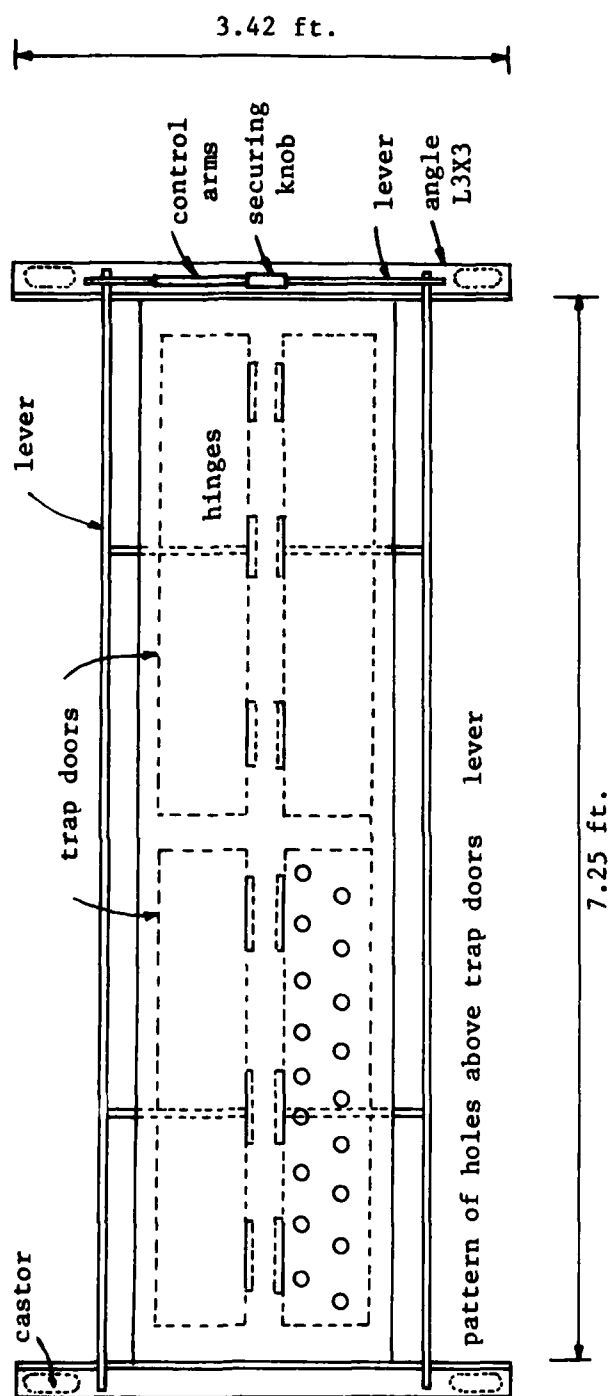


Fig. 2.4 Top View of New Rainer

device, namely 9.5 ft (2.9 m) at the start of the filling operation to 2.5 ft (76.2 cm) at the conclusion. Since the new rainer is much heavier than the old one, the collar was reinforced with angle irons (L2X2) along the four vertical edges. Angle irons at two corners are shown in Fig. 2.2. The angles were bolted to the collar and are 3-ft (91.4 cm) in length so that they support the rails (as shown in Fig. 2.2) at the top while resting on the top longitudinal reinforcement ring of the triaxial device. This greatly increased the rigidity and stability of the collar. Each rail also has three sections of 6-in. (15.2 cm) long angles (L2X2) bolted to the collar and distributed evenly under the rail to provide better support for the rail.

#### 2.4 EXCITATION PORTS

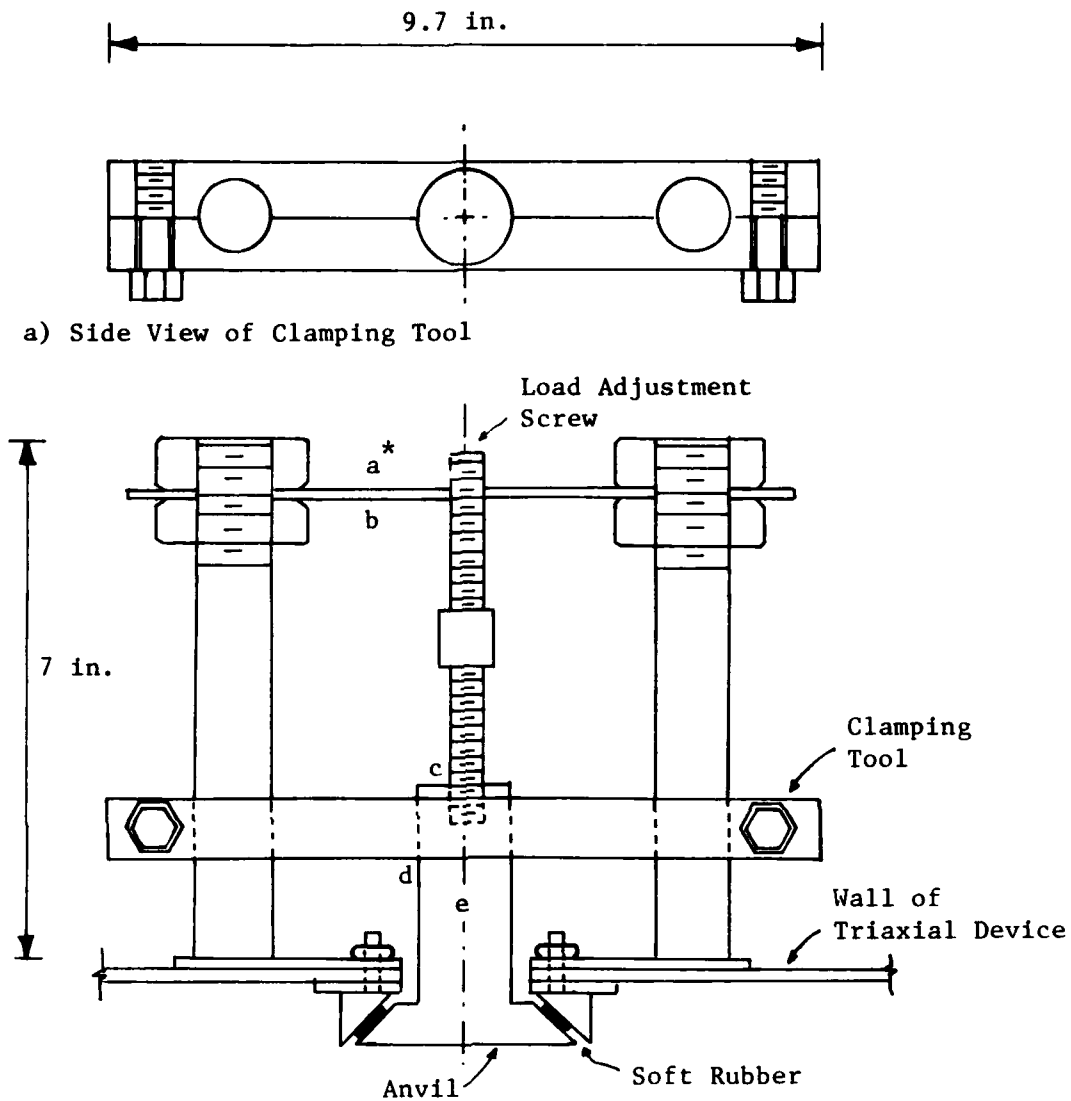
Sand leakage from the two horizontal excitation ports (see Fig. 1.3) was reported in the previous tests. This was most probably due to a slight rotation of the anvil and subsequent sliding of sand out of a gap formed between the anvil and hole in the wall for the excitation port. To prevent this, a clamping tool was designed to hold the anvil in place when testing was not being performed. The clamping tool is basically two similar pieces of steel bars placed together. Three holes have been drilled in the bars so that the shaft of the anvil fits in the center hole and the two large bolts of the external frame fit in



each of the side holes. The clamping tool is shown in place on an excitation port in Fig. 2.5. The ends of the two steel bars can be bolted tightly together, hence the anvil is held fixed with respect to the external frame, which in turn is fixed to the triaxial device. The anvil in each excitation port was clamped with these tools except during testing.

It was decided that the anvil of the shaft would provide enough striking surface to generate the desired waves, therefore the 3-in. (7.6 cm) square plate used previously as the striking surface was removed. Shear waves were generated in the soil by striking the anvil shaft either horizontally or vertically (parallel to the side of the triaxial device) about 1 in. (2.5 cm) from the wall. Compression waves were generated by striking the top surface of the anvil in the direction of the axis of anvil (perpendicular to the side of the triaxial device). The striking locations are shown in Fig. 2.5b.

The anvil in each excitation port which is in contact with the soil must maintain the same pressure against the soil as is being applied by the membrane on the opposite face of the triaxial device. To monitor the load applied by the anvil, strain gages were mounted to the thin plate of the external frame of the port as shown in Fig. 2.5b. After a preliminary calculation on the range of bending strain of the



Note:

1. \*a and b are locations where strain gages are mounted on the surface of the thin plate
2. c is location of striking for compression waves
3. d and e are locations of striking for shear waves

b) Excitation Port with Clamping Tool in Place

Fig. 2.5 - Clamping Tool and Excitation Port

thin plate under the working stress range of 10 to 40 psi (68.9 to 275.6 kPa), strain gages of type EA-06-500BL-350 were selected. This is a foil-type, bonded, resistive gage with 350 ohms  $\pm 0.15$  percent as the gage resistance and  $2.07 \pm 0.5$  percent as the gage factor. The strain gages and installation aids were purchased from the Micro-Measurements Division of the Measurements Group at Raleigh, North Carolina.

The strain gages were mounted on the thin plate following the procedures recommended by the manufacturer. The relation between strain and resistance change for these gages is :

$$\epsilon = (1/F) \cdot (\Delta R/R)$$

where:  $\epsilon$  = strain in microstrains ( $10^{-6}$  cm/cm),

F = gage factor,

$\Delta R$  = change in resistance in ohms, and

R = gage resistance in ohms.

A strain indicator was used to read off the resulting strain digitally in microstrains. Two strain gages were mounted to each plate (one on top and one beneath) in such a pattern that temperature compensation was provided and the output was doubled. After the gages were connected to the lead wires, silicone glue was placed over the gages to protect them from the ambient environment of moisture, dust and dirt. A completed excitation port is shown in Fig. 2.6.

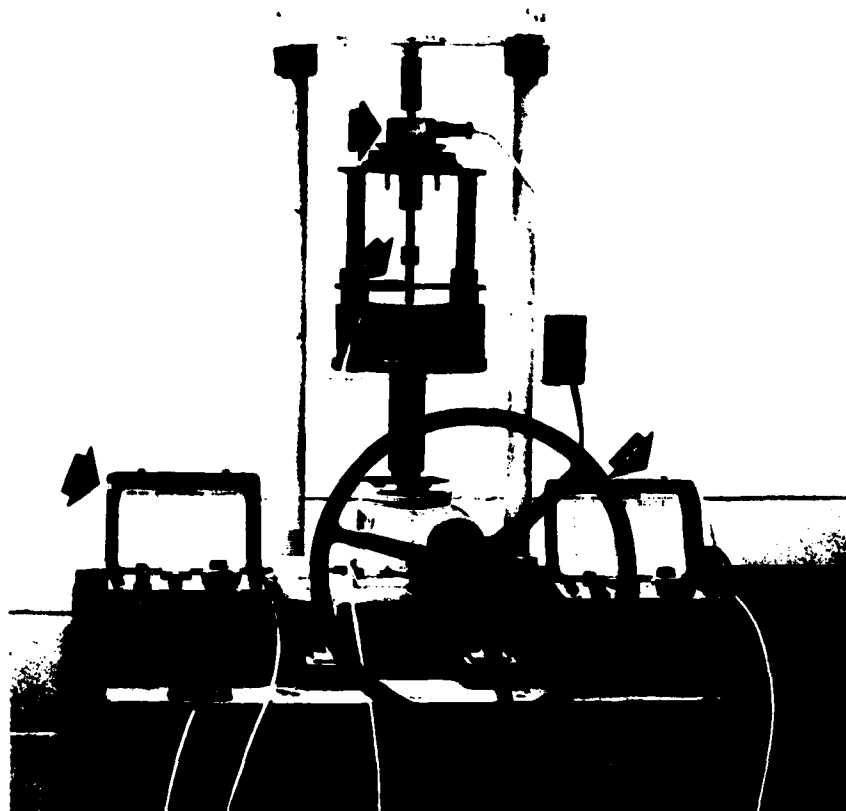


Legend: 1. Strain gage  
2. Clamping tool  
3. Load adjustment screw

Fig. 2.6 Completed Excitation Port In Place

The strain gages used as secondary transducers were calibrated in terms of pressure on the face of the anvil in contact with the sand. Therefore, the strain gages were calibrated using a load cell to monitor the applied force. The area of the anvil in contact with the sand is 9 sq-in. ( $522.6 \text{ cm}^2$ ), hence a 1-lb force (4.45 N) induces a pressure of 0.111 psi (0.766 kPa) under the face of the anvil. The calibration set-up is shown in Fig. 2.7. A loading frame was used to push the anvil downwards (analogous to the soil pushing the anvil outwards) and a load cell was seated between the anvil and the loading piston of the press to monitor the applied pressure. Unfortunately at the time of calibration, only a 300-lb (1.34 kN) load cell was available. Therefore, the maximum reading corresponded to a pressure of 33.3 psi (229 kPa), which is slightly less than the maximum pressure of 40 psi (275.6 kPa) used in these tests. Two strain indicators were used: one to monitor the load cell and the other the strain gages. The final calibration curves are shown in Figs. 2.8 to Fig. 2.10. The reading for 40 psi (275.6 kPa) was obtained by linear extrapolation since the material is essentially linearly elastic.

The calibration curves in Figs. 2.8 to 2.10 showed small hysteresis upon load cycling. To see if creep had an insignificant effect on the strain gages, the top-bottom (TB) excitation port was kept under



- Legend:
1. 300-lb load cell
  2. Strain gages
  3. Strain Indicator for strain gages
  4. Strain Indicator for load cell

Fig. 2.7 Set-Up for Calibrating Strain Gages on Each Excitation Port

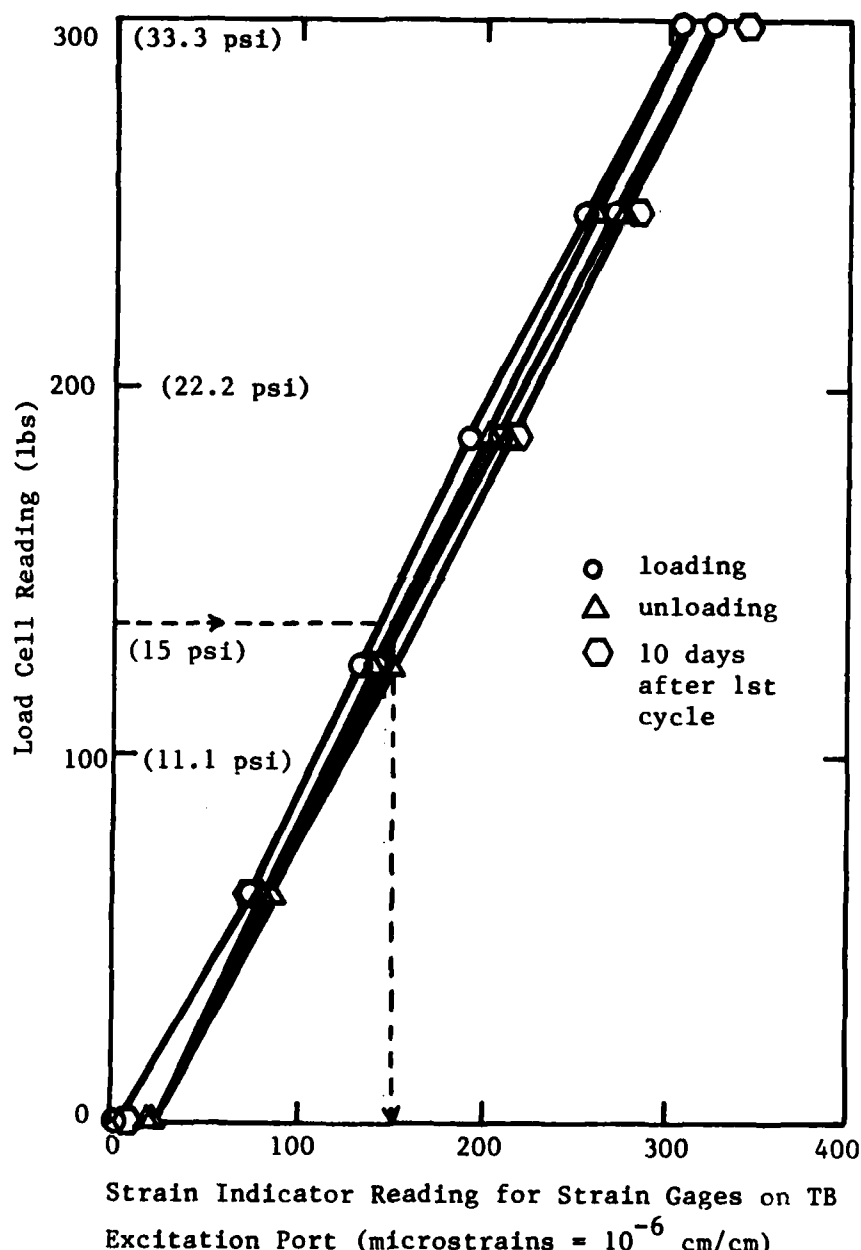


Fig. 2.8 Calibration Curve for Strain Gages on TB Excitation Port

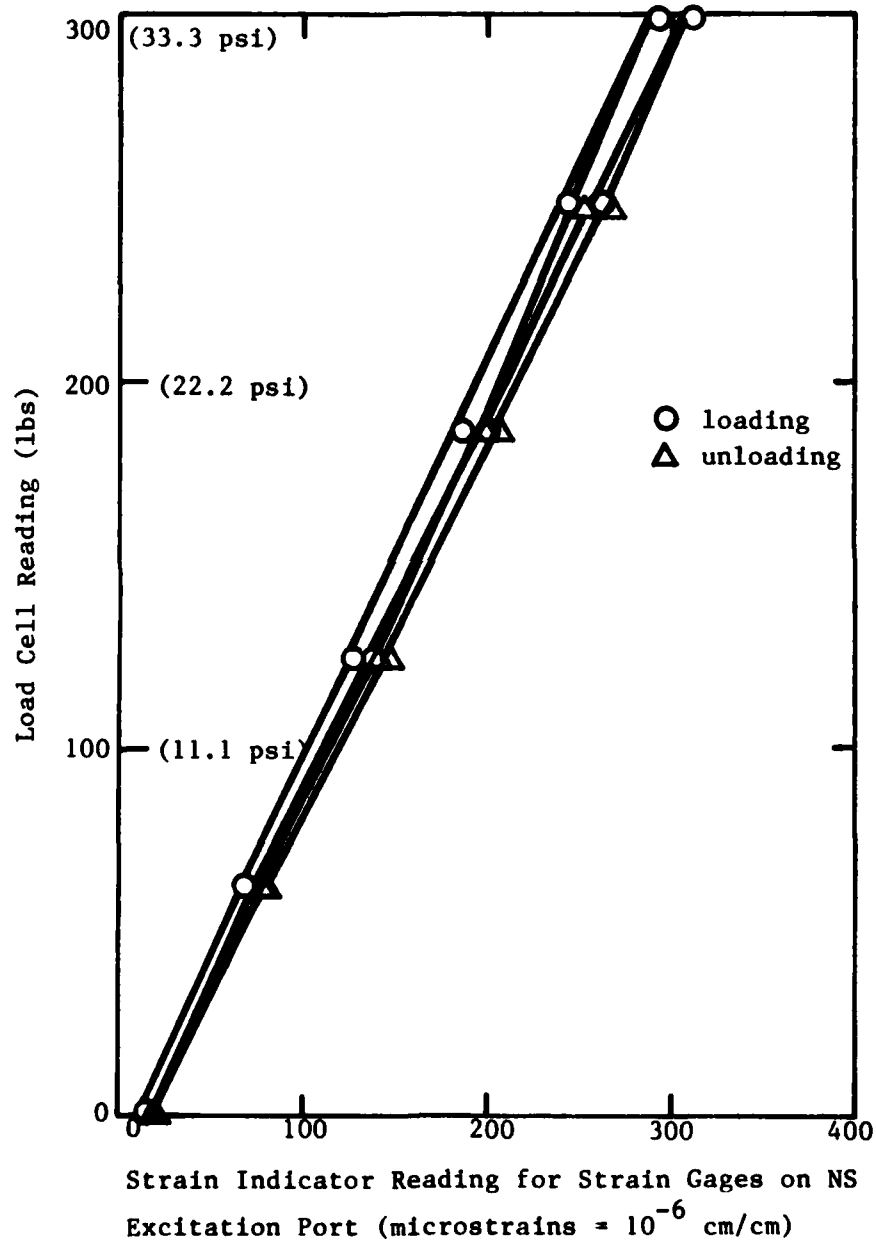


Fig. 2.9 Calibration Curve for Strain Gages on NS Excitation Port



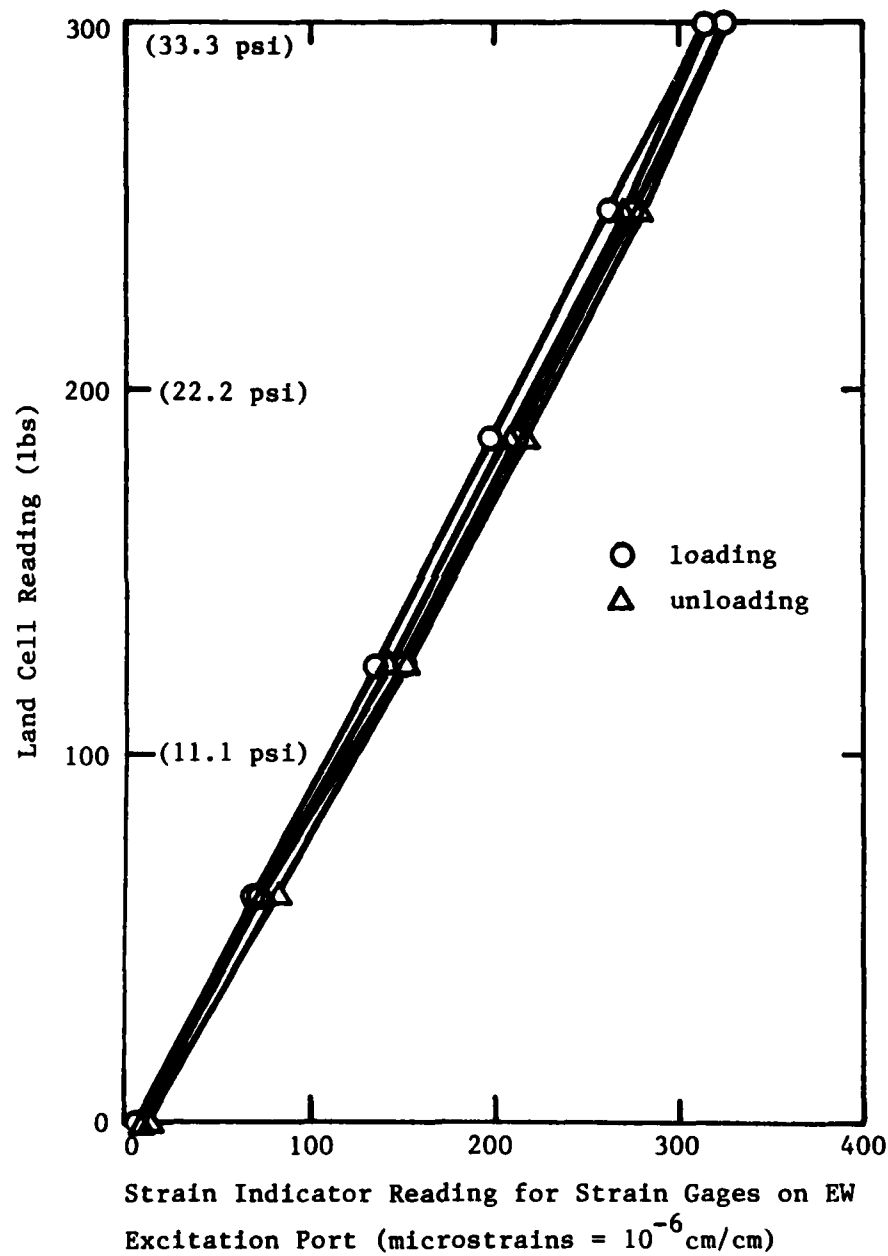


Fig. 2.10 Calibration Curve for Strain Gages on EW Excitation Port

a pressure of 13.8 psi (95.1 kPa) for a period of ten days. Then the strain gages were calibrated again. The data essentially fell within the hysteresis loops as shown in Fig. 2.8, and therefore creep was assumed to be negligible.

As an example of the use of the calibration curves, assume an isotropic pressure of 15 psi (103.4 kPa) was applied to the sand specimen. The corresponding average strain reading on the TB port should then be 152 microstrains as shown in Fig. 2.8. In order for the anvil contacting the sand to attain this pressure, the adjustment screw (Fig. 2.5) in the excitation port would be either tightened or loosened until the strain reading of the strain gages was 152 microstrains.

## 2.5 MONITORING AND RECORDING SYSTEM

The same instruments (accelerometers, charge amplifiers, oscilloscopes, stress cells and strain cells) used in the earlier tests were used in the monitoring and recording system, except that a significant effort was made to recalibrate the instruments before this series of dynamic tests was performed. In addition, eight more accelerometers were placed inside the triaxial device making a total of 29 accelerometers. All accelerometers were placed along the principal axes of the sand mass. Four of the eight new accelerometers were added along the

vertical direction to monitor vertically propagating shear waves which were polarized obliquely, and the other four accelerometers were added along the north-south direction to provide more data for the attenuation study.

#### 2.5.1 Digital Oscilloscopes

Two digital oscilloscopes with magnetic storage capabilities, series 2090, were purchased earlier from the Nicolet Instrument Corporation at Madison, Wisconsin. These units were used to monitor and record the outputs from the accelerometers. One of the two oscilloscopes (Serial No. 79703) was sent back to the dealer for maintenance, cleaning and adjustment of the magnetic storage unit before use.

#### 2.5.2 Accelerometers

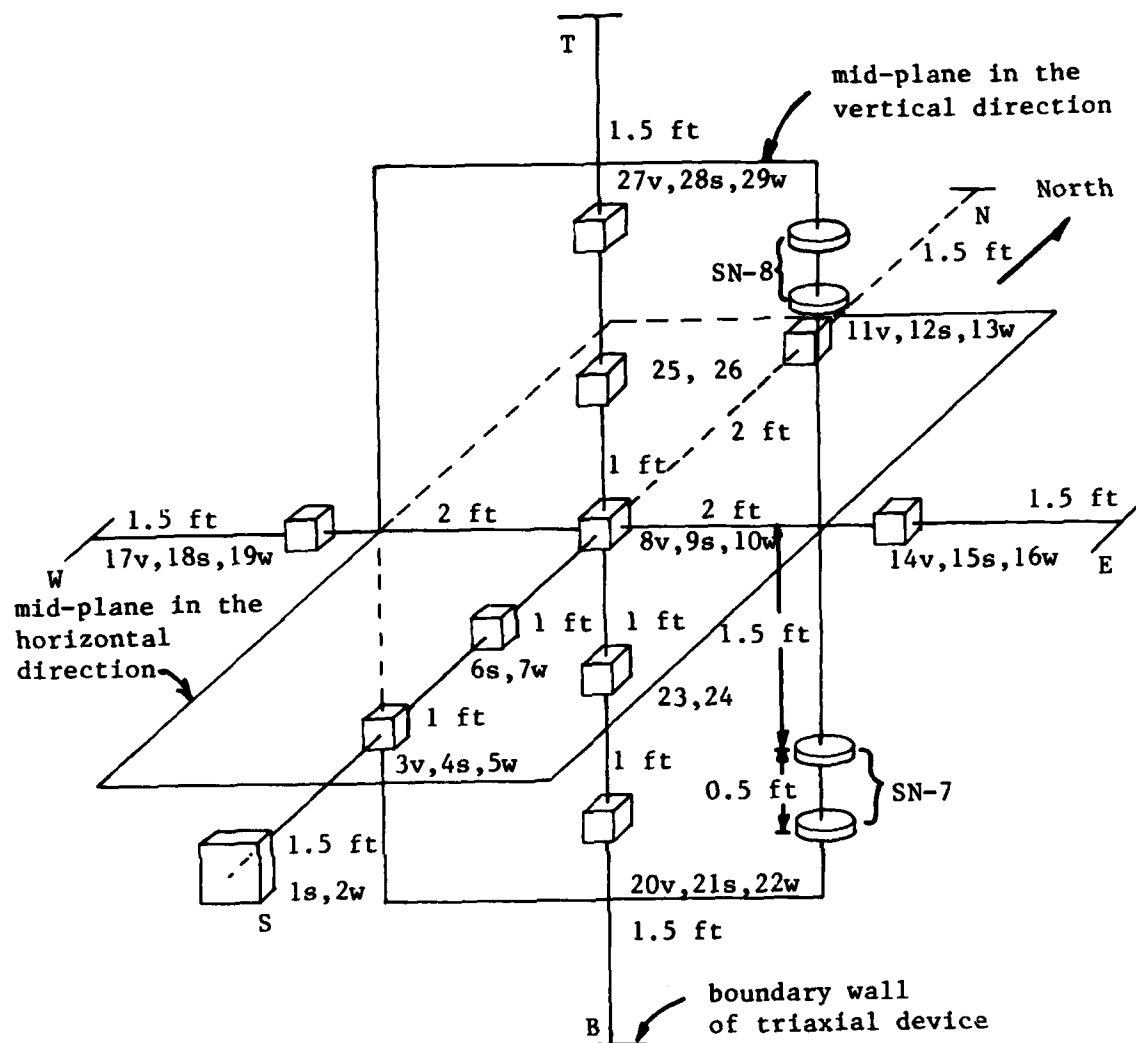
Twenty-one Endevco Isoshear accelerometers, model 7701-100, were used in the previous tests. These accelerometers have a typical charge sensitivity of 100 pc/g ( $10^{-12}$  coulombs per gravitational acceleration). Two more accelerometers of this model and six accelerometers of model 7701-50 were added in the present tests. All model 7701-50 accelerometers have half the charge sensitivity of a model 7701-100, namely 50 pc/g. This variation in charge sensitivity did not affect

collection of data since the same full-scale output could be obtained simply by changing the sensitivity dial and full-scale range switch on the charge amplifier, which is used to amplify the signal before it is displayed on the oscilloscopes. The six, 7701-50, accelerometers were used in the locations of the first and last 3-D accelerometer packages in the east-west direction as shown in Fig. 2.11.

Since the accelerometers are precise instruments which are designed to give many years of service without maintenance, only a comparative technique was used to calibrate the accelerometers. Any one accelerometer was believed to be reliable and could be picked as a "standard" against which the other accelerometers could be compared. As such, the calibration procedure consisted of imposing "identical" motions on the subject and standard accelerometers and the two outputs were compared. It was found that all accelerometers were functioning satisfactory with differences between outputs from the subject and standard accelerometers less than  $\pm 0.05$  percent.

#### 2.5.3 Accelerometer Blocks

Four new accelerometer blocks were added in the triaxial device. Each new accelerometer block was designed to house two accelerometers as compared to the 3-D accelerometer blocks constructed ear-



- Legend:
1. NS = north-south principal axis  
EW = east-west principal axis  
TB = vertical (top-bottom) principal axis
  2. Letter following accelerometer number indicates direction of sensitivity for that particular accelerometer (v=vertical, s=south and w=west)
  3. Accelerometers 23, 25 are  $45^\circ$  to N-S axis  
Accelerometers 24, 26 are  $22.5^\circ$  to N-S axis
  4. SN-7, SN-8 are two pairs of 4" strain sensors for vertical strain measurement

Fig. 2.11 - Schematic View of Instrumentation Locations

lier which housed three accelerometers. A schematic drawing of the location of the accelerometer blocks inside the triaxial device is shown in Fig. 2.11. Two new accelerometer blocks were located in the north-south (NS) principal direction so that more data could be collected in that direction for an attenuation study in another phase of the project being conducted by Dr. Carroll at West Point. The two other new accelerometer blocks were located in the vertical principal axis to monitor vertically propagating shear waves which were polarized obliquely.

One of the new accelerometer blocks was machined from aluminum while the other three were made of Birch wood, (the same material as that of the 3-D blocks). A picture of the aluminum block is shown in Fig. 2.12. The aluminum block was attached to the excitation port on the south wall of the triaxial device. The area of the square face of the block is same as the base of anvil to which the block is rigidly bolted. One accelerometer inside the block is oriented in the north-south direction and the other east-west (accelerometers 1s and 2w, respectively, in Fig. 2.11). These accelerometers were used to provide more data for the attenuation study being conducted by Dr. Carroll. Two more accelerometers oriented in the same relative directions (accelerometers 6s and 7w in Fig. 2.11) and rigidly attached to a new wooden block were located 2.5-ft (1.07 m) away from the aluminum block



Fig. 2.12 Accelerometer Being Assembled in Aluminum Accelerometer Block Which is Part of NS Excitation Port

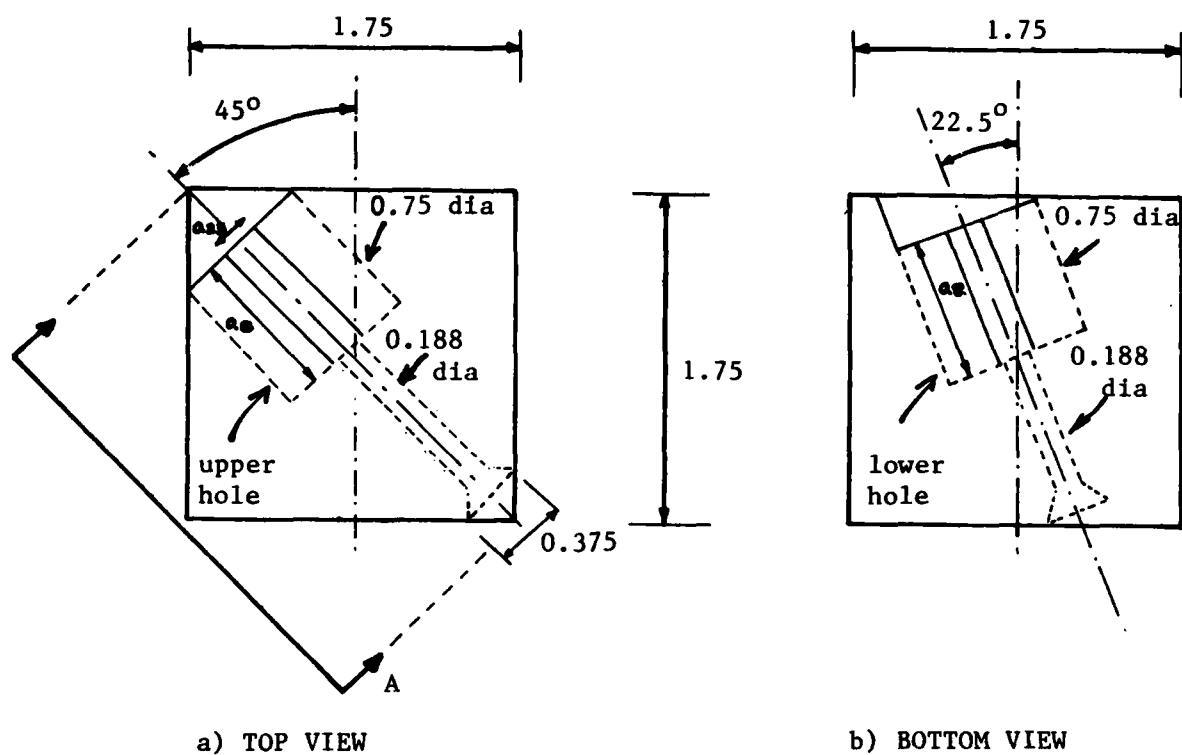
along the north-south principal direction. These accelerometers were also included for use in the attenuation study. These new wooden blocks are of the same size as the 3-D blocks.

The other new wooden blocks were added in the vertical direction: one was located 1-ft (30.5 cm) above the central accelerometer block and the other 1-ft (30.5 cm) below as shown in Fig. 2.11. Each new wooden block has holes for housing the accelerometers machined at different orientations, namely 45 and 22.5 degrees with respect to the east-west (EW) principal direction. As shown in Fig. 2.11, the accelerometers are numbered as 23 and 25 for the 45-degree inclination and 24 and 26 for the 22.5-degree inclination. A drawing for the design of the blocks, which are of the same size as the 3-D blocks, is shown in Fig. 2.13. With these two accelerometer blocks, shear waves polarized at 45 and 22.5 degrees to the east-west axis and propagating along the vertical principal axis could be monitored. However, the study of shear waves is not covered in this report.

#### 2.5.4 Charge Amplifiers

Since only nine Endevco charge amplifiers, model 2735, were purchased earlier, the 29 accelerometers were switched among them before the signals were displayed on the two digital oscilloscopes.





Note: All dimensions are in inches

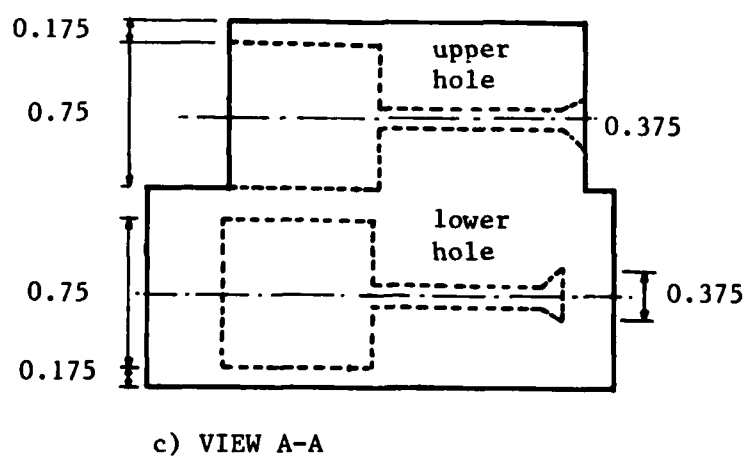


Fig. 2.13 - Accelerometer Block Used to Monitor Oblique Shear Waves

Therefore, these nine charge amplifiers were calibrated to make sure that they provided the same system gain. The charge amplifiers were calibrated for the full-scale sensitivity test following the procedure described in the instruction manual. A schematic drawing for the electrical set-up is shown Fig. 2.14. The full-scale test was conducted for a combination of sensitivity dial readings and full-scale ranges; the sensitivity dial readings were 1, 3 or 10 pc/g while the full scale-range switch was set at 1, 3, 10, 30, 100, 300, 1000 or 3000. At all times, the product of the setting of the sensitivity dial and the full-scale range switch was equal to the number of picocoulombs (pc) which will produce full-scale output. The results were satisfactory with minor adjustment of potentiometer occasionally necessary. The system gain had an accuracy of better than  $\pm 1.5$  percent on all full-scale ranges which means that the output from any two accelerometers should be within 1.5 percent for the same input.

#### 2.5.5 Stress Cells

Three total stress cells, model TE-9010, and a control unit, model C-9001, were purchased earlier from the Terra Technology at Redmond, Washington. (See section 3.6 of Kopperman et al, 1982 for a description of the stress cells.) Each stress cell was calibrated before it was placed in the sand. The set-up for calibrating the

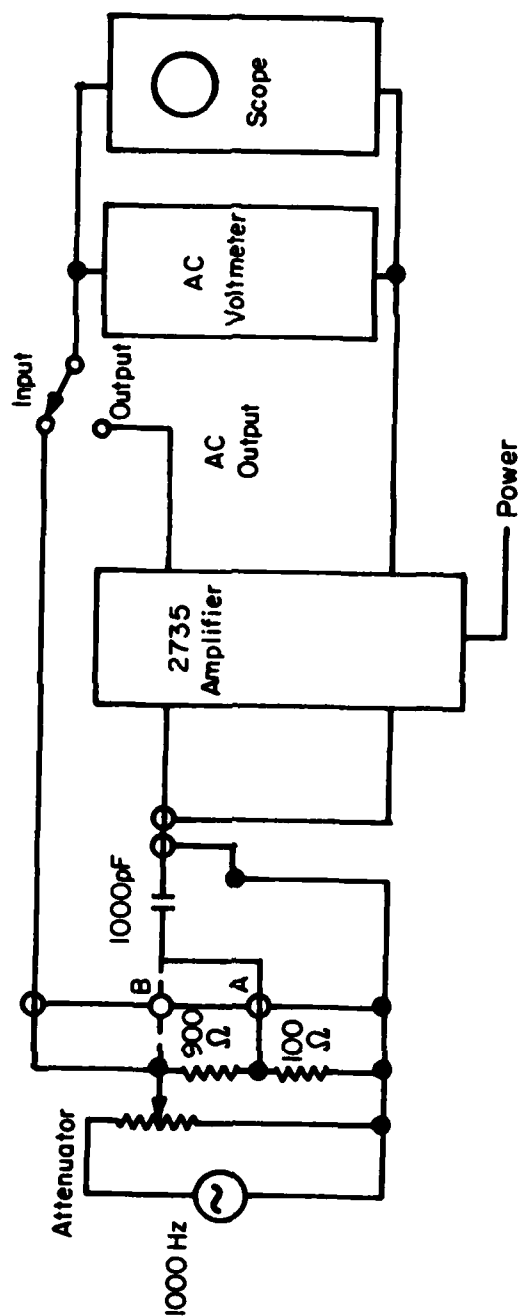


Fig. 2.14 Electric Set-Up for Calibrating Endevco Model 2735 Charge Amplifiers

stress cells was basically the same as that used for calibrating the strain gages on the excitation ports (Section 2.4). However, this time a larger capacity load cell (1000-lb (4450 N)) was used to monitor the applied load. In an attempt to have a uniform pressure over the faces of the gages, each stress cell was covered with rubber on both faces before it was placed between the top and bottom 6-in. (15.2 cm) square platens. The platens had the same size as the plane dimensions of the stress cell. The loading frame was then used to load the stress cell to known pressures and readings from the control unit of the stress cells were recorded. Calibration curves obtained are shown in Figs. 2.15 to 2.17. The curves are essentially straight lines above a pressure of 5 psi (34 kPa) with values of correlation coefficient varying from 0.99 to 1.00. There is no hysteresis effect upon load cycling.

#### 2.5.6 Strain Sensors

The strain sensors were calibrated using the calibration fixture and control unit purchased from the manufacturer. The strain sensors are the same as those used before, namely model 4000 series, Bison soil strain gages (Section 3.7, Kopperman et al, 1982). There are four pairs of 2-in. (5.1 cm) diameter strain sensors and four pairs of 4-in. (10.2 cm) diameter strain sensors. Dial calibration curves were generated following procedures recommended in the manufacturer's manu-

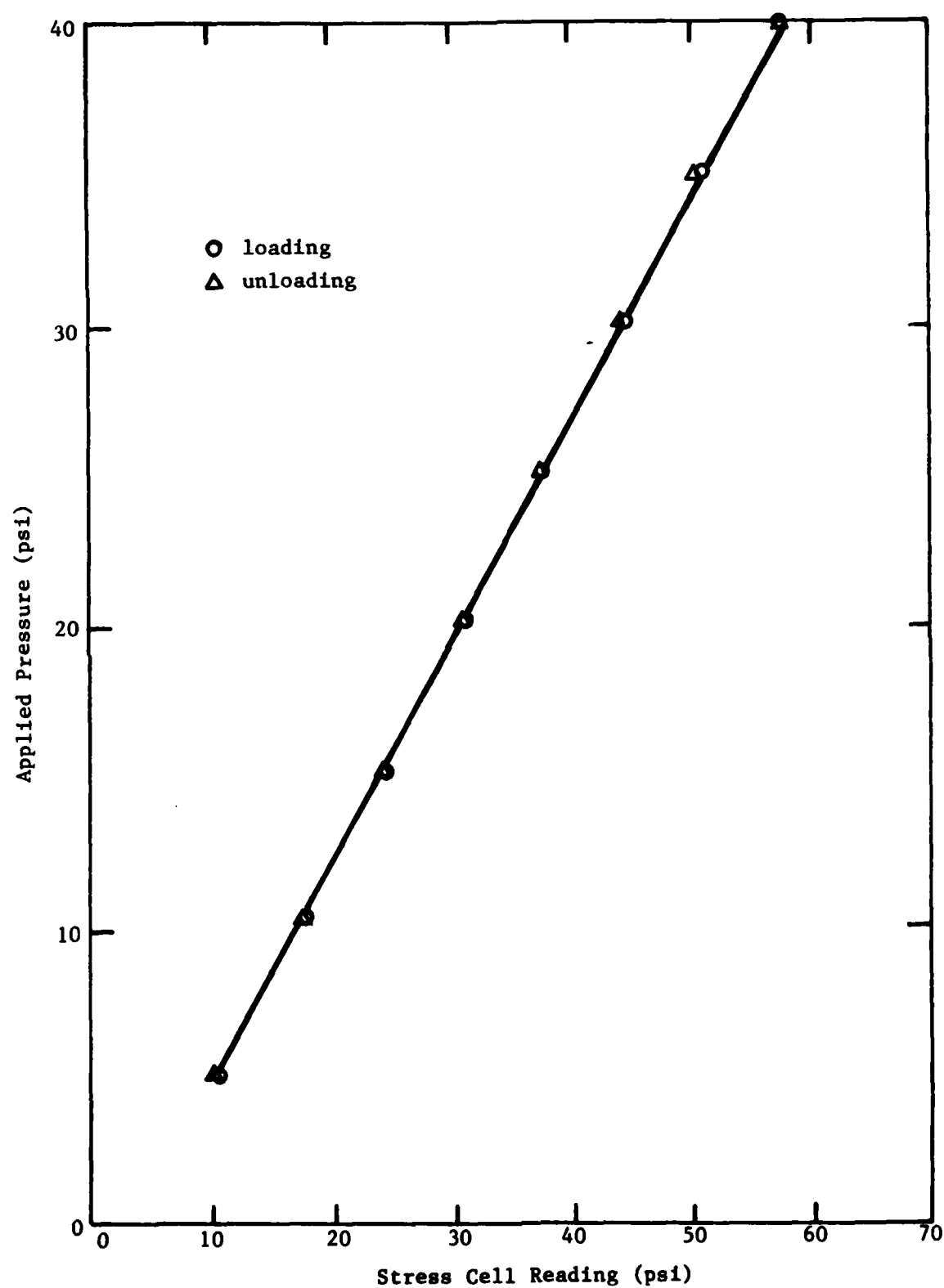


Fig. 2.15 Calibration Curve for Stress Cell SS-1

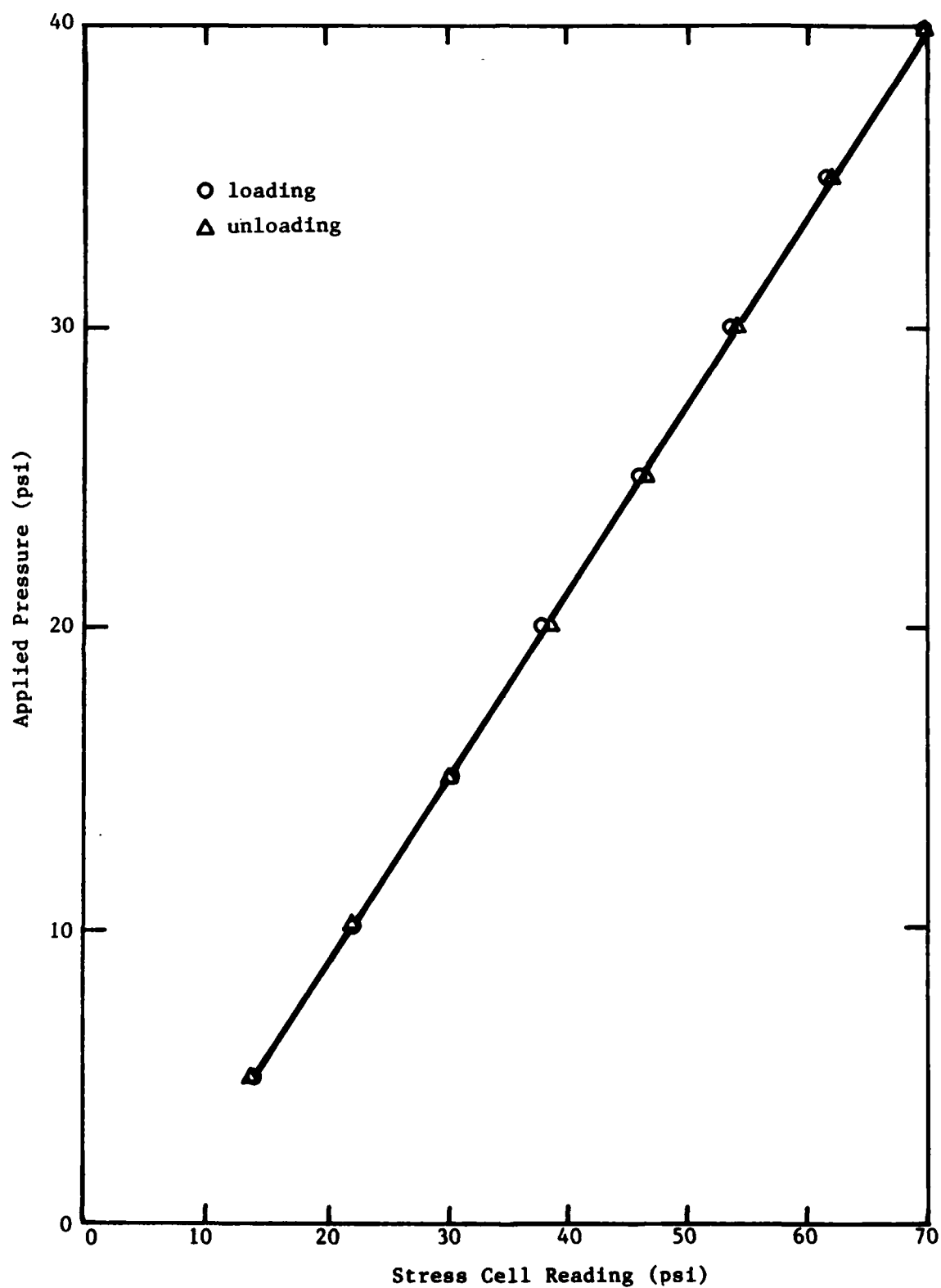


Fig. 2.16 Calibration Curve for Stress Cell SS-2

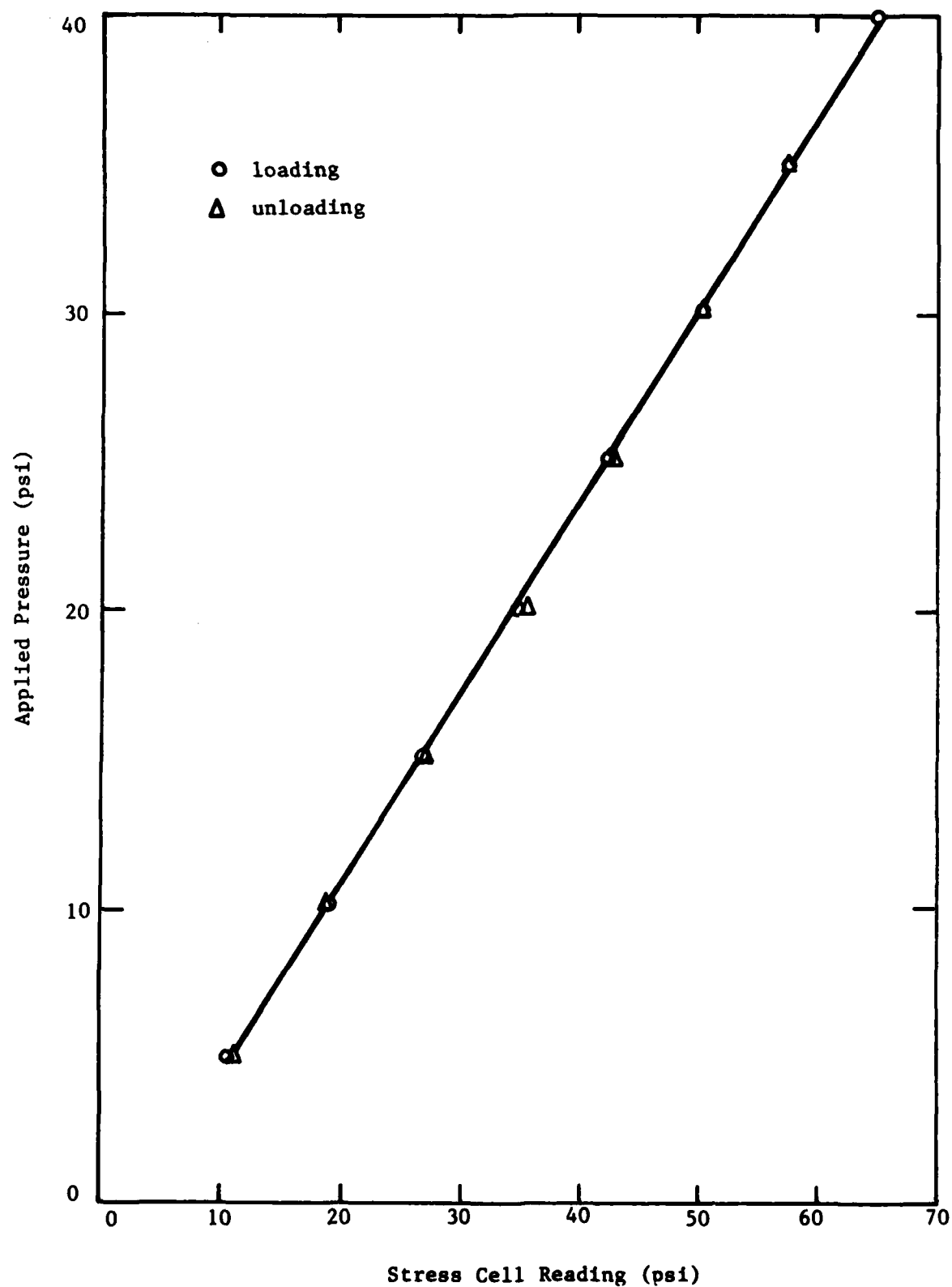


Fig. 2.17 Calibration Curve for Stress Cell SS-3

al for each pair of strain sensors. With an initial null amplitude reading from the control unit (prior to any strain), the calibration factor can be obtained from the calibration curve. Then, strains can be obtained by multiplying this factor by the difference in amplitude readings due to soil movement. One of the calibration curves obtained is shown in Fig. 2.18, and the remainder are included in Appendix A.

As an example of use of the calibration curves, assume the initial null amplitude for the strain sensor SN-1 is 600, the corresponding calibration factor is 0.0505 percent per unit amplitude change as shown in Fig. 2.18. Now, assume the null amplitude for the strain sensor SN-1 is 598 after a pressure of 10 psi (68.9 kPa) is applied. Therefore, the change in amplitude reading is -2, which multiplied by the calibration factor (0.0505) gives the resulting strain as -0.101 percent (negative for compression).

## 2.6 SUMMARY

The same 7-ft (2.1 m) cubical loading device used by Kopperman et al (1982) and Knox et al (1982) was used in the present series of tests, except that the following additions and improvements were made to the testing facilities: 1. a bin for storing dry sand was constructed, 2. a new rainer for placing the sand was built, 3. strain



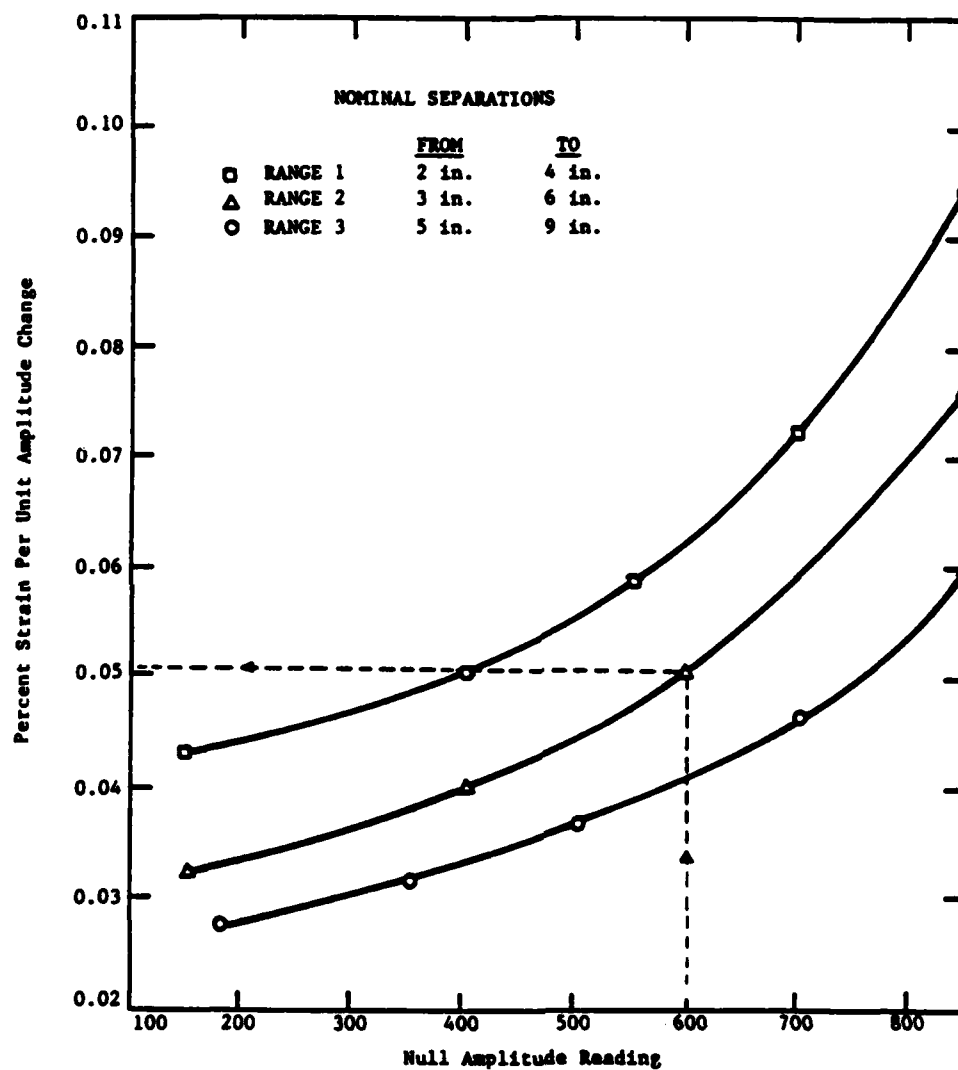


Fig. 2.18 - Strain Calibration for Strain Sensor SN-1

gages were mounted on each excitation port to control the pressure applied at the ports, 4. accelerometers, stress cells and strain cells were calibrated, and 5. additional accelerometers were included to provide more complete data for an attenuation study and to monitor shear waves polarized obliquely. After the above items were completed, the sand specimen was built and a series of tests was commenced as discussed in the following chapters.

## CHAPTER THREE

### TESTING PROGRAM AND PROCEDURES

#### 3.1 INTRODUCTION

The main purposes of this project were to improve the test facility as discussed in Chapter Two and then to perform a series of tests on the same sand used by Knox et al (1982) and Kopperman et al (1982). This series of tests would include all of tests performed earlier as well as additional tests under anisotropic states of stress. These tests would then be used to check the validity of the conclusions reported by Kopperman et al (1982) as well as to extend the earlier work.

The first step in the test program was to empty the sand from the triaxial device. (However, before the device was emptied, Knox and Kopperman performed some tests with the writer and S. Lee before they left so that the basic technique in performing the tests could be demonstrated.) Once the device was emptied, improvements and calibration of the instruments as discussed in Chapter Two were pursued. Upon completion of this work, the device was filled following the procedures reported by Kopperman et al (1982) with the same sand that was originally in the device. Dynamic testing was then performed under the states

of isotropic confinement ( $\bar{\sigma}_1 = \bar{\sigma}_2 = \bar{\sigma}_3$ ), biaxial confinement ( $\bar{\sigma}_1 > \bar{\sigma}_2 = \bar{\sigma}_3$  or  $\bar{\sigma}_1 = \bar{\sigma}_2 > \bar{\sigma}_3$ ), and triaxial confinement ( $\bar{\sigma}_1 > \bar{\sigma}_2 > \bar{\sigma}_3$ ). After each sequence of testing, data were reduced and analyzed before performing the next sequence of testing so that additional insight and better understanding and planning for the next sequence could be obtained.

Kopperman et al (1982) and Hoar and Stokoe (1978) have shown that measurements of interval velocities (velocities determined from travel times between receivers) represent more correctly the material than direct velocities (velocities determined from travel times between the source and receivers). Therefore, only interval velocity measurements were made, and the triggering system used by Knox and Kopperman was unnecessary and, hence, deleted.

### 3.2 EMPTYING OF THE TRIAXIAL DEVICE

The emptying process commenced near the start of February, 1982 and took about three months to finish. The top cover of the triaxial device was first removed with the help of an overhead crane. Water was then bled from the top membrane after which the membrane was removed. The next step in the process was removal of sand. Sand was removed with the aid of a concrete bucket which was raised to the top of the triaxial device using a fork-lift and sand was shovelled into

the bucket. It was soon found that this emptying process was very labor intensive, especially after the upper two ft (61 cm) of sand was removed and the remainder had to be emptied with a shovelling action that required the shovel to be raised over the shoulder in order to dump sand into the bucket. The first half of the sand in the triaxial device was stored in the new storage bin (Section 2.2), and the remainder was stored in an open-air bin outside the Laboratory.

Once the sand was lowered to the level of the embedded instrumentation, the shovelling action became very slow and tedious. The instrumentation was carefully uncovered, and the locations of all instruments were measured and found to agree closely with the locations reported by Kopperman et al (1982). These measurements were performed as a check on the earlier work and to make sure no mass movement of sand had unknowingly occurred. After all instruments were removed and the triaxial device was completely emptied, efforts were directed to calibration of the instrumentation (Sections 2.4 and 2.5).

Emptying the triaxial device took three months because of:

1. careful checking of instrumentation locations, and
2. injury of S. Lee during the emptying process.

### 3.3 SAMPLE CONSTRUCTION

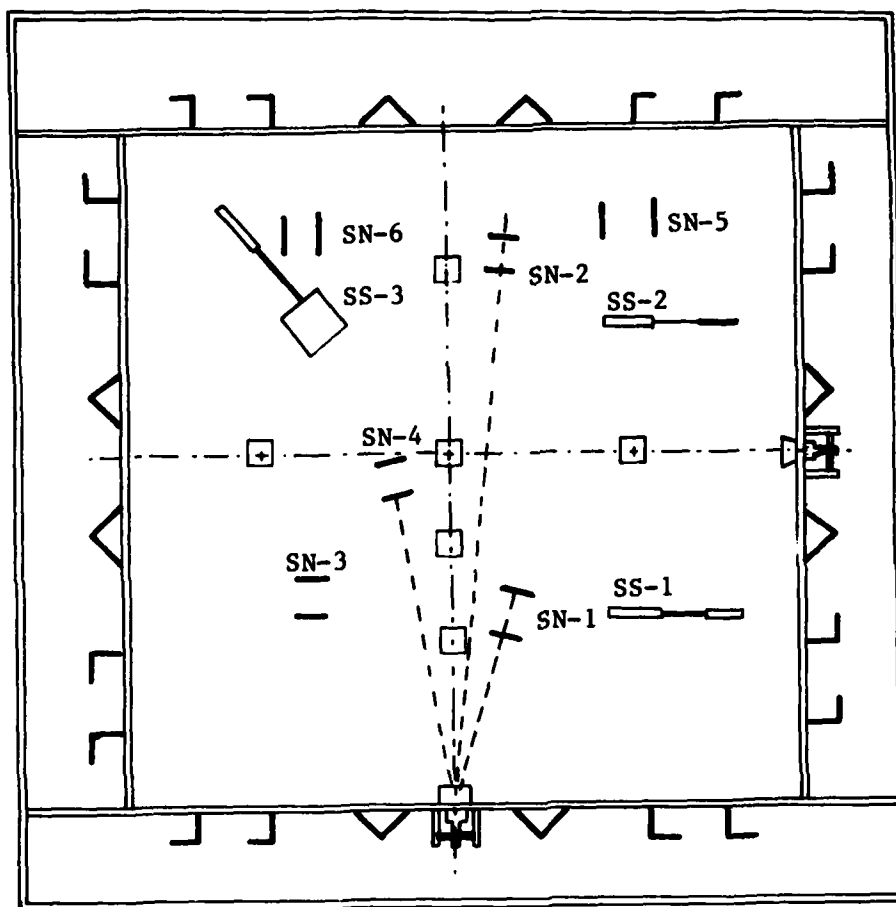
A new test specimen was constructed following the procedures reported by Kopperman et al (1982). The inside of the triaxial device and membranes were first cleaned. One membrane was then hung on the north and south walls. Two plastic sheets with WD-40 oil in between were placed on the bottom and four side walls inside the triaxial device. Filling of sand into the device then started in early August, 1982.

The sand in the new storage bin was used first to fill the triaxial device. With the small trap door near the base of the bin, sand was allowed to flow out of the bin and into a concrete bucket which was placed next to the trap door. It took less than ten minutes to fill the bucket which was then moved inside the Ferguson Laboratory with a fork-lift. An overhead crane was used to lift the bucket so that the sand could be unloaded into the new rainer which was located on the reinforced collar above the triaxial device (Section 2.3). Once the rainer was full (one bucket of sand was enough to fill the rainer), the trap doors under the rainer were opened by about one in. (2.5 cm), and the rainer was moved from side to side in the east-west direction to rain the sand into the triaxial device. It took about twenty min-

utes to empty a rainer full of sand. The raining process proceeded satisfactory with the new rainer.

After all sand in the storage bin had been used, sand from the open-air bin was used. Dry sand was shovelled into the bucket, and the same filling process followed. However, since there were several heavy rainfalls during this time, sand in this storage bin became wet and had to be spread out on the concrete floor and dried in the sun before it could be used. This drying operation slowed the filling process significantly and also made it laborious. (It is recommended that a second storage bin be constructed so that all sand required to fill the triaxial device can be stored in dry areas.) Moisture measurements showed that the sand placed in the triaxial device had a moisture content less than 0.05 percent.

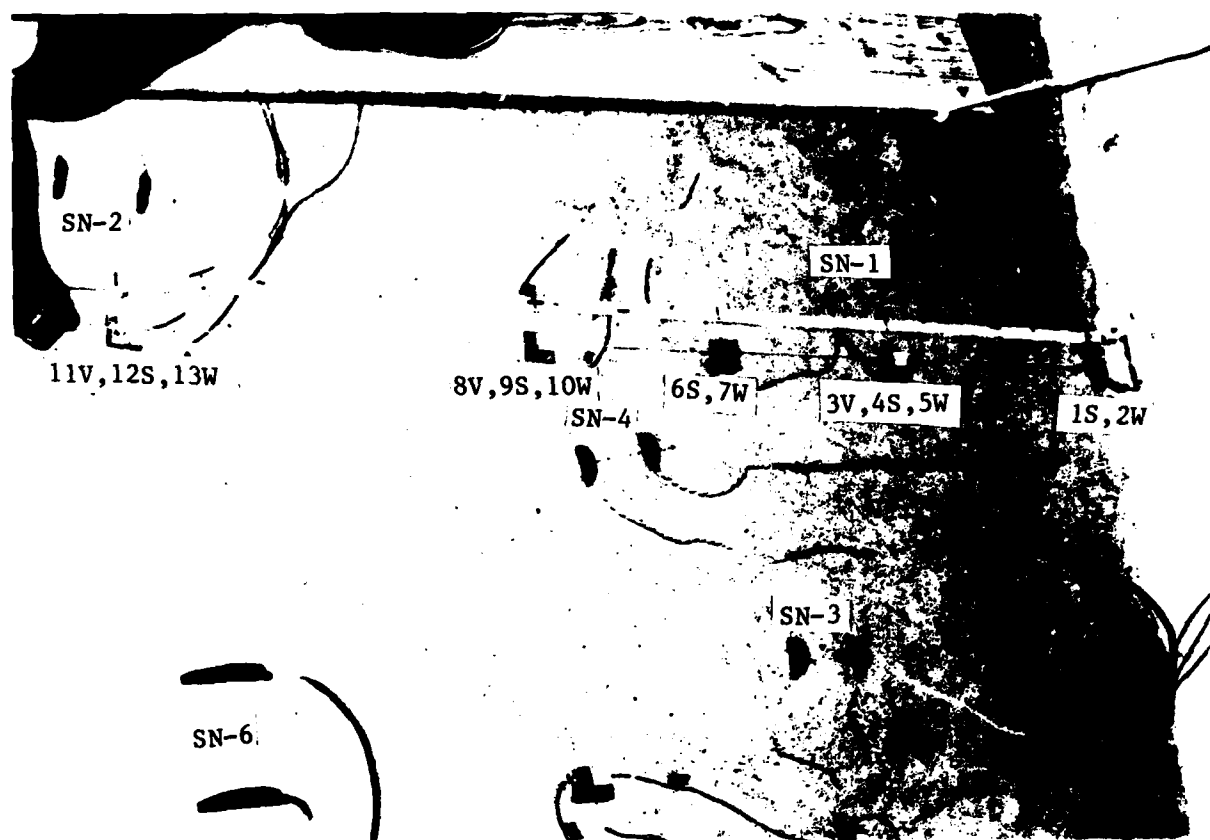
The filling process was halted at the eight elevations where instruments were to be placed as shown in Fig. 2.11. However, most instruments were placed at the mid-depth plane as detailed in Fig. 3.1. Pictures of the instruments are shown in Figs. 3.2 and 3.3. Since the overhead crane was often not available because of other commitments at the Laboratory, a wooden platform was hung inside the triaxial device with ropes tied to the four castors of the rainer as shown in Fig. 3.4. This was done so that one could climb (carefully) into the



- Legend:
1. 2-D or 3-D Accelerometers
  2. SS-1 to SS-3 stress cells (which are actually 6 in. above the mid-depth plane)
  3. SN-1 to SN-4: 2 in. strain sensors
  4. SN-5 to SN-6: 4 in. strain sensors

Fig. 3.1 - Instrumentation at Mid-Depth Plane in Triaxial Device





- Legend:
1. 1S to 13W: accelerometer levels; letter following accelerometer number indicates direction of sensitivity (see Fig. 2.11)
  2. SN-1 to SN-4: 2-in. strain sensors
  3. SN-6 : 4-in. strain sensors

Fig. 3.2 - Instruments Being Placed at the Mid-Depth Plane

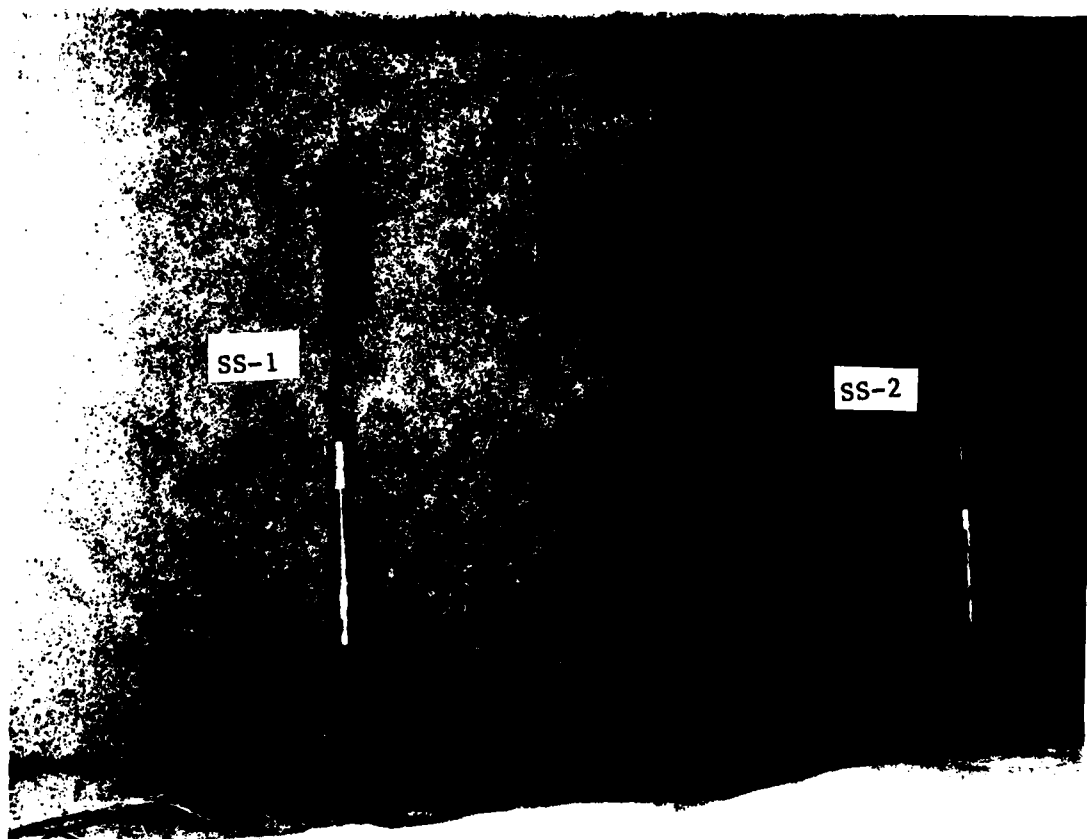


Fig. 3.3 - View Showing Stress Cells in North-South Direction

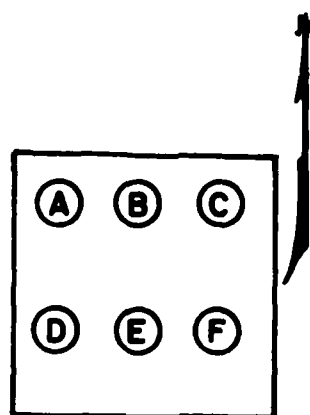


- Legend:
1. Dispersion screen on rainer
  2. Rope
  3. Working platform
  4. Wooden collar of sand raining system
  5. Membrane on north wall

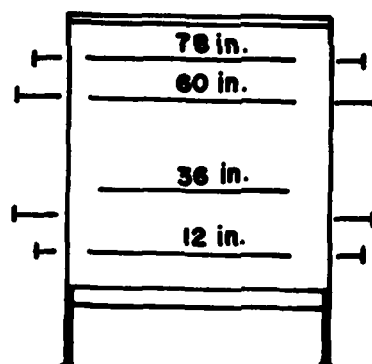
Fig. 3.4 - View of Working Platform Supported by Ropes Attached to Rainer

triaxial device and use the platform as a working area without disturbing the sand. This platform was used to place all embedded instrumentation.

The filling process was also stopped at four elevations where density measurements were taken. The same density devices used by Knox and Kopperman were used. These devices are three cylindrical containers made of 0.25-in. (0.64 cm) thick plexiglass. The containers have an internal diameter of 6 in. (15.2 cm) and a height of 3 in. (7.6 cm), which results in a volume of 8.64 in.<sup>3</sup> (0.05 ft<sup>3</sup> or 142 cm<sup>3</sup>). The top edge of the cylinder is machined to an angle of 45 degrees sloping out to minimize sand bouncing into the container upon striking the container during the raining process, which might alter the compactness of the density specimen. The elevations and locations for density measurements are shown in Fig. 3.5, and the results are listed in Table 3.1. The average density is 101.8 pcf (1629 kg/m<sup>3</sup>), and the standard deviation is 2.0 pcf (32 kg/m<sup>3</sup>), less than 2 percent of the mean value. Compared to values obtained by Kopperman et al, 1982 ( mean value and standard deviation of 96.6 pcf and 1.9 pcf, respectively), the sample is denser than before, with density 5.4 percent higher. In terms of average void ratio, the new sample has a value of 0.64 and is 12 percent lower than the value of 0.73 reported by Kopperman et al. The values of standard deviation show the same amount of experimental scatter



(a) Plan View of Measurement Locations



(b) Elevations Where Raining of Sand was Halted for Measurements

Fig. 3.5 - Locations of Density Measurements Performed During Filling of Triaxial Device

TABLE 3.1

Densities and Void Ratios of Sand  
at Various Elevations in the Triaxial Device

Height Above the Bottom (in.)	Location (see Fig. 3.5)	Density $\gamma$ (pcf)	Void Ratio $e^*$
12	A	103.1	0.62
12	E	99.7	0.68
12	C	101.8	0.64
36	D	103.5	0.62
36	B	100.8	0.66
36	F	104.8	0.60
60	A	102.6	0.63
60	B	98.8	0.69
60	F	103.3	0.62
78	D	103.3	0.62
78	E	98.6	0.70
78	C	101.3	0.65
Average		101.8	0.64
Std. Deviation		2.0	0.03

$$* e = \frac{\gamma_w \cdot G_s}{\gamma_d} - 1 \quad \text{where } G_s = 2.68,$$

$$\gamma_d = \frac{\gamma}{1+w}, \text{ and}$$

$$w = 0.05\%$$

for both samples. The new rainer apparently builds a denser sample but not necessarily a more homogeneous sample than before.

### 3.4 DYNAMIC TESTING

Construction of the sample was finished in early October, 1982. A series of dynamic tests was then performed for isotropic confinement, followed by a series of tests with biaxial confinement. Unfortunately the top membrane started to leak in early January, 1983. This forced testing to be halted. The top membrane was removed, and locations of leakage were found. Due to the special construction of the membrane, the repair cost was unreasonable compared to the cost of a new membrane. Therefore, a new membrane was ordered from Goodyear Aerospace Corporation at Rockmart, Georgia, the same company that built the old membranes. In April, 1983, the new membrane was delivered. Testing was resumed in May, 1983, and was completed in late May, 1983.

The loading history for all series of tests is summarized in Table 3.2. The history is also shown in Fig. 3.6 for the isotropic and biaxial testing series before the membrane leaked and Fig. 3.7 for the biaxial and triaxial testing series after the new membrane was installed.

TABLE 3.2  
Loading Pressure Sequences

Test No.	Date of Test	Vertical Effective Stress $\bar{\sigma}_{TB}$ (psi)*	Horizontal Effective Stresses	
			$\bar{\sigma}_{NS}$ (psi)*	$\bar{\sigma}_{EW}$ (psi)*
1	10/08/82	10	10	10
2	10/13/82	15	15	15
3	10/16/82	20	20	20
4	10/16/82	30	30	30
5	10/20/82	40	40	40
6	10/23/82	30	30	30
7	10/23/82	20	20	20
8	10/23/82	15	15	15
9	10/23/82	10	10	10
10	11/08/82	15	15	15
11	11/10/82	20	15	15
12	11/12/82	30	15	15
13	11/13/82	40	15	15
14	11/13/82	40	20	20
15	11/15/82	40	30	30
16	11/28/82	40	40	40
17	12/17/82	40	30	30
18	12/17/82	40	20	20
19	12/17/82	40	15	15
20	12/18/82	30	15	15
21	12/18/82	20	15	15
22	12/18/82	15	15	15
23	12/18/82	20	20	20
24	12/20/82	30	20	20
25	12/20/82	40	20	20
26	12/20/82	15	20	20
27	12/21/82	10	20	20
28	12/21/82	20	10	20
29	12/21/82	20	15	20
30	12/22/82	20	30	20
31	12/22/82	20	40	20



TABLE 3.2  
Loading Pressure Sequences  
(Continued)

Test No.	Date of Test	Vertical Effective Stress $\bar{\sigma}_{TB}$ (psi)*	Horizontal Effective Stresses	
			$\bar{\sigma}_{NS}$ (psi)*	$\bar{\sigma}_{EW}$ (psi)*
32	12/22/82	30	30	30
33	01/05/83	40	40	40
34	01/06/83	20	30	20
35	01/06/83	20	20	20
36	01/06/83	20	15	20
37	01/07/83	20	10	20
38	01/07/83	15	15	15
39	01/07/83	15	20	15
40	01/08/83	15	30	15
41	01/08/83	15	40	15
42	01/08/83	20	40	20
43	01/10/83	30	40	30
44	01/10/83	20	40	20
45	01/10/83	15	40	15
46	01/11/83	15	30	15
47	01/11/83	15	20	15
48	01/11/83	15	15	20
49	01/11/83	15	15	30
50	01/12/83	15	15	40
51	01/12/83	20	20	40
52	01/12/83	30	30	40
53	05/19/83	30	30	30
54	05/20/83	40	40	40
55	05/20/83	30	30	40
56	05/20/83	20	20	40
57	05/21/83	15	15	40
58	05/23/83	15	15	30
59	05/23/83	15	15	20
60	05/24/83	15	15	15

Table 3.2  
Loading Pressure Sequences  
(Continued)

Test No.	Date of Test	Vertical Effective Stress $\bar{\sigma}_{TB}$ (psi)*	Horizontal Effective Stresses	
			$\bar{\sigma}_{NS}$ (psi)*	$\bar{\sigma}_{EW}$ (psi)*
61	05/24/83	40	25	20
62	05/24/83	40	15	25
63	05/24/83	40	15	30
64	05/24/83	40	15	35
65	05/25/83	28	28	28
66	05/25/83	32	28	24
67	05/25/83	36	28	20
68	05/25/83	40	28	16
69	05/26/83	28	28	28
70	05/26/83	32	31	24
71	05/26/83	36	34	20
72	05/26/83	40	37	16

\* $\bar{\sigma}_{TB}$  = Vertical (top-bottom) effective stress

$\bar{\sigma}_{NS}$  = Horizontal (north-south) effective stress

$\bar{\sigma}_{EW}$  = Horizontal (east-west) effective stress

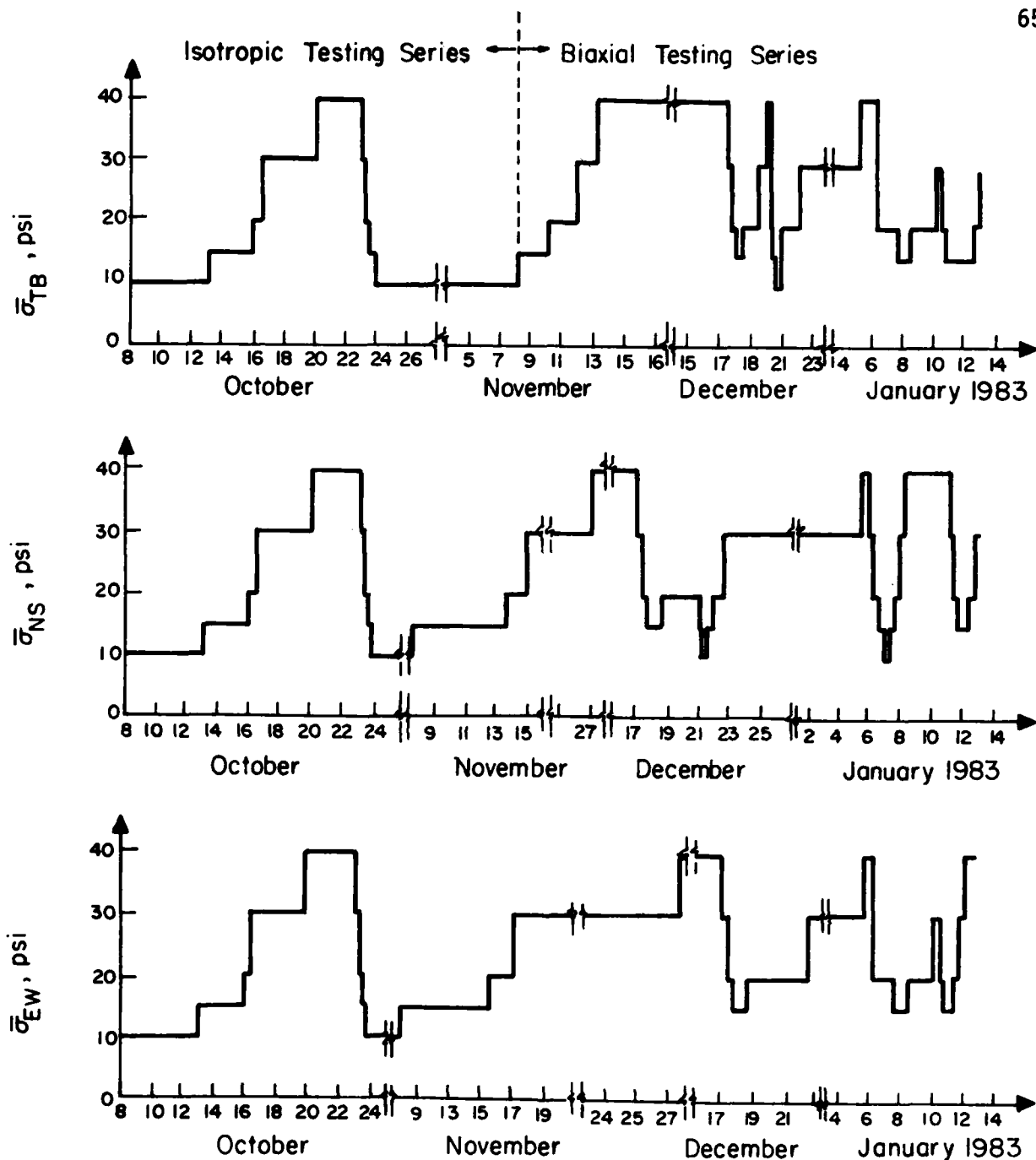


Fig. 3.6 - Loading History in Each Principal Stress Direction from Start of Testing Until Membrane Ruptured

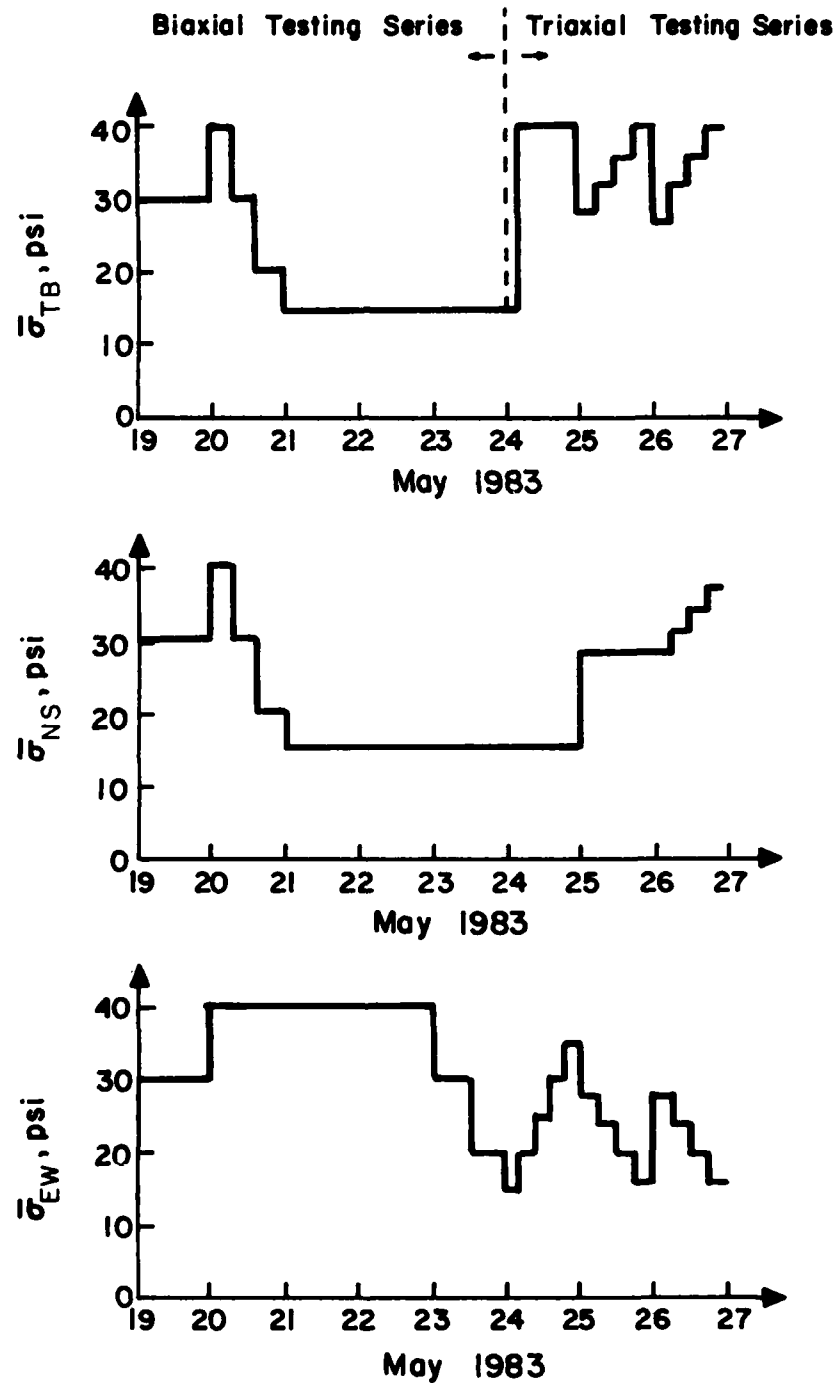


Fig. 3.7 - Loading History in Each Principal Stress Direction After New Membrane Installation

### 3.5 COMPRESSION WAVE ANALYSIS

Waveforms of the compression wave were monitored under each confining pressure and were recorded on magnetic disks using two digital oscilloscopes. These records were brought back to the main campus for analyses from which propagation velocities, frequencies, and strain amplitudes were determined with procedures detailed in the following sections.

#### 3.5.1 Determination of Propagation Velocity

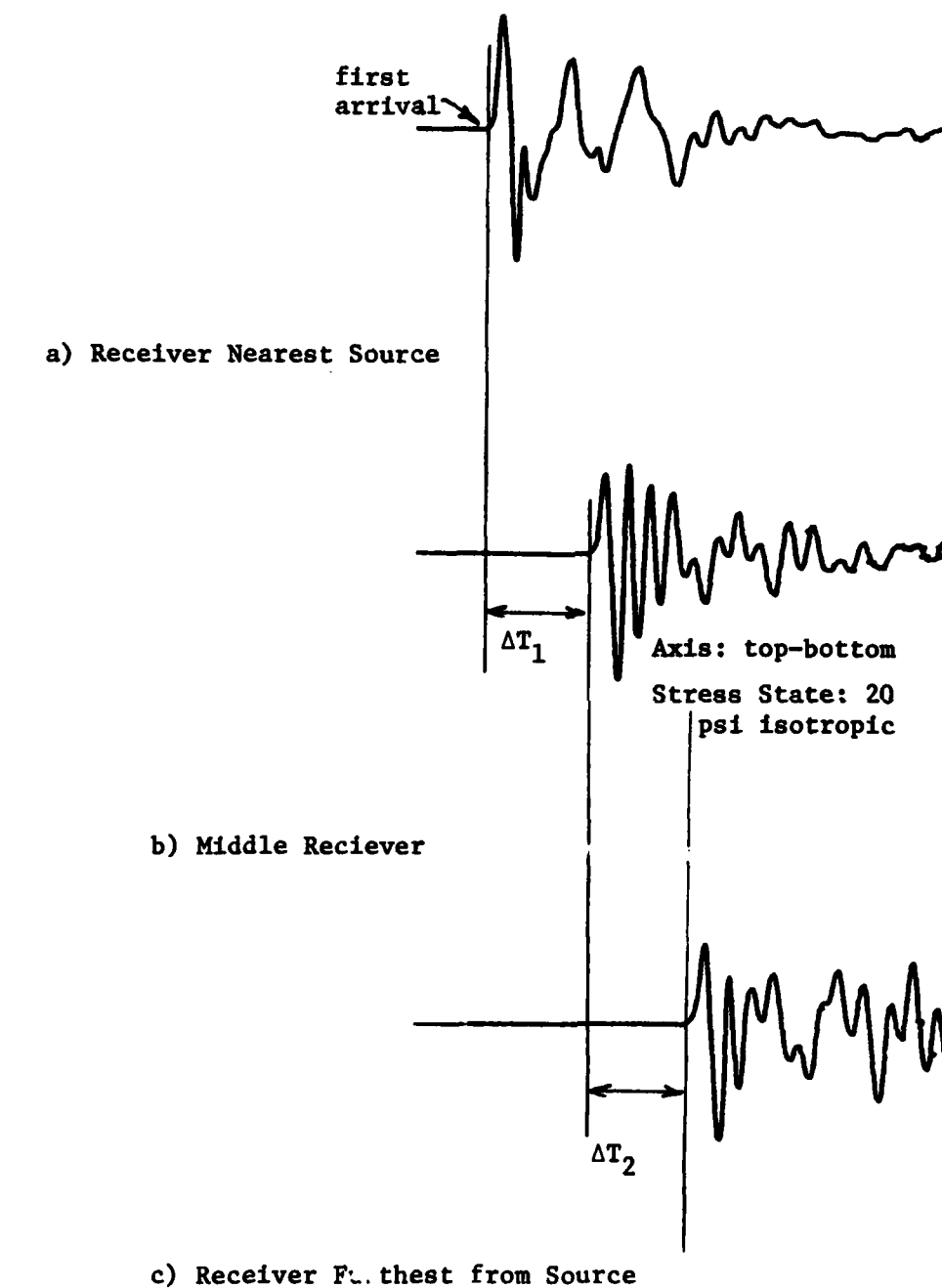
With known distances between accelerometers (which were measured from the center of one accelerometer to the center of next accelerometer during sample construction) and measured travel times of the waves, wave propagation velocities were simply calculated by dividing the distances by the corresponding travel times. The distances used in the analysis are summarized in Table 3.3. The waveforms recorded on the magnetic disks were recalled using the same digital oscilloscopes used in collecting the waves, and travel times were estimated from first arrivals of the waves at each accelerometer. A plotting of typical waveforms illustrating this procedure is shown in Fig. 3.8.

TABLE 3.3

## Distances Between Accelerometers Inside the Triaxial Device

Accelerometer <u>From</u>	Labels* <u>To</u>	<u>Distance (ft)</u>
1S	4S	1.13
4S	6S	0.99
6S	9S	0.99
9S	12S	2.00
16W	10W	2.07
10W	19W	2.06
20V	8V	2.00
8V	27V	2.00
2W	5W	1.13
5W	7W	0.99
7W	10W	0.99
10W	13W	2.00
3V	8V	1.98
8V	11V	2.00
15V	9S	2.07
9S	18S	2.06
14V	8V	2.07
8V	17V	2.06
21S	9S	2.00
9S	28S	2.00
22W	10W	2.00
10W	29W	2.00
23	25	2.00
24	26	2.00

\*See Fig. 2.11 for Accelerometer Locations



Legend:  $\Delta T_1$  = interval travel time from a to b  
 $\Delta T_2$  = interval travel time from b to c

Fig. 3.8 - Determination of Compression Wave Travel Times from a Set of Three Accelerometer Records

### 3.5.2 Determination of Predominant Frequency

The predominant frequency of the compression wave was determined from two fractional values of the period,  $0.25T$  and  $0.50T$ , measured from each accelerometer record as shown in Fig. 3.9. These frequencies were then used to estimate strain amplitudes and the wavelengths as discussed in Sections 3.5.4 and 3.5.5, respectively. Only rough approximations of the values were of concern. Hence, only four sets of records were used in the analysis : two sets for the isotropic state of confinement, one set for the biaxial state of confinement and one set for the triaxial state of confinement. Each set of records contained all the compression waves propagating along each principal axis under the particular stress state.

Values of predominant frequency determined from  $0.25T$  varied from 500 Hz to 2632 Hz with an average of 1287 Hz and standard deviation of 426 Hz. Values of predominant frequency determined from  $0.50T$  varied from 1205 Hz to 5882 Hz with an average of 2400 Hz and standard deviation of 1044 Hz. Frequencies determined from  $0.50T$  were much higher than those from  $0.25T$  due to the phenomenon of a slow rise time of the initial pulse. The average frequency for all measured values from both  $0.25T$  and  $0.50T$  was 1830 Hz.



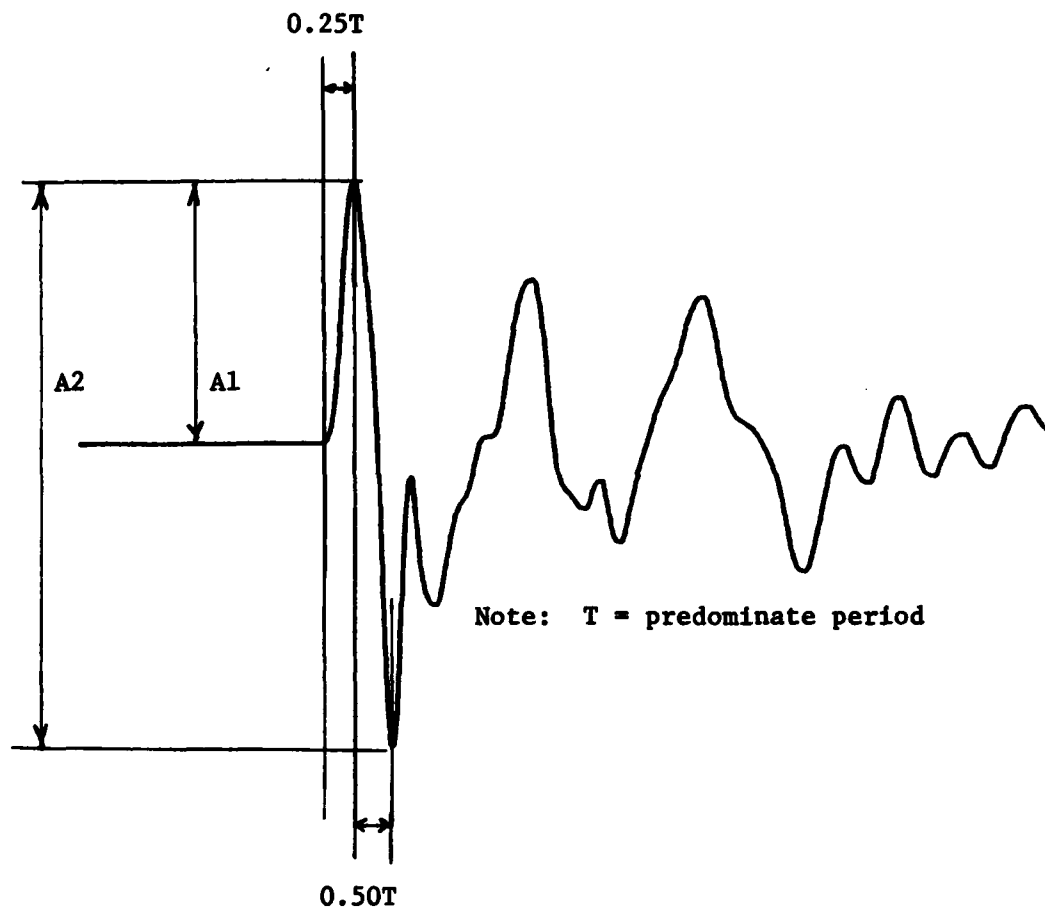


Fig. 3.9 - Determination of Particle Amplitudes and Predominant Periods from a Typical Accelerometer Record

### 3.5.3 Determination of Peak Acceleration

Two amplitudes of each wave form were determined from the same four sets of records. The amplitudes determined were the first-peak (or trough) amplitude,  $A_1$ , and the first peak-to-peak amplitude,  $A_2$ , as shown in Fig. 3.9.

The charge amplifiers used with the accelerometers were calibrated so that the product of the sensitivity dial and the full-scale switch was equal to the number of picocoulombs (pc) which will produce the full-scale output of 20V peak-to-peak. As an example, let the product be 100 pc and the sensitivity of a typical accelerometer be 100 pc/g. Therefore, an acceleration of one g ( $32.2 \text{ ft/s}^2$  or  $9.8 \text{ m/s}^2$ ) peak-to-peak would produce an output of 20V. With measured values of  $A_1$  and  $A_2$  in volts, peak and peak-to-peak accelerations of each wave were determined. Values of peak acceleration ranged from 0.007g to 0.564g ( $0.23$  to  $18.0 \text{ ft/s}^2$  or  $0.069$  to  $5.5 \text{ m/s}^2$ ) with an average of 0.124g ( $3.99 \text{ ft/s}^2$  or  $1.22 \text{ m/s}^2$ ). The average of peak-to-peak accelerations was 0.275g ( $8.86 \text{ ft/s}^2$  or  $2.70 \text{ m/s}^2$ ) and was about twice the peak acceleration.

### 3.5.4 Determination of Strain Amplitude

It is well known that the linear strain amplitude,  $\epsilon$ , for a plane wave can be determined from the particle velocity,  $\dot{u}_p$ , and propagation velocity,  $V_p$ , as follows :

$$\epsilon = \frac{\dot{u}_p}{V_p} \quad (3.1)$$

and

$$\dot{u}_p = (2\pi f)A \quad (3.2)$$

where:  $f$  = wave frequency, and

$A$  = peak particle amplitude.

Using a harmonic approximation, the peak acceleration,  $\ddot{z}$ , can be related to peak amplitude as follows:

$$\ddot{z} = (2\pi f)^2 A \quad (3.3)$$

which means:

$$\dot{u}_p = \frac{\ddot{z}}{2\pi f} \quad (3.4)$$

From Eqs. 3.1 and 3.4, the relationship between strain amplitude, acceleration, frequency, and compression wave velocity for a plane wave is:

$$\epsilon = \frac{\ddot{z}}{(2\pi f)V_p} \quad (3.5)$$

The sources in the triaxial device tend to generate spherical waves while Eq. 3.5 is derived for plane waves with harmonic excitation. Therefore, values of strain amplitude computed by the equation can only be used as an approximation to reflect the order of magnitude of the strains in the sand in the triaxial device. To estimate the maximum strain amplitude, the smallest values of frequency and compression wave velocity together with the largest peak acceleration amplitude gives a strain amplitude of about 0.0005 percent. Since this is less than 0.001 percent, testing may be considered to be low amplitude and the effect of strain amplitude can be ignored.

### 3.5.5 Determination of Wavelengths

With known values of compression wave velocity,  $V_p$ , and frequency,  $f$ , the wavelength,  $\lambda$ , can be computed from the following equation:

$$\lambda = \frac{V_p}{f} \quad (3.6)$$

Using the average minimum velocity of 1340 ft/s (409 m/s) and the average maximum velocity of 1980 ft/s (604 m/s) together with an average

frequency of 1830 Hz, the range in wavelengths was 0.73 ft to 1.08 ft (0.22 m to 0.33 m) in the sand in the triaxial device.

As discussed in Section 6.2.5 by Kopperman et al (1982), the wavelengths must be short enough so that the full wave passes by any receiver before any reflected wave reaches the receiver in order to obtain waveforms that are easily interpretable. This critical distance is twice the distance between the receiver furthest from the source and the wall opposite the source. In this series of tests, the accelerometers were positioned such that this distance is about 3 ft (0.92 m) which is more than twice the longest wavelength. Therefore, the wavelengths are short enough to be read without interference from reflections.

Conversely, the wavelength should be long enough so that the accelerometer block properly tracks particle motions in the sand. If the wavelength is too small, the block acts as a boundary rather than as a part of the sand specimen. The accelerometer blocks embedded in the sand are 1.75 in. (44 mm) square. Since the minimum wavelength is 0.73 ft (8.8 in. or 220 mm) which is five times the dimension of the block, wavelengths may be considered as long enough to have waves that are easy to interpret (Suddhiprakarn et al, 1983).

### 3.6 SUMMARY

The triaxial device used by Knox et al (1982) and Kopperman et al (1982) was first emptied. Improvements and calibration of the instruments as discussed in Chapter Two were pursued. Then, a sample of the same sand was constructed using the new raining device (Section 2.3). The filling process was halted at elevations where instruments were to be placed and density measurements were taken. The locations of instruments are shown in Figs. 2.11 and 3.1. The average density of the sample is 101.8 pcf ( $1629 \text{ kg/m}^3$ ).

Once the sample was constructed, series of dynamic tests were performed for isotropic confinement, biaxial confinement and triaxial confinement. The loading history for all series of tests is summarized in Table 3.2 and shown in Figs. 3.6 and 3.7. Analysis for waveforms of the compression wave collected under each test is presented in Section 3.5. Propagation velocity of each P-wave is determined and relationship between P-wave velocity and states of confinement is studied and presented in Chapters 4, 6 and 7.

## CHAPTER FOUR

### ISOTROPIC CONFINEMENT

#### 4.1 INTRODUCTION

The first step in the study of the effect of confining pressure on compression wave velocity was to perform tests with isotropic confinement. This state of confinement is the simplest state that can be applied with the triaxial device, and the effect of stress state on velocity is the easiest to analyze. Moreover, this state of confinement eliminates stress as a contributing factor for different values of P-wave velocity measured along each of the principal axes and thus permits evaluation of structural anisotropy (also called inherent anisotropy).

Compression wave velocities were measured at various isotropic states of stress ranging from 10 psi (69 kPa) to 40 psi (276 kPa). To obtain isotropic loading, confining pressures were applied so that stresses along all three principal axes of the triaxial device were the same ( $\bar{\sigma}_1 = \bar{\sigma}_2 = \bar{\sigma}_3$ ). However, in reality, true isotropic confinement could not be achieved at all points within the triaxial device because of small inherent pressure gradients. In the vertical direction, there was a slight increase in stress with depth caused by the

weight of sand. The change in vertical stress from top to bottom of the device was less than 5 psi (34.5 kPa), or less than  $\pm 2.5$  psi (17 kPa) from the value applied at the center of the device. For stresses applied in the horizontal directions, the hydraulic head of water in the membranes caused a change in stress from top to bottom of the device of about 3 psi (20.7 kPa), or less than  $\pm 1.5$  psi (10.3 kPa) from the value applied at the mid-height of the device. The largest vertical distance away from the mid-height of the specimen to any accelerometer was 2 ft (0.61 m) as shown in Fig. 2.11. Therefore, variations in pressures in the area over which data were collected were  $\pm 1.4$  psi (9.6 kPa) and  $\pm 0.86$  psi (5.9 kPa) in the vertical and horizontal directions, respectively. Within the range of isotropic pressures, namely 10 to 40 psi (69 to 276 kPa), variations in pressures over the area of interest were 3.5 to 14 percent and 2.2 to 8.6 percent in the vertical and horizontal directions, respectively. These pressure gradients were small and were considered negligible.

Values of all pressures reported in this study represent the values of pressures applied at the center of the triaxial device. To account for the effects of overburden pressure, hydraulic gradient, and different piezometric elevations between the membranes and pressure panel board, the following corrections were applied to the pressure gage readings :



$$\text{vertical correction : } P_G = P_C - 0.21 \text{ psi}$$

$$\text{horizontal correction : } P_G = P_C + 0.72 \text{ psi}$$

where :  $P_G$  = reading on pressure gage at panel board, in psi, and

$P_C$  = pressure at center of triaxial device, in psi.

These corrections were derived for a constant difference in elevation between the top or center of the device and the air/water interface at the panel board, namely for a 10-in. (25 cm) high column of water in the accumulator on the panel board. It was difficult to keep the water column in the accumulator at a constant elevation throughout measurements at a particular set of confining pressures. A change in elevation of the water level in the accumulator of one in. (2.5 cm) would result in about a 0.04 psi (0.25 kPa) change in pressure, and a change of the entire 18-in. (45.7 cm) high accumulator would result in only a 0.65 psi (4.48 kPa) change in pressure. Therefore, with the effort that was made to maintain the water level at an approximately constant elevation, any set of pressures can be considered constant (within 0.2 psi (1.4 kPa)).

The method of data analysis is discussed in Section 3.5. The effect of stress history on P-wave velocity was studied first. Then, the effect of structural (inherent) anisotropy and variation of P-wave velocity with isotropic loading were studied.

#### 4.2 EFFECT OF STRESS HISTORY

An initial series of tests was performed under isotropic loading with confining pressures increased from 10 psi (69 kPa) to 40 psi (276 kPa). The sand specimen was then unloaded isotropically to 10 psi (69 kPa). At each state of isotropic confinement, compression wave velocities were determined as the average of two interval velocities (Section 3.1) along each of the principal axes, except for the north-south axis along which three interval velocities (provided by additional accelerometers used for an attenuation study) were used to obtain the average velocities.

It is worthwhile to examine first the scatter in the interval velocities along each axis. Along the north-south axis, the intermediate-interval velocity was always less than the near-interval velocity, with the average value of the ratio of these two velocities being 0.98. On the other hand, the far-interval velocity was always greater than the intermediate-interval velocity. The ratio of these two velocities averaged 1.14. Similarly, the ratio of the far-interval velocity to the near-interval velocity along the vertical axis had an average value of 1.08. Along the east-west axis, the ratio of the far-interval velocity to the near-interval velocity averaged 1.005. All of these variations show the inherent scatter in the system. Since the differ-

AD-A151 059

EFFECTS OF STRUCTURAL AND STRESS ANISOTROPY ON VELOCITY  
OF LOW-AMPLITUDE. (U) TEXAS UNIV AT AUSTIN GEOTECHNICAL  
ENGINEERING CENTER S H LEE ET AL. JUN 84

2/2

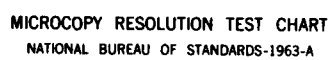
UNCLASSIFIED

AFOSR-TR-85-0089 AFOSR-83-0062

F/G 8/13

NL

END



ences were not large, average values of the interval velocities were used in all analyses.

Compression wave velocities determined from averages of interval velocities were plotted against the corresponding confining pressure on log-log paper for each of the principal axes as shown in Fig. 4.1. Straight lines were fitted to the data for loading and unloading separately using a least-squares method. As shown in Fig. 4.1, straight lines for the unloading data have slightly flatter slopes than those for the loading data which results in the values of  $m$  being greater upon loading. This effect is most important at the lowest pressure. However, the largest variation in  $V_p$  upon loading and unloading is only 6 percent. The hysteresis effect upon  $V_p$  was, therefore, not significant, and averages of values obtained from both loading and unloading were used in all analyses.

Testing at an isotropic state of stress occurred at various times throughout the complete series of tests as summarized in Table 3.2 or as shown in Figs. 3.6 and 3.7. In an attempt to study further the effect of stress history on P-wave velocity, velocities from repeated tests are summarized in Table 4.1. Averages and standard deviations of velocities at each isotropic state of stress were determined for each of the three principal axes. As can be seen in the table, com-

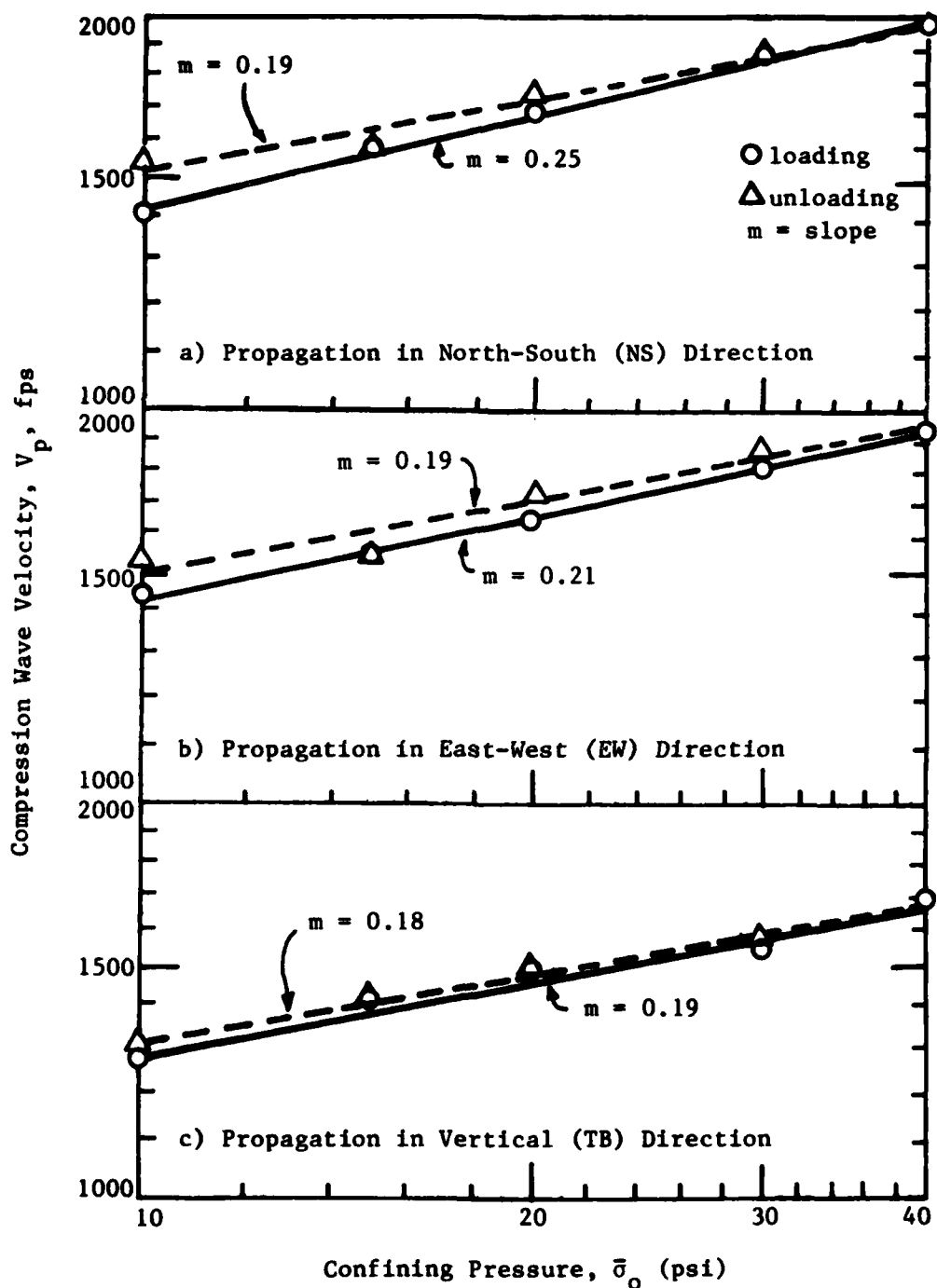


Fig. 4.1 - Effect of Stress History on Variation of P-wave Velocity with Isotropic Confining Pressure

TABLE 4.1

Compression Wave Velocities Measured at Different Times  
Under Similar Isotropic States of Stress

Confining Pressure	Test* No.	P-wave Velocities (fps)		
		HORIZONTAL (north-south)	DIRECTIONS (east-west)	VERTICAL DIRECTION (top-bottom)
10 psi	1	1434	1416	1270
	9	1503	1498	1301
		M** = 1469	M = 1457	M = 1286
		SD** = 49	SD = 58	SD = 22
15 psi	2	1588	1547	1413
	8	1585	1547	1413
	10	1624	1543	1406
	22	1604	1547	1409
	38	1606	1563	1389
	60	1607	1666	1341
		M = 1602	M = 1569	M = 1395
		SD = 14	SD = 49	SD = 28
20 psi	3	1695	1648	1481
	7	1758	1737	1491
	23	1697	1667	1488
	35	1798	1669	1458
		M = 1737	M = 1680	M = 1480
		SD = 50	SD = 39	SD = 15
30 psi	4	1875	1801	1542
	6	1881	1880	1574
	32	1897	1891	1546
	53	1797	1894	1497
		M = 1863	M = 1867	M = 1540
		SD = 44	SD = 44	SD = 32
40 psi	5	1985	1932	1688
	16	1985	1932	1688
	33	2012	1979	1665
	34	1963	1998	1669
		M = 1986	M = 1960	M = 1678
		SD = 20	SD = 34	SD = 12

\*See Table 3.2

\*\* M = mean

SD = standard deviation

pression wave velocities at each confining pressure are close. The maximum percentage differences between any two waves velocities propagating along the same axis under the same confining pressure are small, less than 8 percent for all cases. It should also be noted that the standard deviations are always less than 4.0 percent of the average velocities. Therefore, the scatter of average velocities can be considered small, and the effect of stress history on P-wave velocity is negligible.

#### 4.3 EFFECT OF STRUCTURAL ANISOTROPY

Structural anisotropy is the inherent anisotropy in the soil skeleton which causes a difference in soil properties (including P-wave velocities) in different directions under isotropic loading conditions. (Soil properties will vary with direction if the stresses vary, and this is referred to as stress-induced anisotropy.) A certain amount of structural anisotropy was believed to have been induced in the sample as a result of the raining operation used to build the sample. Therefore, it was necessary to evaluate the magnitude and importance of the effect of structural anisotropy on P-wave velocities before the effect of isotropic confinement could be studied.



The easiest way to study the effect of structural anisotropy on P-wave velocity is to perform tests under isotropic confinement. Therefore, average P-wave velocities summarized in Table 4.1 were plotted against confining pressure using logarithmic paper. The resulting curves are shown in Fig. 4.2 and are represented by the three best-fit straight lines that are almost parallel. The slopes of the straight lines are 0.22, 0.23 and 0.17 for velocities propagating along the north-south (NS), east-west (EW) and vertical (TB) directions, respectively. Additionally, the curves fall into two groups: 1. the two curves for waves propagating along the horizontal directions (NS and EW) in which case the velocities are within 3.5 percent, and 2. the curve for waves propagating along the vertical direction which falls below the other two curves. Therefore, P-wave velocities along the NS and EW directions can be considered the same. As such, no structural anisotropy is present in the horizontal plane which can be considered a plane of isotropy. However, the ratio of velocities of P-waves propagating along the horizontal directions ( $V_{pH}$ ) to those along the vertical direction ( $V_{pV}$ ) varied from 1.16 at 10 psi (69 kPa) to 1.18 at 40 psi (276 kPa). Therefore, structural anisotropy exists between the horizontal and vertical directions. This condition is referred to as cross-anisotropy. (See Section 5.5 for numerical evaluation of this constitutive model.) The average of the ratios of  $V_{pH}$  to  $V_{pV}$  is

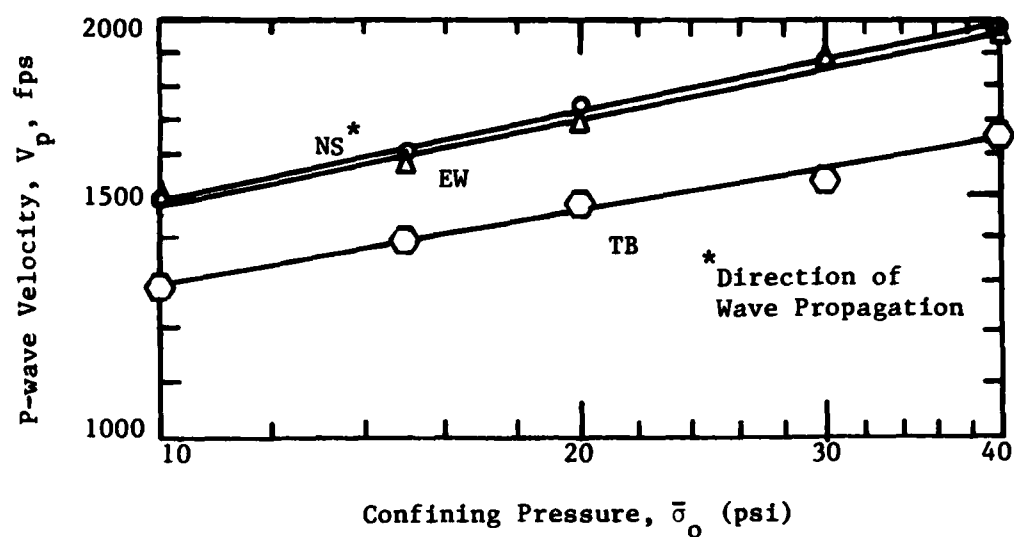


Fig. 4.2 - Effect of Structural Anisotropy on Variation of P-wave Velocity with Isotropic Confining Pressure

1.17. Hence, the wave velocities may be approximated by the following relationship which is independent of stress (provided the stress level is within 10 to 40 psi (69 to 276 kPa)):

$$V_{PH} = 1.17 (V_{PV}) \quad (4.1)$$

Since a pressure gradient exists in the triaxial device (Section 4.1), velocities will increase slightly with depth causing some wave refraction (curved wave path for waves propagating along the horizontal directions). However, the effect of a curved wave path would be small since the receivers are closely spaced when compared to the relative depth of embedment based on confining pressure (Haupt, 1973). The differences in P-wave velocities, therefore, are attributable to structural anisotropy since the same instrumentation and testing technique were used to determine P-wave velocities propagating along each principal axis.

#### 4.4 EFFECT OF ISOTROPIC CONFINEMENT

For the dry sand sample, confining pressure is the same as effective stress (pore water pressure is zero). Also, for isotropic confinement, the confining pressure along each of the three principal axes is the same as the mean effective stress,  $\bar{\sigma}_0$ . Therefore, only one velocity versus pressure plot is needed in the analysis. This plot is

shown in Fig. 4.2 in which the variation in P-wave velocities with  $\bar{\sigma}_0$  can be represented by a linear relationship on a log-log plot for all three axes. The relation shown in Fig. 4.2 can be expressed in power form as used by Hardin and Richart (1963):

$$V_p = C_1 \bar{\sigma}_0^m \quad (4.2)$$

where:  $V_p$  = P-wave velocity, in fps,

$\bar{\sigma}_0$  = isotropic confining pressure, in psf,

$C_1$  = constant ( $C_1 = V_p$  when  $\bar{\sigma}_0 = 1$  psf), and

$m$  = slope of the straight line.

The slopes of the straight lines for the NS and EW directions have values 0.22 and 0.23 while that for the TB direction has a value of 0.17. These values are slightly less than those reported by Hardin and Richart (1963). They concluded that P-wave velocity in sands varied as in Eq. 4.2 but with a slope of  $0.25 \pm 10$  percent within the range of 2000 psf to 8000 psf (96 to 383 kPa). The values of the constant  $C_1$  are very close to each other, namely 308, 280 and 371 for NS, EW and TB directions, respectively. (If the slope of the straight line for the TB direction were also 0.22, the value of the constant  $C_1$  back-calculated from P-wave velocity at 20 psi (138 kPa) would be 241 which looks more reasonable when compared to 308 and 280 for the horizontal directions for this cross-anisotropic specimen.) If P-wave velocity and isotro-

ic confining pressure are in units of m/s and kPa respectively, the values of the constant  $C_1$  would be 183, 172, and 190 for NS, EW and TB directions, respectively. (The value of  $C_1$  is 143 in the TB direction if a slope of 0.22 is assumed.)

With conditions of isotropic confinement, differences between velocities in the horizontal and vertical directions are due to structural anisotropy which is seen to be independent of confining pressure. Writing Eq. 4.2 for velocities in the horizontal and vertical directions separately and eliminating the confining pressure from the two equations, the relationship between horizontal and vertical velocities can be expressed as:

$$V_{pH} = 0.117(V_{vp})^{1.323} \quad (4.3)$$

It should be noted that the above equation is only valid for the sand sample used in the present series of tests since structural anisotropy can vary significantly with sample preparation (Mulilis et al, 1977).

#### 4.5 SUMMARY

From this study of P-wave velocity under isotropic confinement, the following conclusions can be drawn.

1. The effect of stress history on P-wave velocity is small and can be neglected for this sand.

2. Structural anisotropy affected the measured wave velocities, with velocities in the two horizontal directions about 17 per cent higher than the velocity in the vertical direction.

3. The relation between P-wave velocity and isotropic confining pressure agrees with that proposed by Hardin and Richart (1963) and can be expressed by Eq. 4.2. The general form of the equation was unaffected by structural anisotropy, which only affected the constants.

These conclusions are in general agreement with those reported by Kopperman et al (1982). For the purposes of comparison, results obtained in this series of tests and those reported by Kopperman et al (1982) are summarized in Table 4.2 and shown together in Fig. 4.3. The values of slopes obtained in the present series of tests are less than those reported by Kopperman et al (1982). However, the trend is the same in both cases as shown in Fig. 4.3, namely velocities in the horizontal directions are higher than velocities in the vertical direction, illustrating the effect of structural anisotropy. In the present series of tests, velocities in the horizontal directions (NS and EW) are almost the

TABLE 4.2

Comparison of Constants and Slopes for Equation 4.2\*  
with Those Reported by Kopperman et al (1982)

DIRECTION	$C_1$		$m$	
	PRESENT STUDY	KOPPERMAN et al	PRESENT STUDY	KOPPERMAN et al
NS	308	250	0.22	0.23
EW	280	210	0.23	0.24
TB	371	271	0.17	0.20

$$*V_p = C_1 \bar{\sigma}_o^m$$

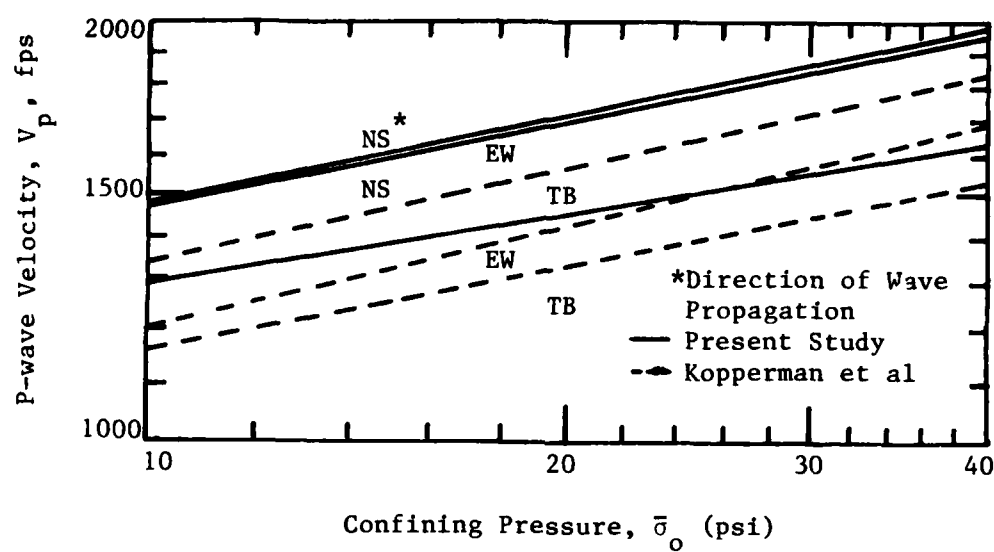


Fig. 4.3 - Comparison of P-wave Velocities with Results from Kopperman et al (1982)



same. This clearly shows the improvements of homogeneity in the lateral directions obtained by using the new rainer to construct the sample as discussed in Section 2.3.

## CHAPTER FIVE

## STRESS-STRAIN BEHAVIOR AND CROSS-ANISOTROPIC MODEL

## 5.1 INTRODUCTION

A study of an appropriate constitutive model for the sand specimen was performed in light of the stress-strain data provided by the stress cells and strain sensors which were installed in the sand specimen during construction. Since the sand specimen is inherently anisotropic (structural anisotropy), models other than that for a homogeneous, isotropic and linear elastic material, which requires two elastic constants (e.g. Young's modulus,  $E$ , and Poisson's ratio,  $\nu$ ), were examined. Based on the results of P-wave velocities under isotropic confinement (Section 4.3), the sand specimen can be idealized as a cross-anisotropic material (also known as transversely or hexagonally anisotropic). A cross-anisotropic material is one with a plane of symmetry in which all stress-strain relations are isotropic: i.e., the elastic constants are the same no matter how the axes are chosen within the given plane. However, the elastic constants for stresses and strains outside this plane are different. Due to the manner in which the sand was rained into the triaxial device (Section 3.3), the horizontal plane turned out to be the plane of symmetry. This is also true for many naturally deposited soils and sedimentary rocks.

The performances of stress cells and strain sensors are examined herein in relation to the cross-anisotropic model. The stress-strain data and wave velocities are then used to evaluate the constants for the cross-anisotropic model.

## 5.2 NOTATION FOR STRESSES, STRAINS AND WAVE VELOCITIES

Conventional notation used in mechanics is adopted here; that is, tension is considered positive. This convention is used because compressive strains obtained from readings of the strain sensors embedded in the sand specimen gave negative values. A schematic drawing of stresses acting in the positive sense is shown in Fig. 5.1. It should be noted that only stresses acting on the exposed faces of the element are shown while equal complementary stresses acting in opposite directions on the hidden faces are omitted for simplicity. The notation used for the stress is for the first subscript to denote the plane and the second subscript to denote the line of action. Therefore, normal stresses have same letters for the two subscripts while shear stresses have different letters.

Tensor notation is also used. Expressions for strains are listed in the following equations for easy reference:

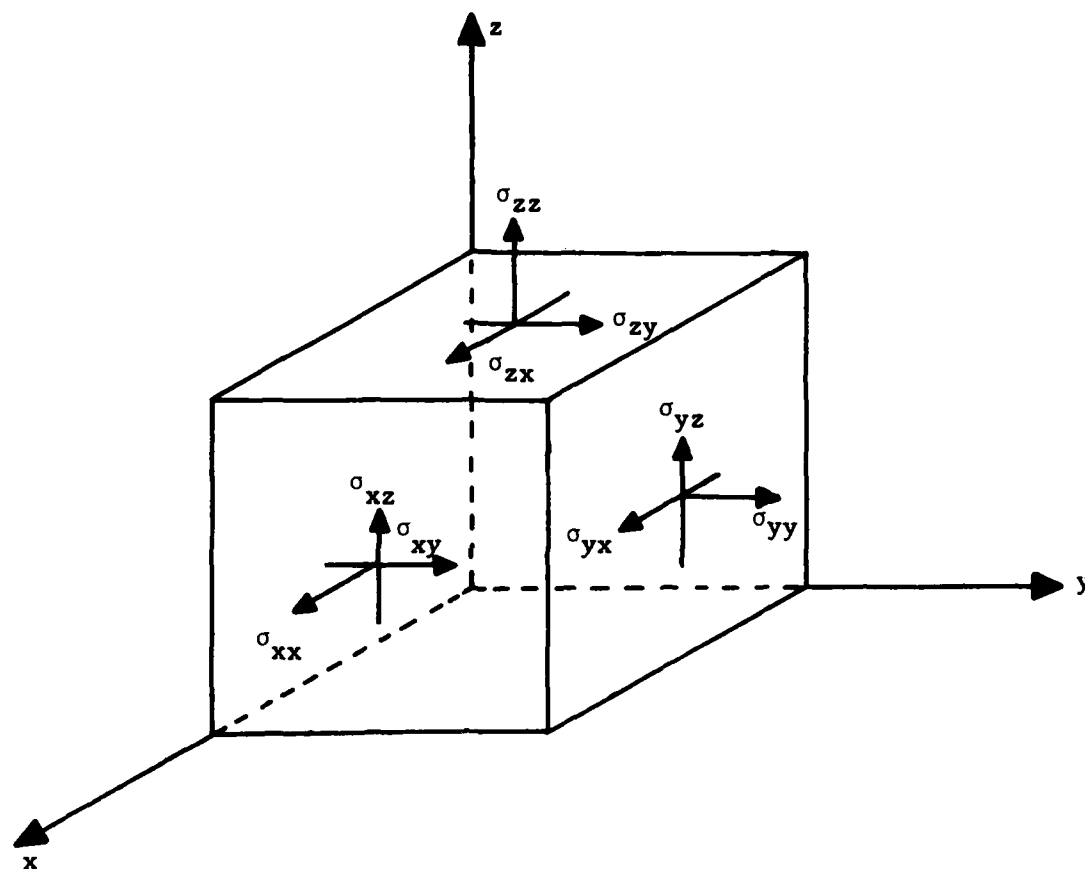


Fig. 5.1 - Orientation of Positive Stresses Acting on a Soil Element

$$\epsilon_{xx} = \frac{1}{2}(\partial u/\partial x + \partial u/\partial x) = \partial u/\partial x \quad (5.1)$$

$$\epsilon_{yy} = \frac{1}{2}(\partial v/\partial y + \partial v/\partial y) = \partial v/\partial y \quad (5.2)$$

$$\epsilon_{zz} = \frac{1}{2}(\partial w/\partial z + \partial w/\partial z) = \partial w/\partial z \quad (5.3)$$

$$\epsilon_{xy} = \epsilon_{yx} = \frac{1}{2}(\partial v/\partial x + \partial u/\partial y) \quad (5.4)$$

$$\epsilon_{yz} = \epsilon_{zy} = \frac{1}{2}(\partial w/\partial y + \partial v/\partial z) \quad (5.5)$$

$$\epsilon_{zx} = \epsilon_{xz} = \frac{1}{2}(\partial u/\partial z + \partial w/\partial x) \quad (5.6)$$

The letters  $u$ ,  $v$  and  $w$  represent displacements in the  $x$ -,  $y$ - and  $z$ -directions, respectively. It should be noted that shear strains represented by  $\epsilon_{xy}$ ,  $\epsilon_{yz}$  and  $\epsilon_{zx}$  (Eqs. 5.4, 5.5 and 5.6) are exactly one-half the values of the shear strains represented by  $\gamma_{xy}$ ,  $\gamma_{yz}$  and  $\gamma_{zx}$ , respectively.

For most numerical purposes, stresses and strains discussed above are written as vectors:

$$\{\sigma\}^T = [\sigma_{xx} \ \sigma_{yy} \ \sigma_{zz} \ \sigma_{xy} \ \sigma_{yz} \ \sigma_{zx}] \quad (5.7)$$

$$\{\epsilon\}^T = [\epsilon_{xx} \ \epsilon_{yy} \ \epsilon_{zz} \ \epsilon_{xy} \ \epsilon_{yz} \ \epsilon_{zx}] \quad (5.8)$$

The stress-strain (constitutive) laws relating the two are usually expressed in matrix form:

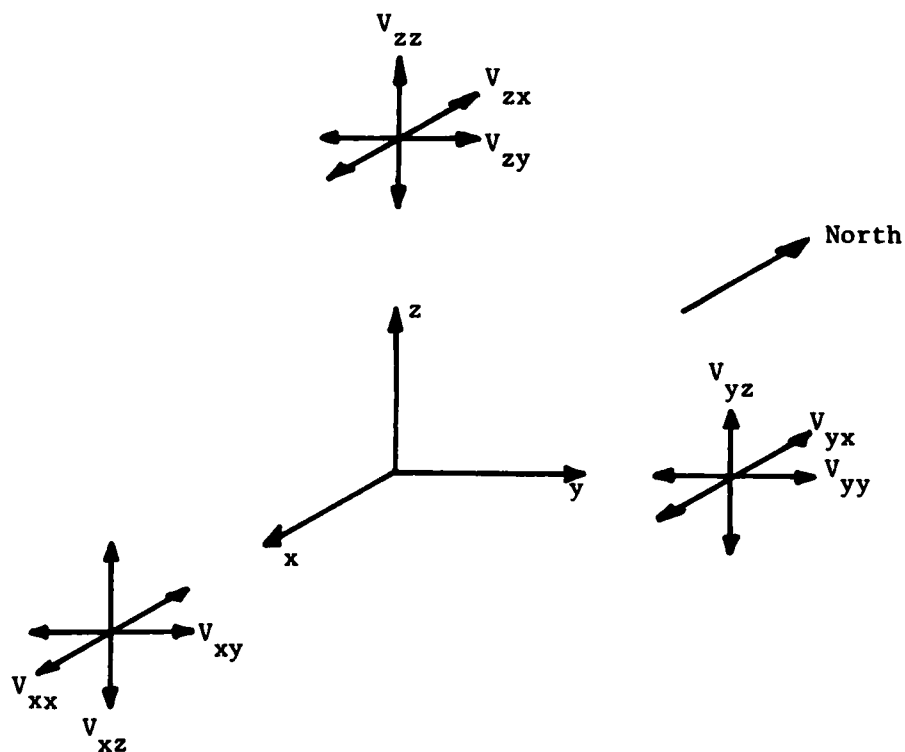
$$\{\sigma\} = [C] \{\epsilon\} \quad (5.9)$$

$$\{\epsilon\} = [D] \{\sigma\} \quad (5.10)$$

where  $[C]$  and  $[D]$  are  $6 \times 6$  matrices.

Velocities of three compression waves and six shear waves propagating and polarized along principal stress directions were measured in each test. These nine wave velocities are denoted by the symbols shown in Fig. 5.2. The notation of velocity used here is for the first subscript to denote the direction of wave propagation, while the second subscript denotes the direction of polarization (particle motion). Since the direction of propagation for P-waves is the same as the direction of particle motion, P-wave velocities have same letters for the subscripts. On the other hand, the direction of propagation for S-waves is different from the direction of particle motion; therefore, S-wave velocities have different letters for the first and second subscripts. It should be noted that the xy-plane is the horizontal plane which is the plane of symmetry in the cross-anisotropic model. The x-, y- and z- axes in Figs. 5.1 and 5.2 are the principal axes in the north-south (NS), east-west (EW) and vertical (TB) directions, respectively.

The above notation for stresses, strains and wave velocities are used in all subsequent analyses.



Legend: First letter denotes direction of wave propagation, second letter denotes direction of particle motion.

Compression Wave Velocities:  $V_{xx}$   
 $V_{yy}$   
 $V_{zz}$

Shear Wave Velocities:  $V_{xy}, V_{xz}$   
 $V_{yx}, V_{yz}$   
 $V_{zx}, V_{zy}$

Fig. 5.2 - Notation Used to Describe Wave Velocities

### 5.3 PERFORMANCE OF STRESS CELLS

Three total stress cells (Section 2.5.5) were used to monitor the stresses induced within the sand mass by the applied confining pressures. To investigate any effect of side shear along the walls of the triaxial device and hence to check the uniformity of stresses within the sand mass, two of the three stress cells (SS-1 and SS-2 in Fig. 3.1) were located such that they both measured stresses in the x-direction. The third stress cell (SS-3 in Fig. 3.1) was used to measure stress in the z-direction.

Since confining pressures applied by the air-water pressurizing system (Figs. 1.6 and 1.7) remained stable within acceptable limits ( $\pm 0.2$  psi ( $\pm 1.4$  kPa)), stresses indicated by the stress cells before the top membrane leaked were plotted against the applied confining stresses as shown in Figs. 5.3 to 5.5. Raw readings from the stress cells together with calibration curves shown in Figs. 2.15 to 2.17 were used to obtain stresses from the stress cells. As shown in Figs. 5.3 to 5.5, stresses indicated by the stress cells were widely scattered with all but four readings less than the applied pressure. The mean values and standard deviations were calculated for stresses obtained under the same confining stress. Linear regression was performed on the mean



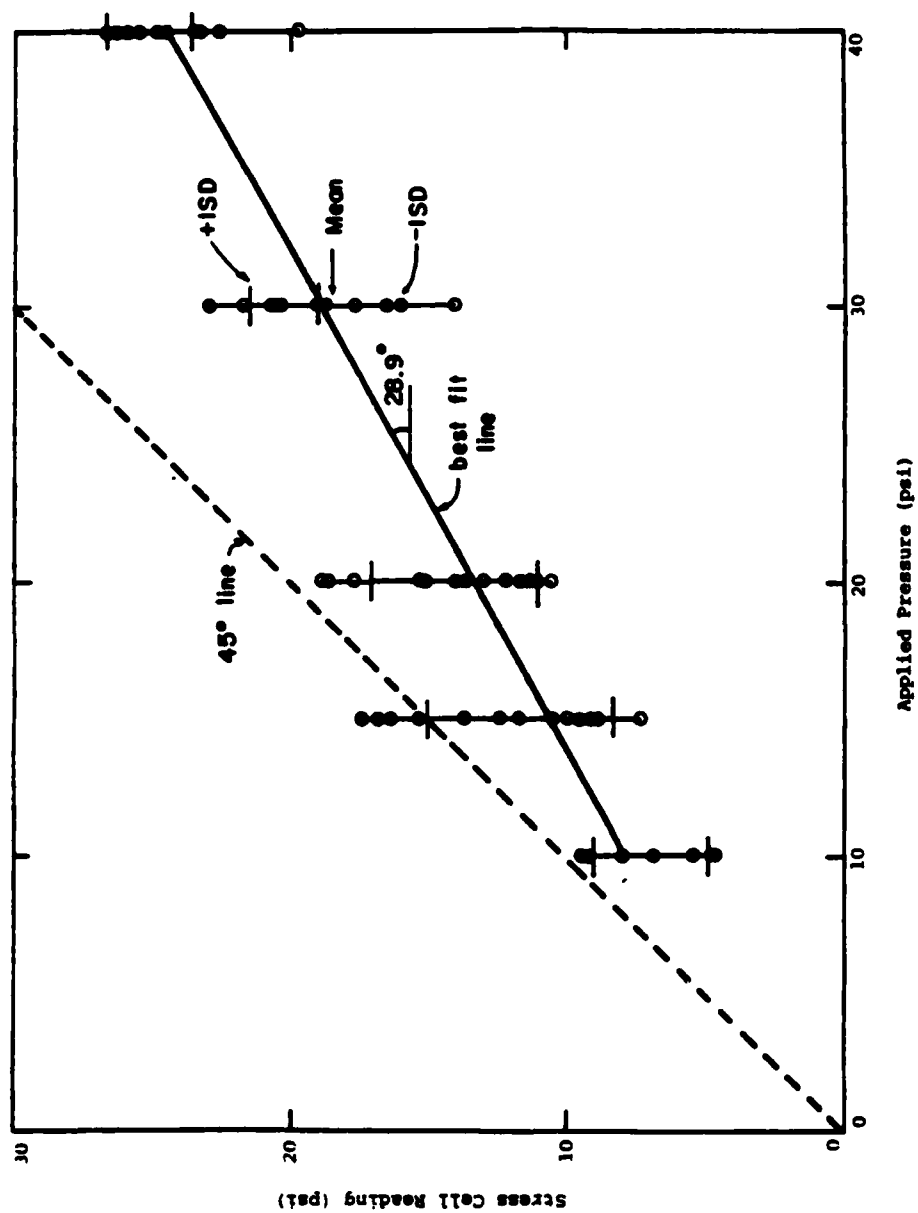


Fig. 5.3 - Comparison of Principal Stress Measured by Stress Cell SS-1 with Applied Stress in the Triaxial Device

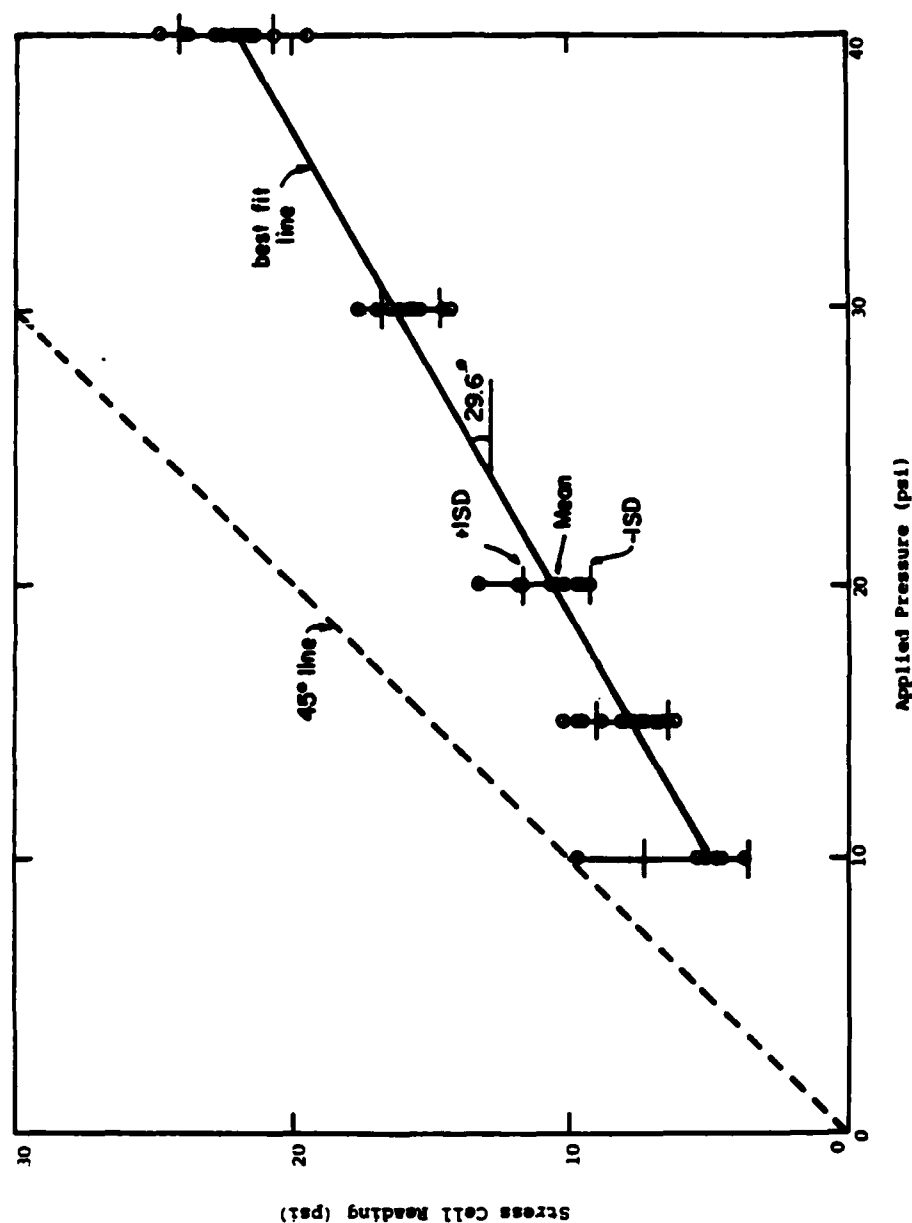


Fig. 5.4 - Comparison of Principal Stress Measured by Stress Cell SS-2 with Applied Stress in the Triaxial Device

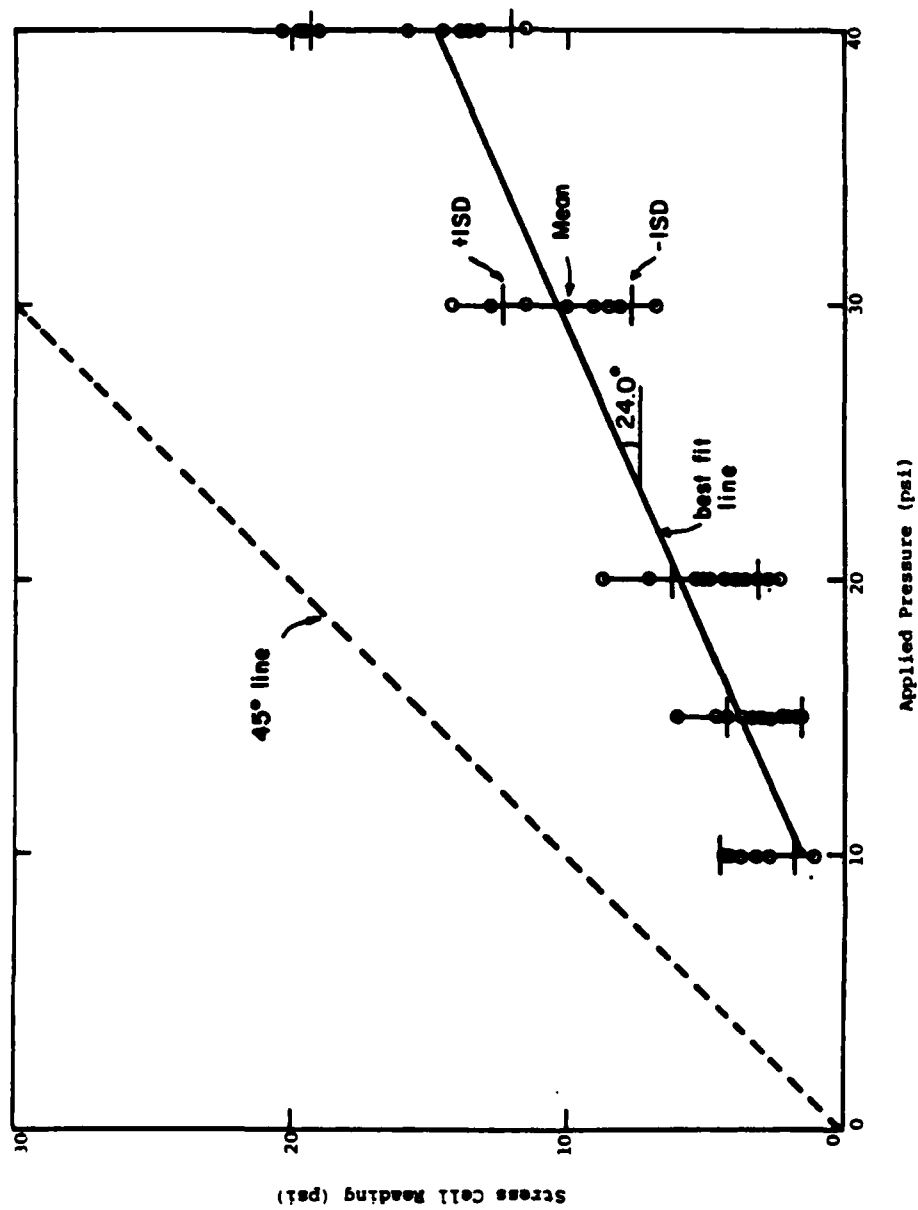


Fig. 5.5 - Comparison of Principal Stress Measured by Stress Cell SS-3 with Applied Stress in the Triaxial Device

values and the resulting best-fit straight lines are shown in Figs. 5.3 and 5.5.

As can be seen in the figures, readings from stress cell SS-2 are less scattered than readings from the other two stress cells. This is reasonable since cell SS-2 is closer to the pressurizing membrane than the other two stress cells and hence less influenced by any side shear along the walls of the triaxial device. However, stresses obtained from cell SS-1 are larger than stresses obtained from stress cell SS-2. This is not expected since side shear would reduce the transmitted normal stresses, and cell SS-1 is located farther away from the pressurizing membrane than cell SS-2.

Since stresses obtained from the stress cells were so scattered, it was concluded that further effort in analyzing the stress data was unworthy. Stress readings from the pressure gauge in the pressurizing system were, hence, taken to be representative of stresses in the sand specimen and were used in all subsequent analyses involving stresses.

#### 5.4 PERFORMANCE OF STRAIN SENSORS

Eight pairs of strain sensors (Section 2.5.6) were installed in the sand specimen in an attempt to measure strains induced by the applied confining pressures. The locations of the strain sensors are shown in Figs. 2.11 and 3.1. Readings of null amplitude from the control unit (Section 2.5.6) for each pair of strain sensors were recorded in each test. These amplitudes together with the calibration curves shown in Fig. 2.18 and Appendix A were used to estimate strains. However, strains measured by strain sensors SN-1, SN-2 and SN-4 (Fig. 3.1) were not used in the analyses for stress-strain behavior since they did not measure strains in the principal directions.

It was soon found in the isotropic series of tests that the strain sensors were not sensitive enough to measure strains accurately since: 1. null amplitudes changed very slightly or even remained unchanged under increasing or decreasing stress, and 2. for some cases, amplitude readings indicated tensile strains under increasing isotropic confining stress. These are shown in Fig. 5.6. Therefore, amplitude readings for strains were not measured in most of the tests under biaxial confinement before the top membrane leaked. However, amplitude readings were again measured after a new top membrane was installed hoping that some useful strain data might be obtained. Strain readings

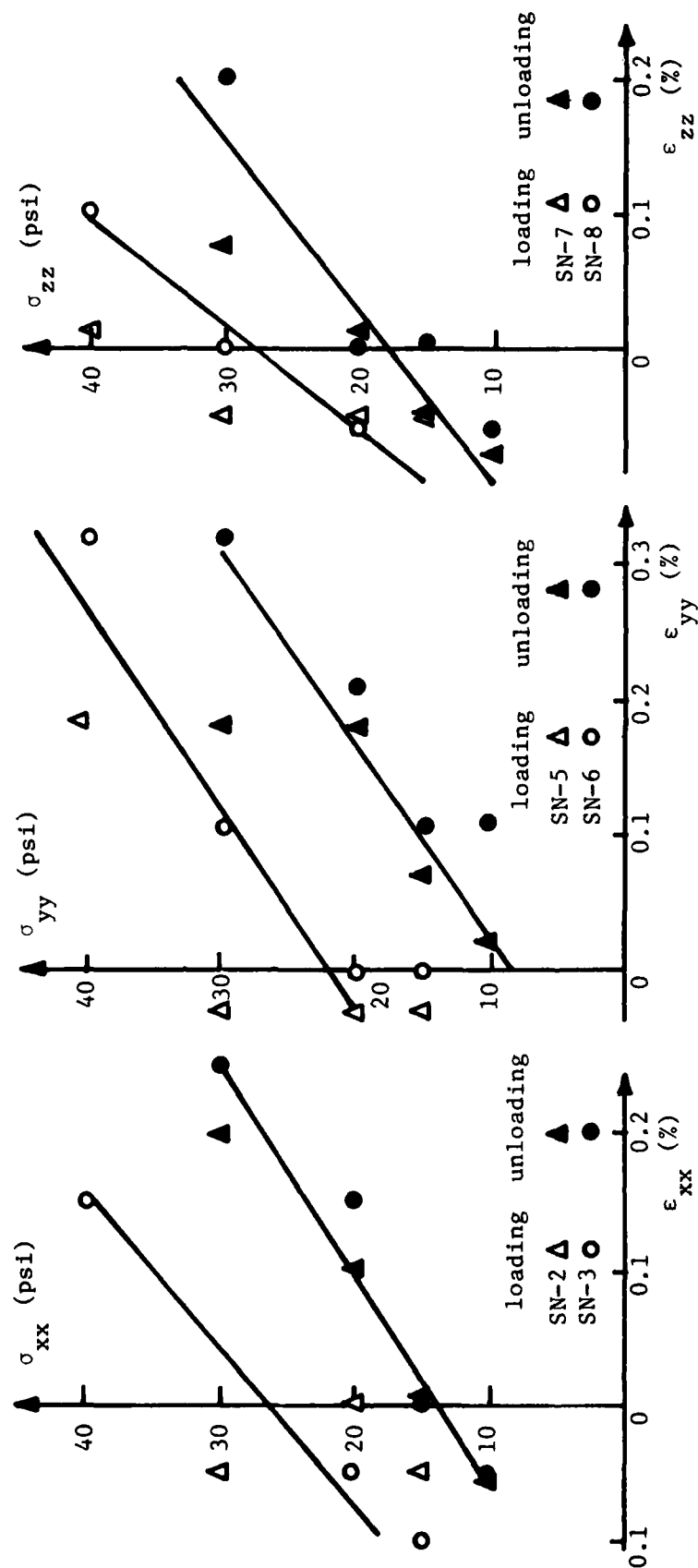


Fig. 5.6 - Stress-Strain Behavior Along Each Principal Direction Under Isotropic Confinement

were used to calculate Poisson's ratios  $\nu_{HV}$  and  $\nu_{VH}$  where the subscripts H and V denote the horizontal and vertical directions, respectively. The relation between horizontal strains and vertical loadings or between vertical strains and horizontal loadings is controlled by  $\nu_{HV}$  or  $\nu_{VH}$ . However, it should be noted that strain data were analyzed with biased judgement since less than a quarter of the data was used in analyses. Therefore, calculations using strain data only gave rough approximations of the constants.

### 5.5 CROSS-ANISOTROPY

The constitutive model for the sand specimen can be expressed by Eq. 5.9 or 5.10. Due to cross-anisotropy, there are only five independent constants to be evaluated in the stress-strain matrix  $[C]$  of Eq. 5.9 or strain-stress matrix  $[D]$  of Eq. 5.10 :

$$[C] = \begin{bmatrix} C_{11} & C_{12} & C_{13} & 0 & 0 & 0 \\ C_{12} & C_{11} & C_{13} & 0 & 0 & 0 \\ C_{13} & C_{13} & C_{33} & 0 & 0 & 0 \\ 0 & 0 & 0 & C_{11}-C_{12} & 0 & 0 \\ 0 & 0 & 0 & 0 & C_{55} & 0 \\ 0 & 0 & 0 & 0 & 0 & C_{55} \end{bmatrix} \quad (5.11)$$

$$[D] = \begin{bmatrix} D_{11} & D_{12} & D_{13} & 0 & 0 & 0 \\ D_{12} & D_{11} & D_{13} & 0 & 0 & 0 \\ D_{13} & D_{13} & D_{33} & 0 & 0 & 0 \\ 0 & 0 & 0 & D_{11}-D_{12} & 0 & 0 \\ 0 & 0 & 0 & 0 & D_{55} & 0 \\ 0 & 0 & 0 & 0 & 0 & D_{55} \end{bmatrix} \quad (5.12)$$

Shear wave velocities, in addition to normal stress-strain data, had to be used to evaluate the five independent constants in the matrix  $[D]$  since shear stresses and strains were not measured. Once the terms in matrix  $[D]$  were evaluated, matrix  $[C]$  could be obtained by inverting matrix  $[D]$ . On the other hand, the nine wave velocities (Section 5.2) measured along principal directions could be used to evaluate four of the five constants in matrix  $[C]$  and to estimate the fifth constant. These two approaches are discussed in the following sections.



### 5.5.1 Evaluation of Constants by Stress-Strain Data and Wave Velocities

For the cross-anisotropic model with the xy-plane (horizontal plane) as the plane of symmetry, the terms in the strain-stress matrix  $[D]$  in Eq. 5.12 as suggested by Desai and Christian (1977) are:

$$\begin{aligned}
 D_{11} &= D_{22} = \frac{1}{E_H} \\
 D_{33} &= \frac{1}{E_V} \\
 D_{44} &= \frac{1+\nu_{HH}}{E_H} \\
 D_{55} &= D_{66} = \frac{1}{2G_{VH}} \\
 D_{12} &= D_{21} = -\frac{\nu_{HH}}{E_H} \\
 D_{13} &= D_{31} = D_{23} = D_{32} = -\frac{\nu_{VH}}{E_H} = -\frac{\nu_{HV}}{E_V}
 \end{aligned} \tag{5.13}$$

The symbols  $E_H$  and  $E_V$  represent Young's moduli in the horizontal plane and vertical direction, respectively. Poisson's ratio relating the strains in one horizontal axis to strains in the other horizontal axis is  $\nu_{HH}$  while  $\nu_{VH}$  and  $\nu_{HV}$  are defined previously in Section 5.4 and are not independent of each other because of symmetry in the  $[D]$  matrix. The  $G_{VH}$  term relates shear stresses out of the horizontal plane to shear strains out of the horizontal plane.

Using the terms in Eq. 5.13 for the  $[D]$  matrix and expanding the matrices in Eq. 5.10 for normal strains gives:

$$\epsilon_{xx} = \frac{1}{E_H} \sigma_{xx} - \frac{\nu_{HH}}{E_H} \sigma_{yy} - \frac{\nu_{HV}}{E_V} \sigma_{zz} \quad (5.14)$$

$$\epsilon_{yy} = -\frac{\nu_{HH}}{E_H} \sigma_{xx} + \frac{1}{E_H} \sigma_{yy} - \frac{\nu_{HV}}{E_V} \sigma_{zz} \quad (5.15)$$

$$\epsilon_{zz} = -\frac{\nu_{VH}}{E_H} \sigma_{xx} - \frac{\nu_{VH}}{E_H} \sigma_{yy} + \frac{1}{E_V} \sigma_{zz} \quad (5.16)$$

It should be noted that for biaxial confinements with same horizontal stresses, Eq. 5.14 is the same as Eq. 5.15 and strains in the x-direction should be equal to the strains in the y-direction. However, strain readings from the strain sensors gave values that were far off from each other, up to an order of magnitude different showing the poor quality of strain data. Some usable strain data under appropriate biaxial conditions gave average values of 0.35 and 0.17 for  $\nu_{HV}$  and  $\nu_{VH}$  respectively. However, it should be emphasized again that these were only rough estimations for the parameters since the strain data were not satisfactory as discussed in Section 5.4. The value of Poisson's ratio  $\nu_{HH}$  was calculated using the following equation:

$$\nu_{HH} = \frac{V_{xy}^2 - 0.5 V_{xx}^2}{V_{xy}^2 - V_{xx}^2} = \frac{V_{yx}^2 - 0.5 V_{yy}^2}{V_{yx}^2 - V_{yy}^2} \quad (5.17)$$

With data of S-wave velocities (Lee et al, 1984) and P-wave velocities for waves propagating along horizontal axes under isotropic confinement, the average value of  $\nu_{HH}$  was found to be 0.27. With known values for the Poisson's ratios, Eqs. 5.14 to 5.16 were solved for  $E_H$  and  $E_V$  using the available stress-strain data. Due to the poor quality of the data, values of  $E_H$  ranged from 9,300 psi (64 MPa) to 70,400 psi (485 MPa) with an average of 21,100 psi (145 MPa) while values of  $E_V$  ranged from 7,700 psi (53 MPa) to 9,200 psi (63 MPa) with an average of 8,300 psi (57 MPa). Shear wave velocities provided from Lee et al (1984)

together with equation suggested by Bachman (1983) were used to evaluate the last parameter  $G_{VH}$ . The equation used was:

$$G_{VH} = [\Sigma(\rho V_{zx}^2) + \Sigma(\rho V_{zy}^2) + \Sigma(\rho V_{yz}^2) + \Sigma(\rho V_{xz}^2)]/n \quad (5.18)$$

where  $n$  is the number of measurements and  $\rho$  is the mass density of the sample. The average value of  $G_{VH}$  calculated from shear wave velocities under isotropic confinements at 20 psi (138 kPa) was 17,700 psi (122 MPa).

As suggested by Desai and Christian (1977), the terms in the cross-anisotropic  $[C]$  matrix found by inverting the  $[D]$  matrix are:

$$\begin{aligned} C_{11} &= C_{22} = A\left(\frac{E_H}{E_V} - \nu_{VH}^2\right) = M_H \\ C_{33} &= A(1 - \nu_{HH}^2) = M_V \\ C_{44} &= \frac{E_H}{1 + \nu_{HH}} = 2G_{HH} \\ C_{55} &= C_{66} = 2G_{VH} \\ C_{12} &= C_{21} = A\left(\frac{E_H}{E_V} \nu_{HH} + \nu_{VH}^2\right) = C_{11} - C_{44} \\ C_{13} &= C_{31} = C_{23} = C_{32} = A\nu_{VH}(1 + \nu_{HH}) \\ A &= \frac{E_H}{(1 + \nu_{HH})[(E_H/E_V)(1 - \nu_{HH}) - 2\nu_{VH}^2]} \end{aligned} \quad (5.19)$$

Since the values of the parameters in the [D] matrix were already calculated, the terms in the [C] matrix had the following values:

$$C_{11} = 23200 \text{ psi (160 MPa)}$$

$$C_{33} = 8600 \text{ psi ( 59 MPa)}$$

$$C_{44} = 16600 \text{ psi (114 MPa)}$$

$$C_{55} = 35400 \text{ psi (244 MPa)}$$

$$C_{12} = 6600 \text{ psi ( 45 MPa)}$$

$$C_{13} = 2000 \text{ psi ( 14 MPa)}$$

It should be noted that the ratio of  $M_H$  to  $M_V$  (2.70) is too large when compared to the square of the ratio of P-wave velocity in the horizontal direction to P-wave velocity in the vertical direction, the value of which as approximated by Eq. 4.1 is 1.37.

#### 5.5.2 Estimation of Constants by Wave Velocities

With measurements of the nine wave velocities under isotropic confinement, four of the five independent parameters in the [C] matrix can be evaluated. The equations suggested by Bachman (1983) to evaluate these parameters are:

$$\begin{aligned}
C_{11} &= C_{22} = M_H = [\Sigma(\rho V_{xx}^2) + \Sigma(\rho V_{yy}^2)]/n \\
C_{33} &= M_V = \Sigma(\rho V_{zz}^2)/n \\
C_{44} &= 2G_{HH} = 2[\Sigma(\rho V_{xy}^2) + \Sigma(\rho V_{yx}^2)]/n \\
C_{55} &= C_{66} = 2G_{VH} = 2[\Sigma(\rho V_{zx}^2) + \Sigma(\rho V_{zy}^2) + \Sigma(\rho V_{yz}^2) + \Sigma(\rho V_{xz}^2)]/n
\end{aligned} \tag{5.20}$$

The expressions for the remaining terms in the  $[C]$  matrix suggested by Drnevich (1975) are:

$$C_{12} = C_{21} = M_H - 2G_{HH} \tag{5.21}$$

$$C_{13} = C_{23} = C_{32} = C_{31} = \frac{1}{2}(M_H + M_V) - 2G_{VH} \tag{5.22}$$

It should be noted that Eq. 5.22 is only an approximation since measurement of P-wave velocities propagating at an angle to the principal axis is needed to evaluate the fifth constant. Equation for calculating the fifth constant from oblique P-waves as presented by Podio (1968) is:

$$C_{13} = \{[2\rho V_{45}^2 - \frac{1}{2}(C_{11} + C_{33} + 2C_{44})]^2 - [\frac{C_{11} - C_{33}}{2}]^2\}^{\frac{1}{2}} - C_{44} \tag{5.23}$$

where  $V_{45}$  is the velocity of P-wave propagating at 45 degrees to the principal directions.

With S-wave velocities (Lee et al , 1984) and P-wave velocities (Table 4.1) under isotropic confinement of 20 psi (138 kPa), the expressions in Eq. 5.20 are found to have the following values:

$$C_{11} = 64100 \text{ psi (442 MPa)}$$

$$C_{33} = 48000 \text{ psi (331 MPa)}$$

$$C_{44} = 46500 \text{ psi (320 MPa)}$$

$$C_{55} = 35400 \text{ psi (244 MPa)}$$

From the above results, the remaining terms in the  $[C]$  matrix calculated by Eqs. 5.21 and 5.22 are:

$$C_{12} = 17700 \text{ psi (122 MPa)}$$

$$C_{13} = 20700 \text{ psi (143 MPa)}$$

When compared to values of the same terms determined in Section 5.5.1, the above terms are larger. The largest difference occurred in the term  $C_{13}$  with a value about 10 times larger.

## 5.6 SUMMARY

The stress-strain behavior of the sand specimen is studied. To help in this study, notation for stresses, strains and wave velocities are first defined in Section 5.2. The performance of stress cells and strain sensors are then evaluated. Unfortunately, both stress

cells and strain sensors are found to have provided data which were highly scattered and generally unsatisfactory.

The cross-anisotropic model for the sand specimen is studied analytically in Section 5.5. With available readings of stresses, strains and wave velocities, complete evaluation of all constants in the cross-anisotropic matrix  $[C]$  relating stress and strain can be accomplished. However, it should be noted that data of stresses, strains and wave velocities were obtained from different stress states. It was also found that a consistent set of wave velocity (both P-wave and S-wave) data could be used to evaluate four of the five independent constants in the  $[C]$  matrix and to approximate the fifth. If oblique P-waves were monitored and velocities were measured in the present series of tests, the fifth constant could have been evaluated by these velocities.



## CHAPTER SIX

### BIAXIAL CONFINEMENT

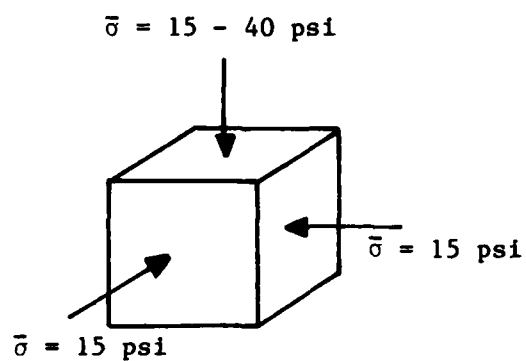
#### 6.1 INTRODUCTION

After studying the effect of isotropic confinement on P-wave velocity, an exhaustive set of tests with biaxial confinement was performed. Conditions of biaxial confinement were obtained by keeping the intermediate principal effective stress equal to the minor principal effective stress ( $\bar{\sigma}_1 > \bar{\sigma}_2 = \bar{\sigma}_3$ ) or by keeping the intermediate principal effective stress equal to the major principal effective stress ( $\bar{\sigma}_1 = \bar{\sigma}_2 > \bar{\sigma}_3$ ).

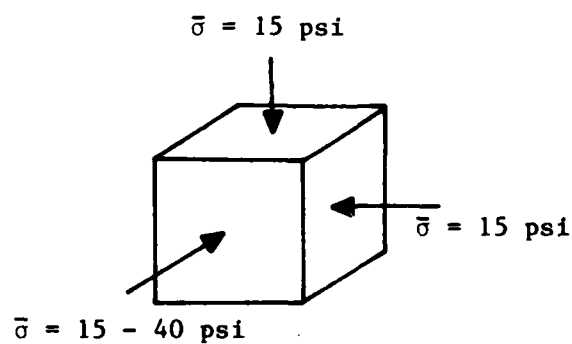
The complete set of tests was composed of two series of biaxial confinement tests: the first series consisted of tests with confining stress varying in only one principal direction while the second series consisted of tests with confining stress varying in two principal directions. Additionally, the first series of tests contained two subsets: the first subset was composed of tests with the intermediate principal stress always equal to the minor principal stress while the second subset was composed of tests where the intermediate principal stress ranged in value from the minor to the major principal stress. The loading conditions for this first series of tests are shown in

Figs. 6.1 and 6.2 for subsets one and two, respectively. The loading conditions for the second test series are shown in Fig. 6.3. Tests of unloading sequences for the conditions shown in Figs. 6.1 to 6.3 were also performed so that complete data were available for the study of stress history and possible structural anisotropy effects.

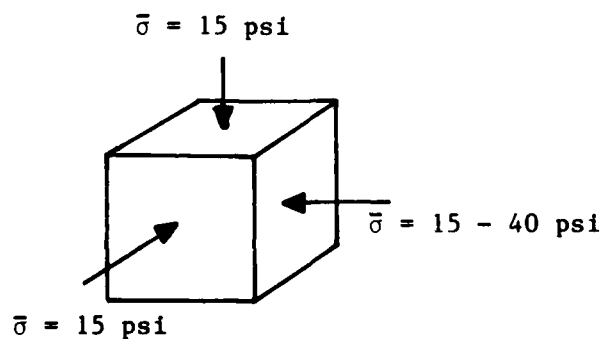
Tests with biaxial confinement started with an isotropic state of stress of 15 psi (103 kPa). The stress in the vertical direction (z-direction) was then increased from 15 psi (103 kPa) to 20, 30 and 40 psi (138, 207 and 276 kPa) as shown in Fig. 6.1(a). With the stress of 40 psi (276 kPa) being held constant in the z-direction, stresses in the x- and y- directions were then increased from 15 to 40 psi (103 to 276 kPa) in the same increments as before. This loading condition is shown in Fig. 6.3(a). Then the horizontal stresses were unloaded from 40 psi (276 kPa) to 15 psi (103 kPa) in the reverse sequence with the vertical stress staying constant at 40 psi (276 kPa). With the horizontal stresses being held constant at 15 psi (103 kPa), the vertical stress was unloaded from 40 psi (276 kPa) to 15 psi (103 kPa) in the same reverse sequence. This represented major principal stress in the z-direction. Then, complete series of tests was redone with  $\bar{\sigma}_1$  in the x-direction. The loading conditions are shown in Figs. 6.1(b) and 6.3(b). Then, complete series of tests was redone with  $\bar{\sigma}_1$  in



(a) First Orientation of Principal Stresses

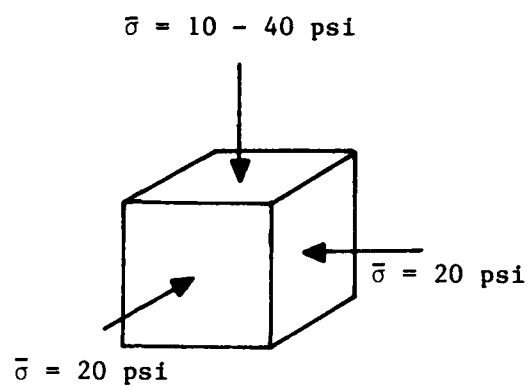


(b) Second Orientation of Principal Stresses

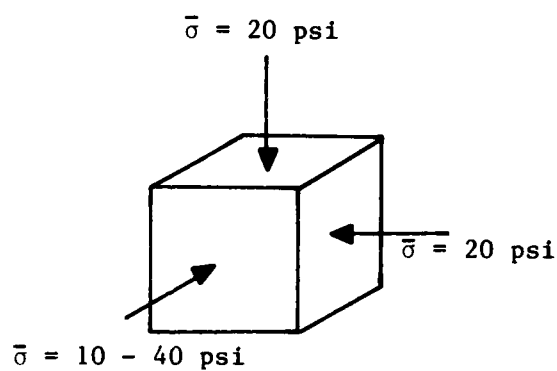


(c) Third Orientation of Principal Stresses

Fig. 6.1 - Initial Subset of First Series of  
Biaxial Confinement Tests with  
Variation of Stress in One Principal  
Direction

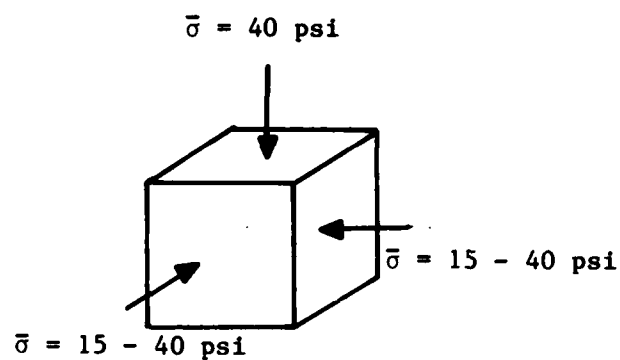


(a) First Orientation of Principal Stresses

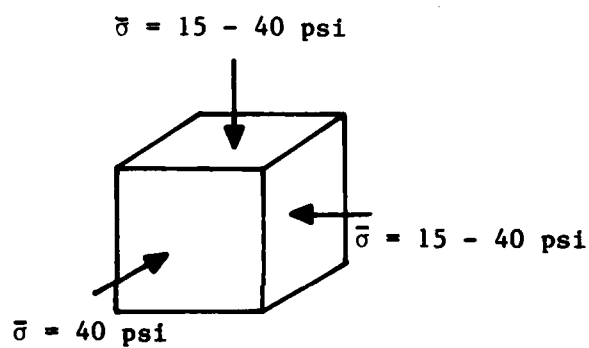


(b) Second Orientation of Principal Stresses

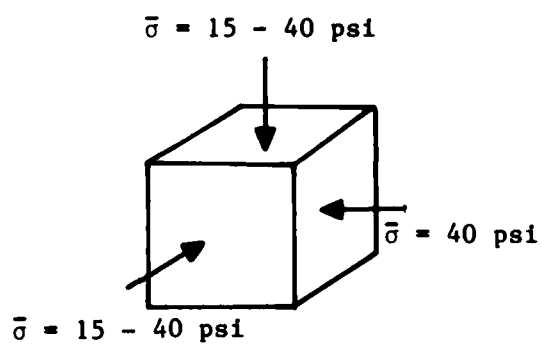
Fig. 6.2 - Second Subset of First Series of  
 Biaxial Confinement Tests with  
 Variation of Stress in One Principal  
 Direction



(a) First Orientation of Principal Stresses



(b) Second Orientation of Principal Stresses



(c) Third Orientation of Principal Stresses

Fig. 6.3 - Second Series of Biaxial Confinement Tests with Variations of Stresses in Two Principal Directions

the y-direction with loading conditions shown in Figs. 6.1(c) and 6.3(c).

In addition to the tests described above, tests with loading conditions shown in Fig. 6.2 were performed to study the effect of intermediate principal effective stress on P-wave velocity. As shown in Fig. 6.2(a), stress in the z-direction ranged in value from the minor to the major principal stress while stresses in the x- and y-directions remained constant at 20 psi (138 kPa) which represented the intermediate principal stress. It should be noted that the intermediate principal stress was also the major principal stress when the stress in the z-direction was the minor principal stress, and vice versa. Then, complete series of tests was redone with stress variation in the x-direction as shown in Fig. 6.2(b). Tests with stress variation in the y-direction are not performed since the sample is believed to be cross-anisotropic (Section 5.1) and enough data were believed to have been obtained for studying the effect of intermediate principal stress on P-wave velocities.

The exact sequences of the complete series of tests with biaxial confinement are summarized in Table 3.2 and shown schematically in Figs. 3.6 and 3.7.

## 6.2 VARIATION OF STRESS IN ONE PRINCIPAL DIRECTION

Compression wave velocities were measured along each principal stress axis under each biaxial state. The same procedure discussed in Section 3.5 was used to analyze all data. The biaxial conditions shown in Figs. 6.1 and 6.2 are referred to as the first series of tests with variation of stress in one principal direction. Results from the first subset of these tests (Fig. 6.1) were used to study the effects of stress history, structural anisotropy and biaxial confinement on P-wave velocities. Results from the second subset of the first test series (Fig. 6.2) were used to study the effect of intermediate principal effective stress on P-wave velocities.

### 6.2.1 Effect of Stress History

Compression wave velocities obtained under the same loading and unloading conditions for each biaxial state of stress were used to study the effect of stress history on P-wave velocities. One complication was that the unloading conditions were performed sometime after each of the corresponding loading conditions shown in Fig. 6.1. This time delay was, however, assumed inconsequential.

Compression wave velocities propagating along the axis of increasing stress are plotted against the corresponding stress in Fig. 6.4 for both loading and unloading conditions. The notation for velocities discussed in Section 5.2 is used. The notation for stresses used by Kopperman et al (1982) is also used in which:

$\bar{\sigma}_a$  = effective stress in the direction of wave propagation,

$\bar{\sigma}_b$  = effective stress in the direction of particle motion, and

$\bar{\sigma}_c$  = effective stress perpendicular to  $\bar{\sigma}_a$  and  $\bar{\sigma}_b$

For P-waves,  $\bar{\sigma}_a$  and  $\bar{\sigma}_b$  are in the same direction. (For shear waves,  $\bar{\sigma}_a$  and  $\bar{\sigma}_b$  are perpendicular.)

As shown in Fig. 6.4, P-wave velocities in the unloading condition are slightly higher than those in the loading condition. The differences are small with the largest discrepancy of about 8 percent occurring at 20 psi (138 kPa) in the y-direction. The mean value of the percentage differences for the rest of the data in all three directions is 2 percent. Hence, the effect of stress history is negligible. As a result, average values of the data from loading and unloading are used for all subsequent analyses.



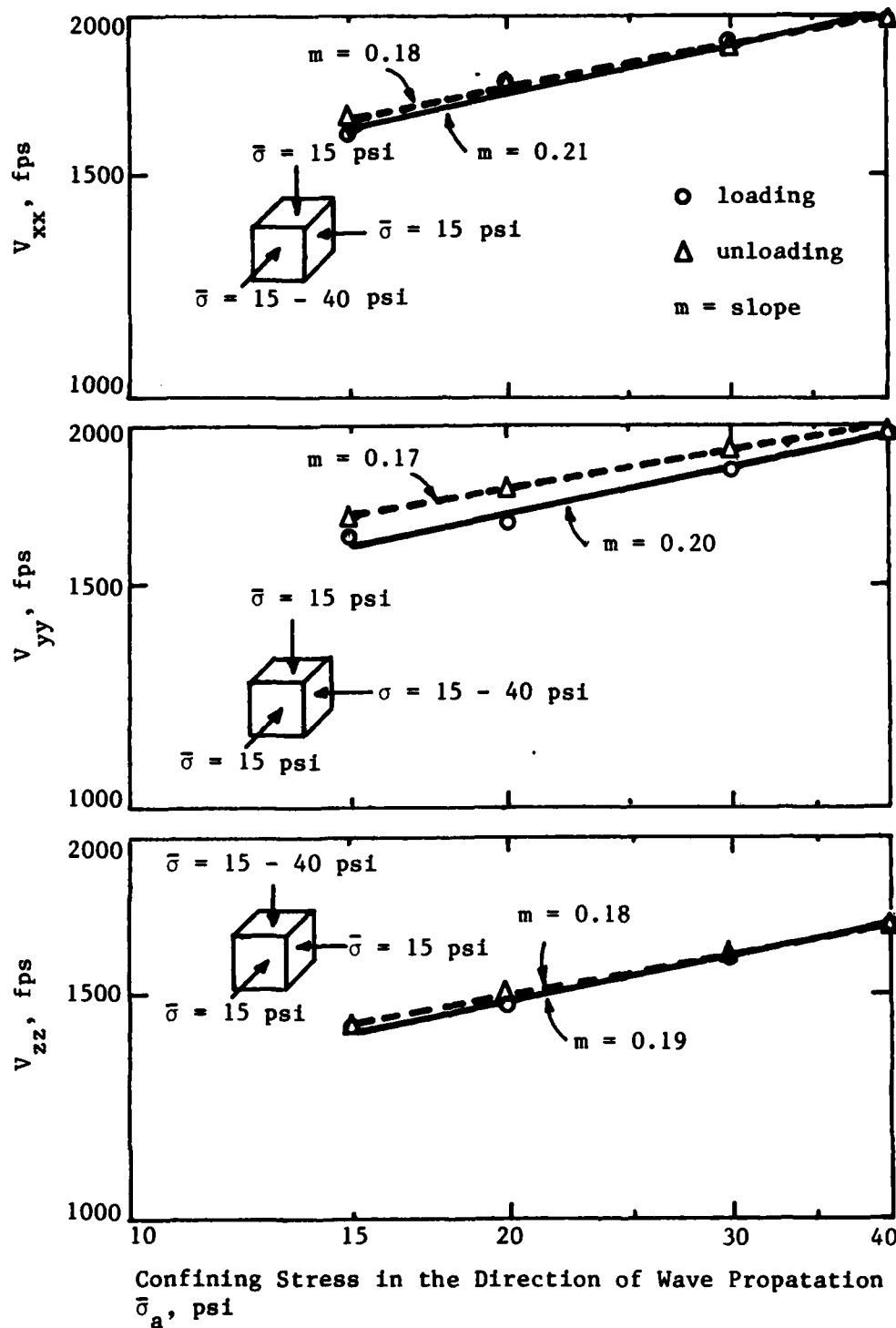


Fig. 6.4 - Effect of Stress History on P-wave Velocity Under Biaxial Confinement with Variation of Stress in One Direction

### 6.2.2 Effect of Structural Anisotropy

If the sand specimen was perfectly uniform and isotropic, P-wave velocities shown in Fig. 6.4 along the axis of increasing stress would have been the same for each of the three different orientations of the major principal stress. Best-fit straight lines for the average values of the loading and unloading data for each of these three biaxial conditions are shown together in Fig. 6.5. The three straight lines show exactly the same trend as those for isotropic conditions (Fig. 4.2). Therefore, the effect of structural anisotropy is independent of these stress states and has the same effect on P-wave velocities for both isotropic and biaxial conditions.

As shown in Fig. 6.5, the cross-anisotropic model for the sand specimen is again confirmed since P-wave velocities in the horizontal directions (NS and EW) are almost the same, with a maximum percentage difference of less than 4 percent. Due to cross anisotropy, velocities in the horizontal directions are about 17 percent higher than the velocity in the vertical direction for the same state of stress.

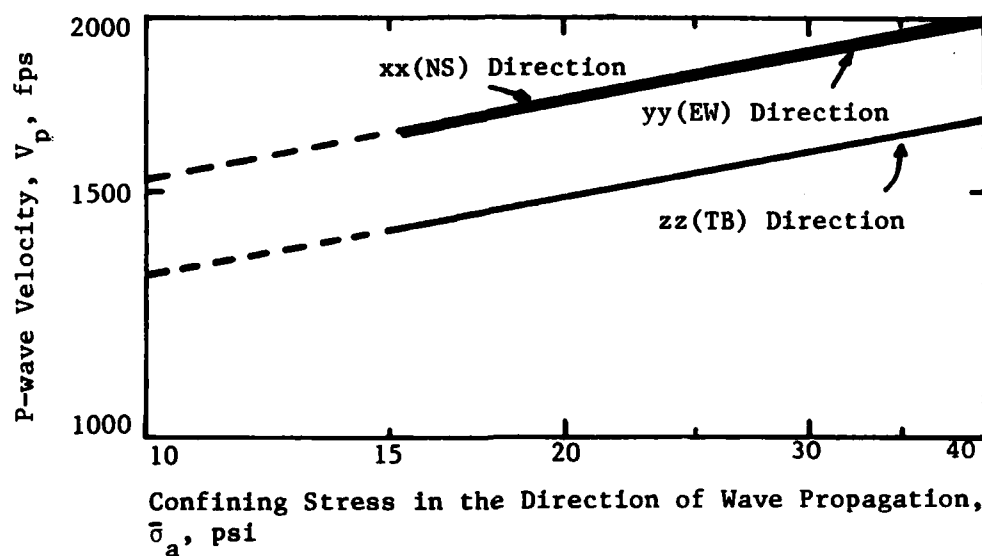


Fig. 6.5 - Effect of Structural Anisotropy on P-wave Velocities Under Biaxial Confinement with Variation of Stress in One Direction

### 6.2.3 Effect of Biaxial Confinement

To study the effect of biaxial confinement on  $V_p$ , velocities of waves propagating along each principal axis for conditions shown in Fig. 6.1 are plotted against the increasing confining stress in Figs. 6.6, 6.7 and 6.8 respectively. Compression wave velocities under isotropic conditions are also shown in the figures for comparison purposes.

As shown in Figs. 6.6(a), 6.7(a) and 6.8(a), compression wave velocity in the direction of increasing confining stress under biaxial confinement varies with stress in essentially the same manner as under isotropic confinement. These results suggest that the relationship between wave velocity and confining stress for biaxial confinement can be patterned after Eq. 4.2 for isotropic confinement if  $\bar{\sigma}_a$  (stress in the direction of wave propagation in psf) is substituted for  $\bar{\sigma}_o$  (isotropic confining stress in psf). The resulting equation is:

$$V_p = C_1 \bar{\sigma}_a^m \quad (6.1)$$

Values of constants in Eq. 6.1 were obtained by fitting a power curve to each set of data using least-squares method (Figs. 6.6a, 6.7a and 6.8a). These values along with those determined for isotropic confinement are summarized in Table 6.1. Most importantly, since the

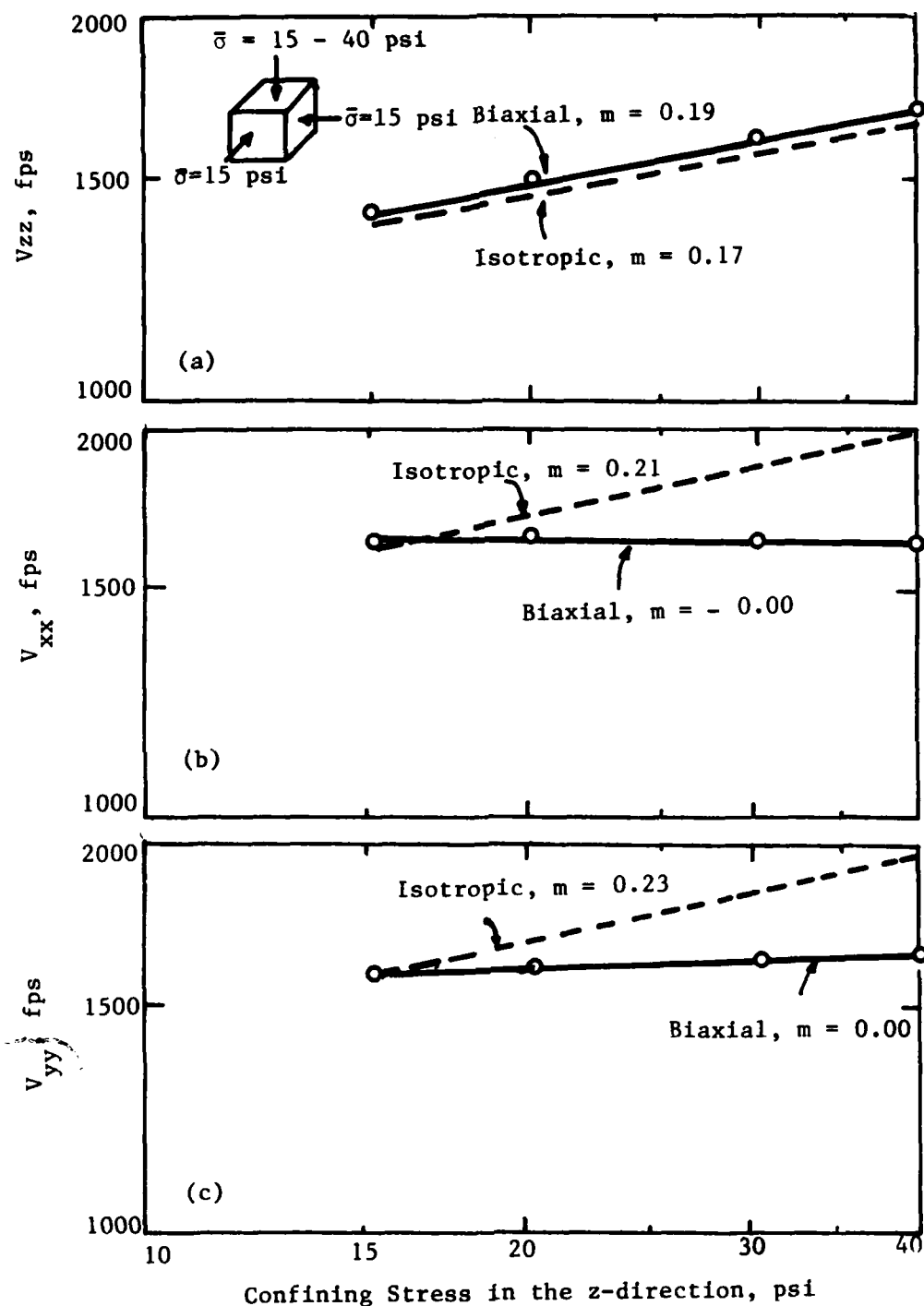


Fig. 6.6 - Variation in P-wave Velocities Under Biaxial Conditions for Stress Increasing Along z-direction

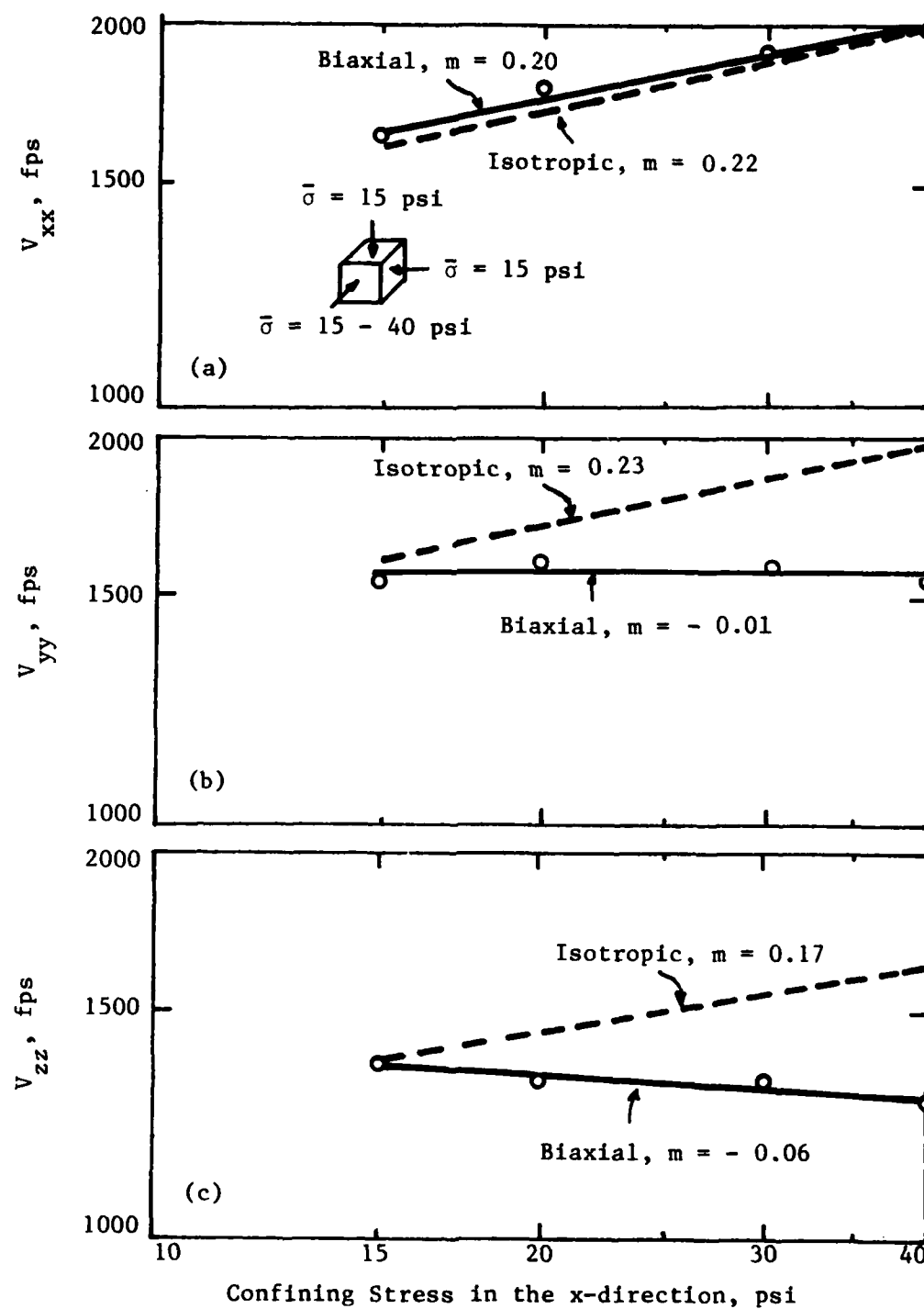


Fig. 6.7 - Variation in P-wave Velocities Under Biaxial Conditions for Stress Increasing Along x-direction

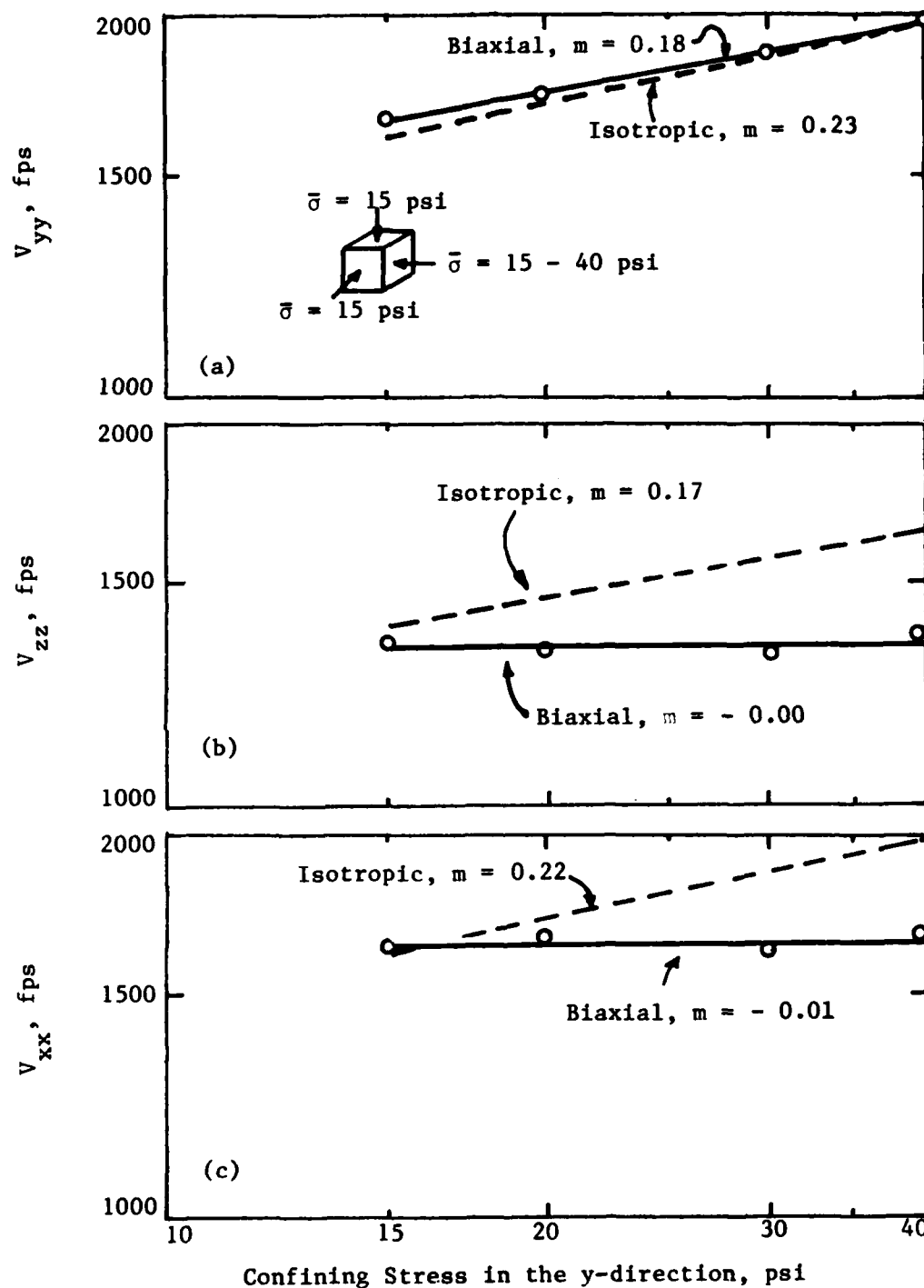


Fig. 6.8 - Variation in P-wave Velocities Under Biaxial Conditions for Stress Increasing Along y-direction

TABLE 6.1

Comparison of Constants and Slopes for  
Equations Relating  $V_p$  to  $\bar{\sigma}_o$  for Isotropic Confinement\*  
and  $V_p$  to  $\bar{\sigma}_a$  for Biaxial Confinement\*\* with  
Variation of Stress in One Principal Direction\*\*\*

DIRECTION	$C_1$		$m$	
	ISOTROPIC	BIAXIAL	ISOTROPIC	BIAXIAL
X (NS)	308	369	0.22	0.20
Y (EW)	280	432	0.23	0.18
Z (TB)	371	342	0.17	0.19

$$*V_p = C_1 \bar{\sigma}_o^m \quad (\text{Isotropic Confinement, Eq. 4.2})$$

$$**V_p = C_1 \bar{\sigma}_a^m \quad (\text{Biaxial Confinement, Eq. 6.1})$$

\*\*\*Biaxial conditions are shown in Fig. 6.1



equation for biaxial confinement only relates P-wave velocity to the stress in the direction of wave propagation, stresses in the other two principal directions perpendicular to the direction of propagation have very little effect on P-wave velocity.

As shown in the middle and bottom curves of Figs. 6.6 to 6.8, P-wave velocities along directions of constant stress are almost constant with the largest percentage difference less than 6 percent. This is just experimental scatter since some velocities increase and some decrease. The results are reasonable (for velocities to remain constant in the direction of constant stress) if P-wave velocity can be expressed by Eq. 6.1.

It should be noted that at 15 psi (103 kPa), the loading condition is actually an isotropic confinement. Therefore, the P-wave velocities measured under this loading condition should be the same as those under isotropic confinement and the two straight lines should intersect each other at 15 psi (103 kPa). This is shown in Figs. 6.6 to 6.8 with small experimental scatter and once again the effect of stress history is confirmed to be negligible.

It is also interesting to observe that complete anisotropy of the system resulted from the coupling of structural anisotropy and

stress anisotropy. The sand specimen is known to be cross-anisotropic due to structural anisotropy (Section 4.3). Under biaxial loading with different horizontal stresses, soil properties in the two horizontal directions will also be different due to stress-induced anisotropy and, therefore, complete anisotropy resulted. Complete anisotropy under biaxial loading is shown by condensing the solid curves in Figs. 6.7(a) to 6.7(c) into a single figure which is shown in Fig. 6.9. Compression wave velocities in each direction are different from one another (complete anisotropy) except at 15 psi (103 kPa) where the velocities in the horizontal directions are equal for the isotropic confinement (no stress anisotropy). Therefore, complete anisotropy resulted in biaxial conditions shown in Figs. 6.1(b), 6.1(c), 6.2(b), 6.3(b) and 6.3(c).

#### 6.2.4 Effect of Intermediate Principal Effective Stress

The results presented so far are for biaxial conditions with the intermediate principal effective stress always equal to the minor principal effective stress. For the biaxial conditions shown in Fig. 6.2, the intermediate principal stress is equal to the major principal stress at the start of testing and then changes to be equal to the minor principal stress in the later stages. Tests with these biaxial

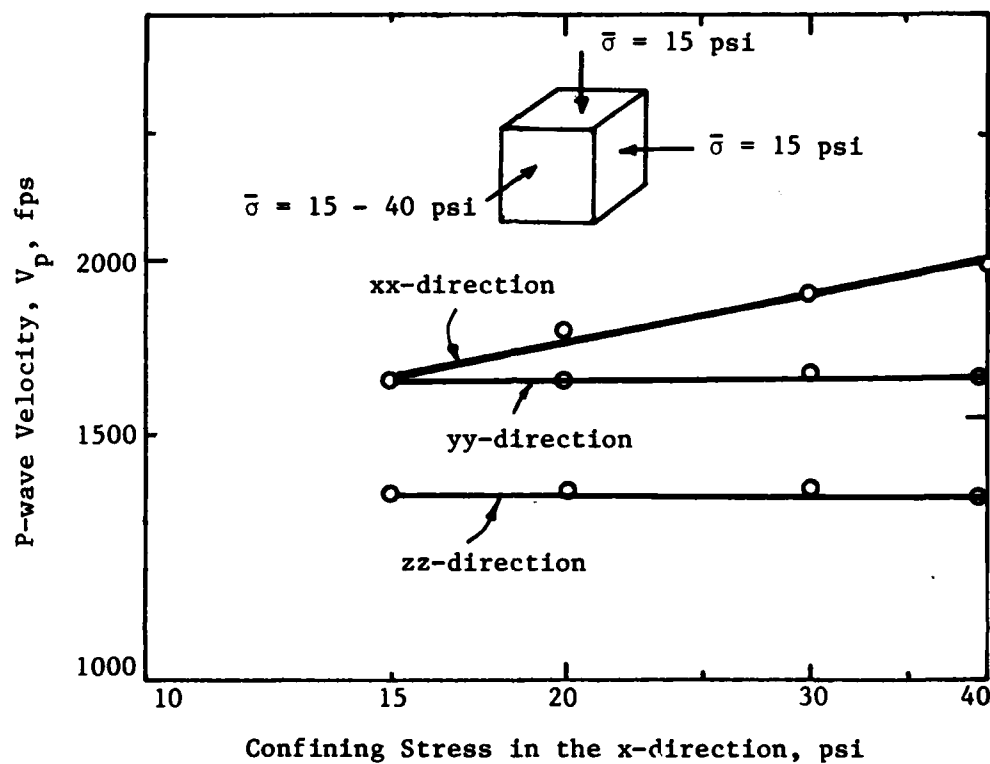


Fig. 6.9 - Effect of Complete Anisotropy on P-wave Velocities Under Biaxial Condition with Different Horizontal Confining Stresses

conditions were performed to investigate if there is any effect of intermediate principal stress on P-wave velocity.

Results of the biaxial conditions shown in Figs. 6.2(a) and 6.2(b) are shown in Figs. 6.10 and 6.11, respectively. Comparable biaxial conditions with increasing confining stress in the same directions are also shown in Figs. 6.10 and 6.11. Since the P-wave velocities are very close to each other for both stress conditions, there is no discernible effect of intermediate principal stress on the P-wave velocities and Eq. 6.1 is applicable for both cases. Compression waves propagating along directions of constant stress have almost constant values for P-wave velocities and the results appeared as horizontal straight lines in Figs. 6.10 and 6.11.

### 6.3 VARIATION OF STRESS IN TWO PRINCIPAL DIRECTIONS

For the conditions shown in Fig. 6.3, two of the three principal stresses were changed during each test. Velocities of compression waves propagating along axes with increasing confining stress are plotted against the confining stress in Fig. 6.12. Compression wave velocities obtained under isotropic confinement are also shown for comparison purposes. All of the resulting straight lines are in close agreement to each other showing same trend in the variation of  $V_p$

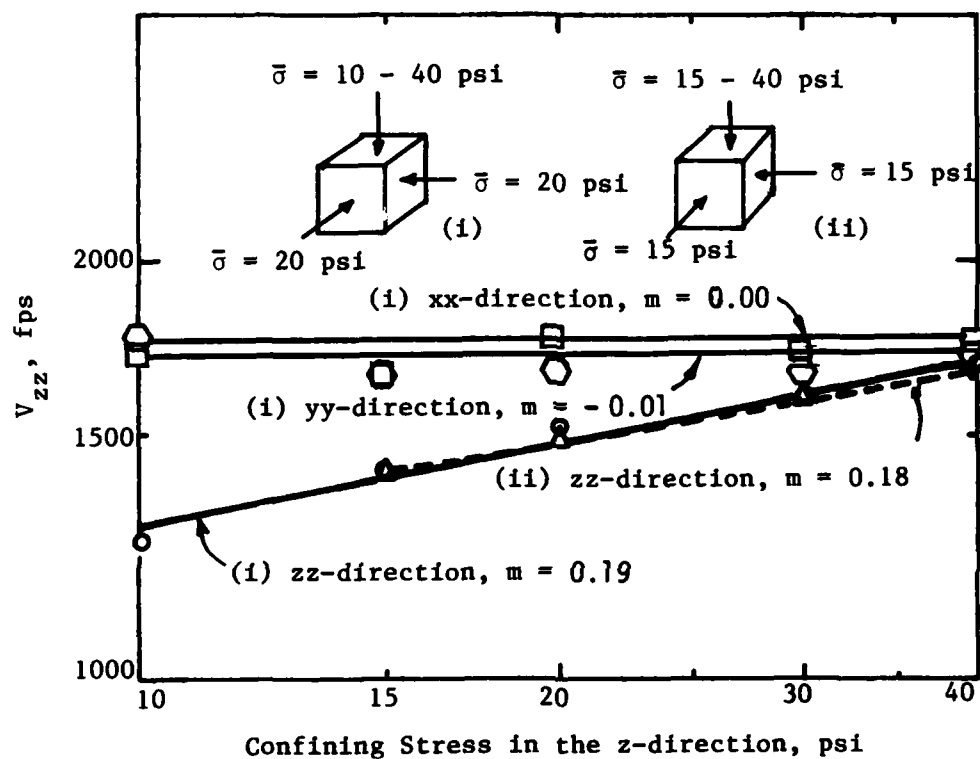


Fig. 6.10 - Effect of Intermediate Principal Stress on  $V_p$  with Stress Increasing Along the z-direction

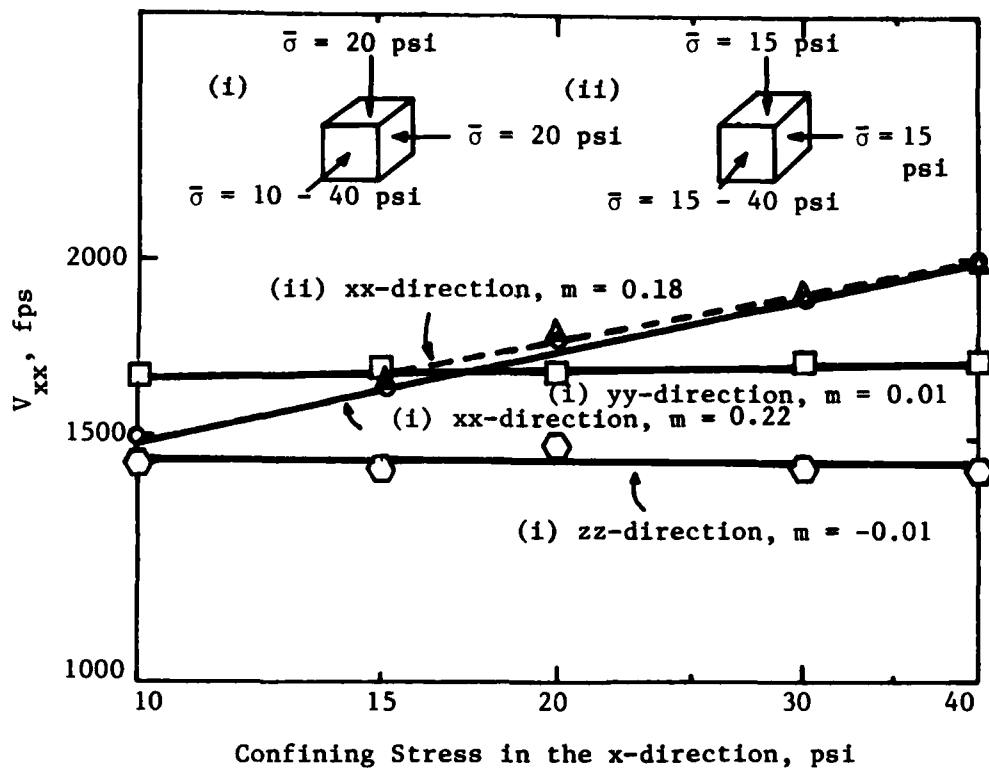


Fig. 6.11 - Effect of Intermediate Principal Stress on  $V_p$  with Stress Increasing Along the x-direction

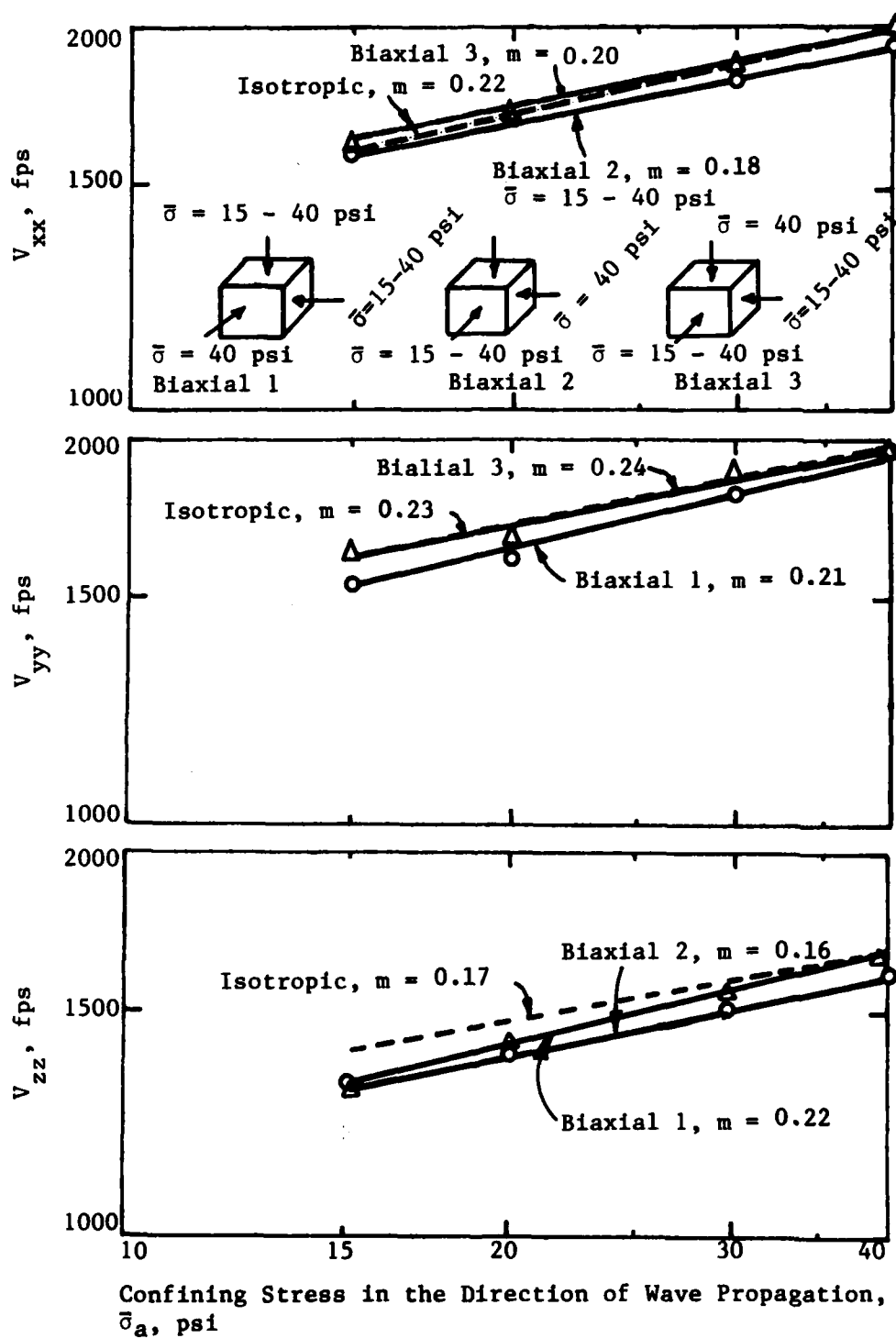


Fig. 6.12 - Variation in P-wave Velocities Along Directions of Increasing Stress Under Biaxial Confinement with Two Principal Stresses Changing

with confining stress. The largest difference between P-wave velocities under isotropic confinement and biaxial confinement is shown in Fig. 6.12(c) at 15 psi (103 kPa) at which point the difference is 12 percent. The average of the percentage differences in P-wave velocities shown in Fig. 6.12 is 4 percent. The scatter is small and once again Eq. 6.1 is applicable for P-wave velocities propagating along axes of increasing confining stress. Values of the constants in Eq. 6.1 derived from the results presented in Fig. 6.12 are summarized in Table 6.2.

Velocities of P-waves propagating along axes of constant confining stress are shown in Fig. 6.13. The P-wave velocities in each of the principal axes with constant confining stress remained more or less constant. The resulting straight lines are almost horizontal with small values for the slopes. Structural anisotropy is also depicted in Fig. 6.13 since the velocities in the horizontal directions are almost the same and are about 17 percent higher than the velocities in the vertical direction.

#### 6.4 SUMMARY

From the results of P-wave velocities measured under repeated biaxial conditions, it was shown that the effect of stress



TABLE 6.2

Comparison of Constants and Slopes for Equations  
 Relating  $V_p$  to  $\bar{\sigma}_a$  for Isotropic Confinement\*  
 and  $V_p$  to  $\bar{\sigma}_a$  for Biaxial Confinement\*\*  
 with Variation of Stress in Two Principal Directions\*\*\*

DIRECTION	STRESS STATE	$C_1$	$m$
X	ISOTROPIC	308	0.22
	BIAXIAL 2 <sup>†</sup>	431	0.18
	BIAXIAL 3	342	0.20
Y	ISOTROPIC	280	0.23
	BIAXIAL 1	366	0.21
	BIAXIAL 3	256	0.24
Z	ISOTROPIC	371	0.17
	BIAXIAL 1	227	0.22
	BIAXIAL 2	443	0.16

$$*V_p = C_1 \bar{\sigma}_o^m \quad (\text{Isotropic Confinement, Eq. 4.2})$$

$$**V_p = C_1 \bar{\sigma}_a^m \quad (\text{Biaxial Confinement, Eq. 6.1})$$

\*\*\*Biaxial conditions are shown in Fig. 6.3

<sup>†</sup>See insert in Fig. 6.12

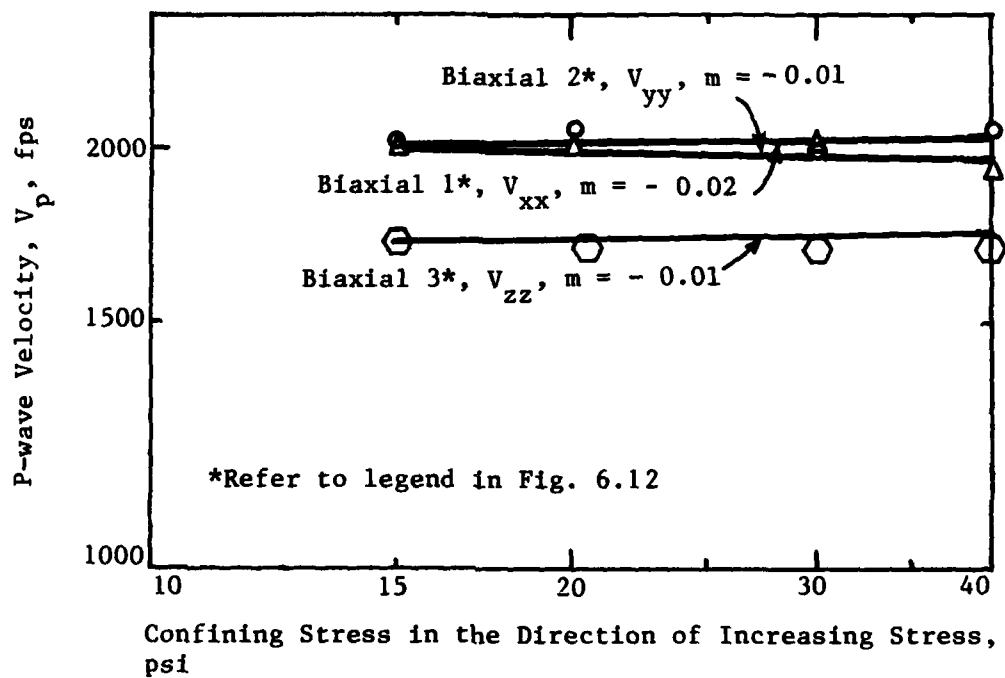


Fig. 6.13 - Variation in P-wave Velocities Along Directions of Constant Stress Under Biaxial Confinement with Two Principal Stresses Changing

history on P-wave velocities of this sand was negligible. Therefore, averages of P-wave velocities measured under loading and unloading conditions were used for analysis purposes, and the small effect of stress history was neglected.

For biaxial conditions with equal horizontal confining stresses, the sand specimen behaved as a cross-anisotropic material with wave propagation velocities in the horizontal directions equal and different from  $V_p$  in the vertical direction. However, when the two horizontal confining stresses are different, the resulting stress anisotropy couples with structural anisotropy to produce a complete anisotropic material. Compression wave velocities in a complete anisotropic material have different values in each of the three principal axes. However, the same equation (Eq. 6.1) is applicable to velocities of P-waves propagating along directions of increasing stress in the complete anisotropic state.

Curves for average values of velocities of P-waves propagating along each principal axis with increasing confining stress from all the appropriate biaxial conditions shown in Figs. 6.1 to 6.3 are shown in Fig. 6.14. The three straight lines are almost identical to those in Fig. 4.2 for the isotropic condition except that P-wave velocities in the vertical direction are 3 to 4 percent less than those under iso-

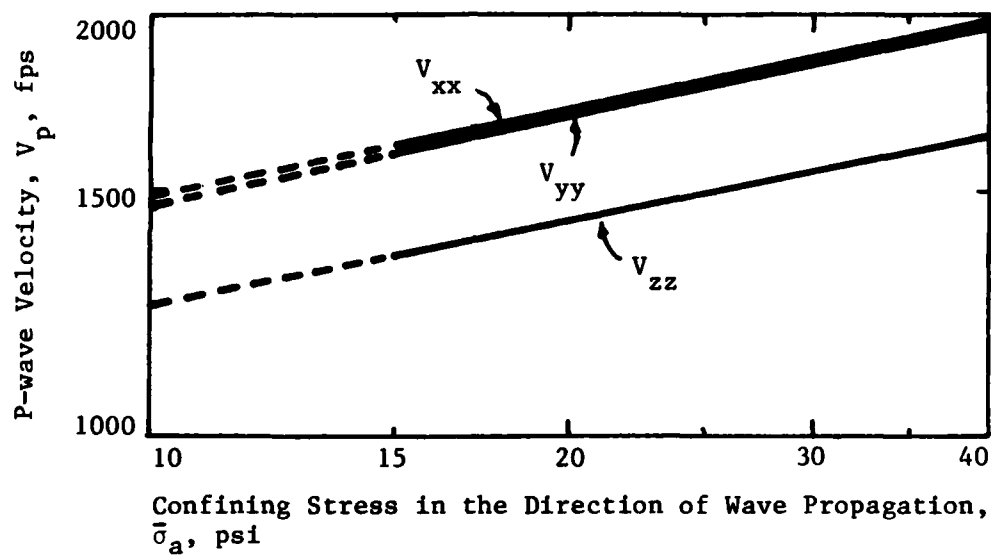


Fig. 6.14 - Effect of Structural Anisotropy on  $V_p$   
Under Biaxial Confinement

tropic conditions. The values of constants in Eq. 6.1 for the straight lines shown in Fig. 6.14 are summarized in Table 6.3 together with those for biaxial loading conditions reported by Kopperman et al (1982).

TABLE 6.3

Comparison of Constants and Slopes for Eq. 6.1\*  
 Relating  $V_p$  to  $\bar{\sigma}_a$  for Biaxial Confinement with  
 Those Reported by Kopperman et al (1982)

	$C_1$		$m$	
DIRECTION	PRESENT STUDY	KOPPERMAN ET AL	PRESENT STUDY	KOPPERMAN ET AL
X	330	218	0.21	0.24
Y	284	293	0.22	0.20
Z	293	287	0.20	0.20

$$*V_p = C_1 \bar{\sigma}_a^m$$

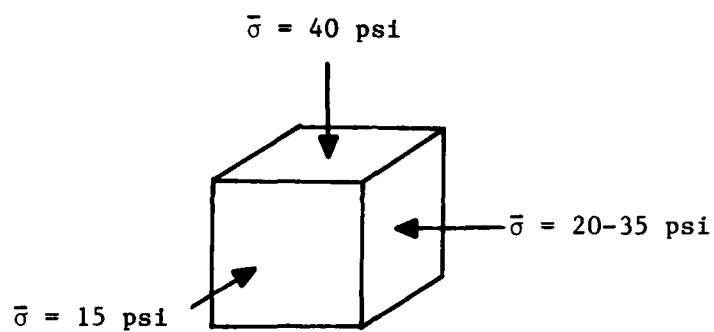
## CHAPTER SEVEN

### TRIAXIAL CONFINEMENT

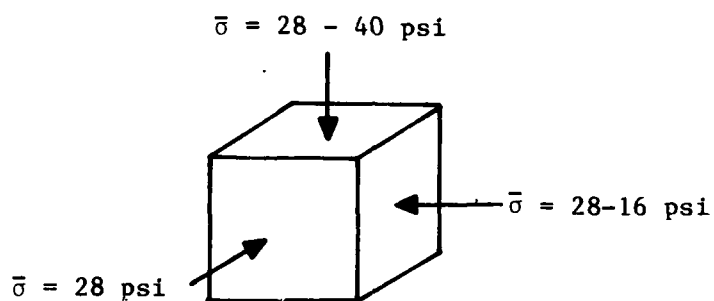
#### 7.1 INTRODUCTION

The last step in the study of the effect of confining pressure on compression wave velocity was to perform tests with triaxial confinement. Conditions of triaxial confinement were obtained when all stresses in principal directions had different values, i.e. when the major principal stress was greater than the intermediate principal stress which was in turn greater than the minor principal stress ( $\bar{\sigma}_1 > \bar{\sigma}_2 > \bar{\sigma}_3$ ).

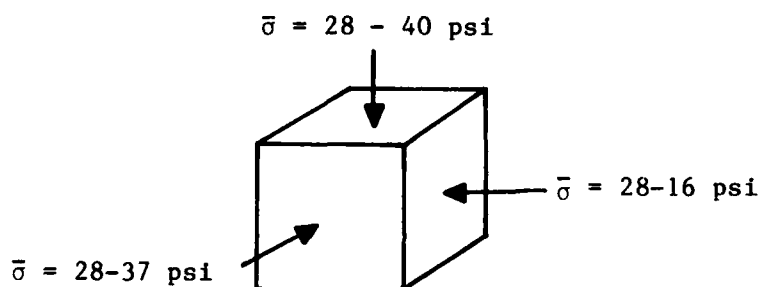
The complete set of triaxial confinement tests was composed of three series of tests: 1. the first series consisted of tests in which confining stress was varied in only one principal direction, 2. the second series consisted of tests in which confining stress was varied in two principal directions, and 3. the third series consisted of tests in which confining stress was varied in all three principal directions. The loading conditions for each series are shown in Fig. 7.1. The exact sequence of these loading conditions is shown in Fig. 3.7. Unloading tests were not performed since results from previous



a) First Series



b) Second Series



c) Third Series

Fig. 7.1 - Loading Conditions for Triaxial Confinement Tests



tests (Sections 4.2 and 6.2.1) had shown that the effect of stress history on P-wave velocities was negligible.

Compression wave velocities were measured along each principal stress axis under each triaxial state. The same procedure discussed in Section 3.5 was used to analyze all data. Results and conclusions for the first, second and third series of triaxial confinement tests are presented in Sections 7.2, 7.3 and 7.4, respectively.

## 7.2 VARIATION OF STRESS IN ONE PRINCIPAL DIRECTION

As shown in Fig. 7.1(a), the first series of triaxial confinement tests started with stresses in the x-, y- and z-directions having values of 15 psi (103 kPa), 20 psi (138 kPa) and 40 psi (276 kPa), respectively. The intermediate principal stress was then increased from 20 psi (138 kPa) to 35 psi (241 kPa) in increments of 5 psi (34 kPa) while the major and minor principal stresses in the z- and x- directions, respectively, remained unchanged. Velocities obtained with these stress conditions could be used, therefore, to study the effect of intermediate principal stress on P-wave velocities under triaxial confinement.

### 7.2.1 Effect of Intermediate Principal Stress

Compression wave velocities obtained from the stress conditions shown in Fig. 7.1(a) are plotted against the stress in the y-direction (the intermediate principal stress in this case) in Fig. 7.2. As shown in the figure, compression waves propagating along axes of constant stress (x- and z- axes) travelled at almost constant values of velocities and, hence, were independent of the increasing intermediate principal stress. The resulting curves therefore appear as nearly horizontal lines in Fig. 7.2. On the other hand, P-waves propagating along the axis of the intermediate principal stress exhibited velocities which increased with increasing stress with a linear relationship as shown in Fig. 7.2. As a result, Eq. 6.1 (which was patterned after Eq. 4.2 for isotropic confinement) for biaxial confinement could be used to express the relationship between P-wave velocity and confining stress in the direction of wave propagation for triaxial confinement.

The best-fit straight line obtained from measurements under isotropic conditions of P-waves propagating in the y-direction is also shown in Fig. 7.2. Since the two straight lines are almost on top of each other, the relationship between P-wave velocity and confining

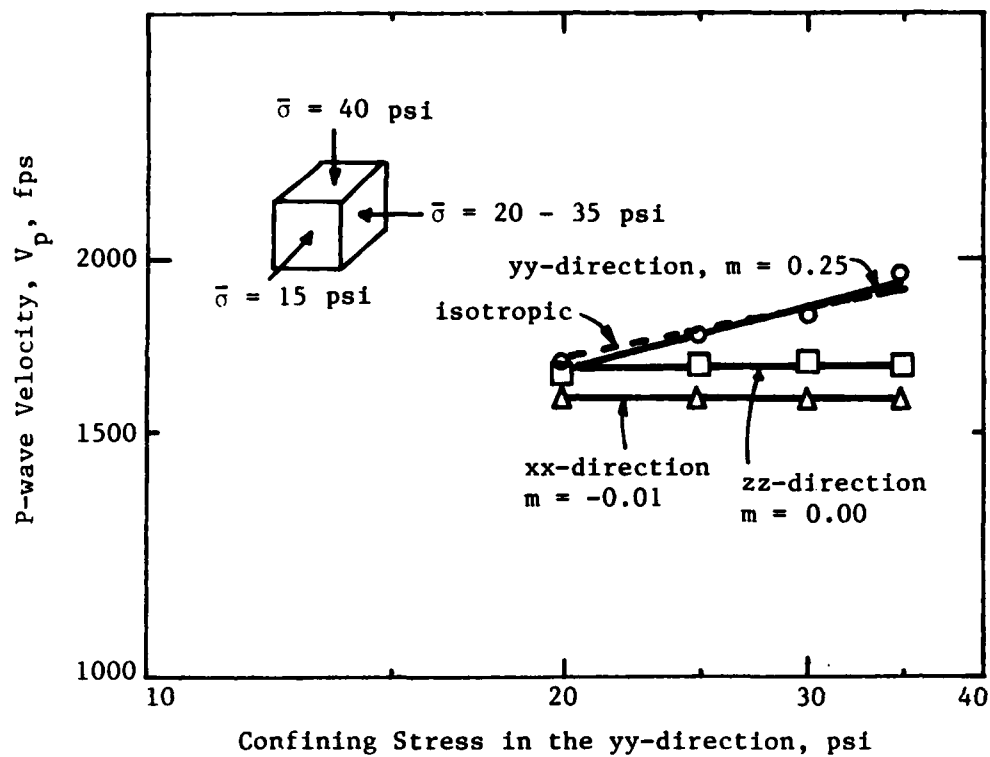


Fig. 7.2 - Variation of Compression Wave Velocities Under Triaxial Confinement When Only One Principal Stress Varied

stress in the direction of wave propagation is the same for both isotropic and triaxial confinements.

### 7.3 VARIATION OF STRESS IN TWO PRINCIPAL DIRECTIONS

As shown in Fig. 7.1(b), the second series of triaxial confinement tests started with an isotropic condition of 28 psi (193 kPa). Then, the stress in the y-direction was decreased from 28 psi (193 kPa) to 16 psi (110 kPa) in decrements of 4 psi (28 kPa) while the stress in the z-direction was increased from 28 psi (193 kPa) to 40 psi (276 kPa) in increments of 4 psi (28 kPa). As a result, the stress in the x-direction represented the intermediate principal stress which remained constant at 28 psi (193 kPa) while the minor and major principal stresses in the y- and z- directions, respectively, varied according to the pattern described above.

#### 7.3.1 Effect of Major and Minor Principal Stresses

For the stress conditions shown in Fig. 7.1(b), P-wave velocities in the x-direction varied from 1761 ft/s (537 m/s) to 1792 ft/s (547 m/s) with an average value of 1775 ft/s (541 m/s) and standard deviation of 14 ft/s (4 m/s). Therefore, P-wave velocities in the x-direction (intermediate principal stress direction) could be consid-

ered as constant at 1775 ft/s (541 m/s) and independent of the varying major and minor principal stresses. Consequently, P-wave velocities in the x-direction appear as a single point at  $\bar{\sigma}_a$  equal to 28 psi (193 kPa) in Fig. 7.3.

Compression wave velocities measured in the major and minor principal stress directions are plotted against confining stress in the direction of wave propagation in Fig. 7.3. The two resulting best-fit straight lines were shown as solid lines in the figure. The best-fit straight lines obtained under isotropic conditions are also shown in Fig. 7.3 as dashed lines for comparison purposes. Since the solid lines are very close to the dashed lines, Eq. 6.1 could be used to express the relationship between P-wave velocity and confining stress in the direction of wave propagation under this type of triaxial confinement.

#### 7.4 VARIATION OF STRESS IN ALL PRINCIPAL DIRECTIONS

As shown in Fig. 7.1(c), the third series of triaxial confinement tests also started with an isotropic condition of 28 psi (193 kPa). Then the stress in the x-direction was increased from 28 psi (193 kPa) to 37 psi (255 kPa) in increments of 3 psi (21 kPa) while stress variations in the y- and z-directions were the same as in the second

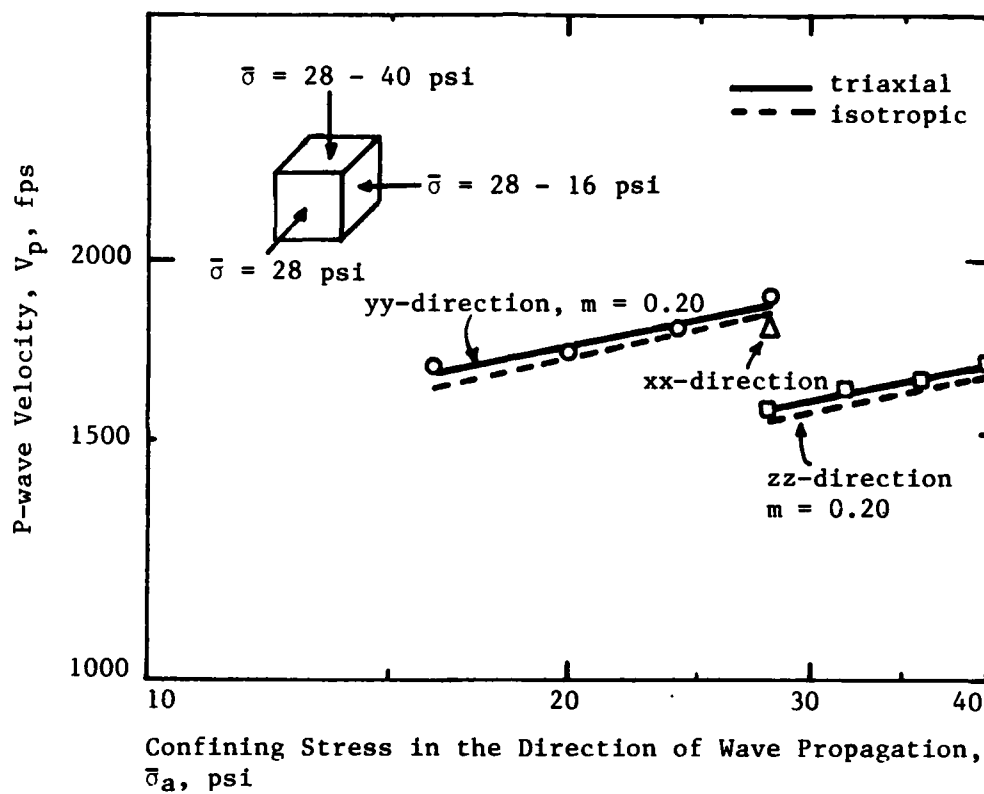


Fig. 7.3 - Variation of Compression Wave Velocities Under Triaxial Confinement When Two Principal Stresses Varied

series of tests (Section 7.3). Therefore, confining stresses in all directions varied with the stresses in the z-, x- and y-directions being the major, intermediate and minor principal stresses, respectively.

#### 7.4.1 Effect of Principal Stresses

Compression wave velocities obtained from stress conditions shown in Fig. 7.1(c) are plotted against the confining stress in the direction of wave propagation in Fig. 7.4. In this case, each confining stress is one of the principal stresses. As shown in Fig. 7.4, three best-fit straight lines (solid lines in the figure) were obtained: one for each principal direction. Best-fit straight lines obtained under isotropic conditions are also shown in Fig. 7.4 as dashed lines. Once again the behavior under triaxial loading is very close to that determined under isotropic and biaxial conditions, and hence Eq. 6.1 can be used to express the relationship between P-wave velocity and confining stress in the direction of wave propagation.

It should be noted that due to structural anisotropy, P-wave velocities in the z-direction are less than those in the x- and y-directions which were approximately equal. This is in same relative

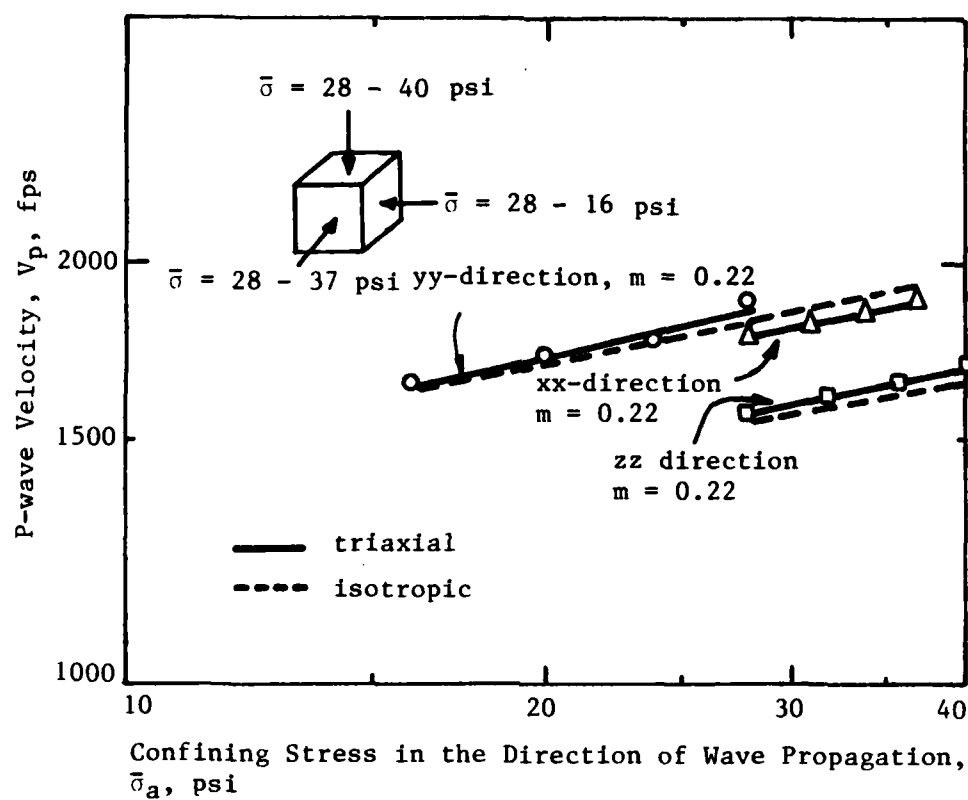


Fig. 7.4 - Variation of Compression Wave Velocities  
 Under Triaxial Confinement When All Principal Stresses Varied



ordering of wave velocities with directions as observed under isotropic loading (Fig. 4.2).

An effort was made to develop a generalized equation relating P-wave velocities in one principal direction to confining stresses in all three principal directions under triaxial confinement. This generalized equation had the form of:

$$V_{xx} = C \bar{\sigma}_{xx}^{mx} \bar{\sigma}_{yy}^{my} \bar{\sigma}_{zz}^{mz} \quad (7.1)$$

in which the four constants had to be determined from velocity and stress data. It just so happened that there were four sets of data to fulfill the minimum requirement of measured values of variables. Ideally, the power for the stress in the direction of wave propagation should have a value in the range of 0.20 to 0.25 while stresses in other two perpendicular directions should have powers close to zero. However, results from multiple regression analysis had values of the parameters  $C$ ,  $m_x$ ,  $m_y$  and  $m_z$  far different from the expected values and varied randomly from analysis for P-wave velocities in each of the principal directions. Therefore, it was believed that the sample population was too small, and results from multiple regression analysis were too sensitive to provide any valid statistical model for the P-wave velocities and stresses in the principal directions under triaxial confinement.

## 7.5 SUMMARY

Three series of triaxial confinement tests were performed to study the effect of stress states on P-wave velocities. The results from the first, second and third series of tests are presented in Sections 7.2, 7.3 and 7.4, respectively. All results led to the same conclusion that it is essentially the confining stress in the direction of wave propagation that controls the P-wave velocity and the relationship can be expressed by Eq. 6.1.

Best-fit straight lines obtained from the average of the three series of triaxial confinement tests are shown as solid lines in Fig. 7.5. Best-fit straight lines obtained under isotropic conditions are also shown in Fig. 7.5 (as dashed lines). Once again, both sets of straight lines are very close to each other indicating that Eq. 6.1 can be applied for both isotropic and triaxial confinements. Constants for these lines are summarized in Table 7.1.

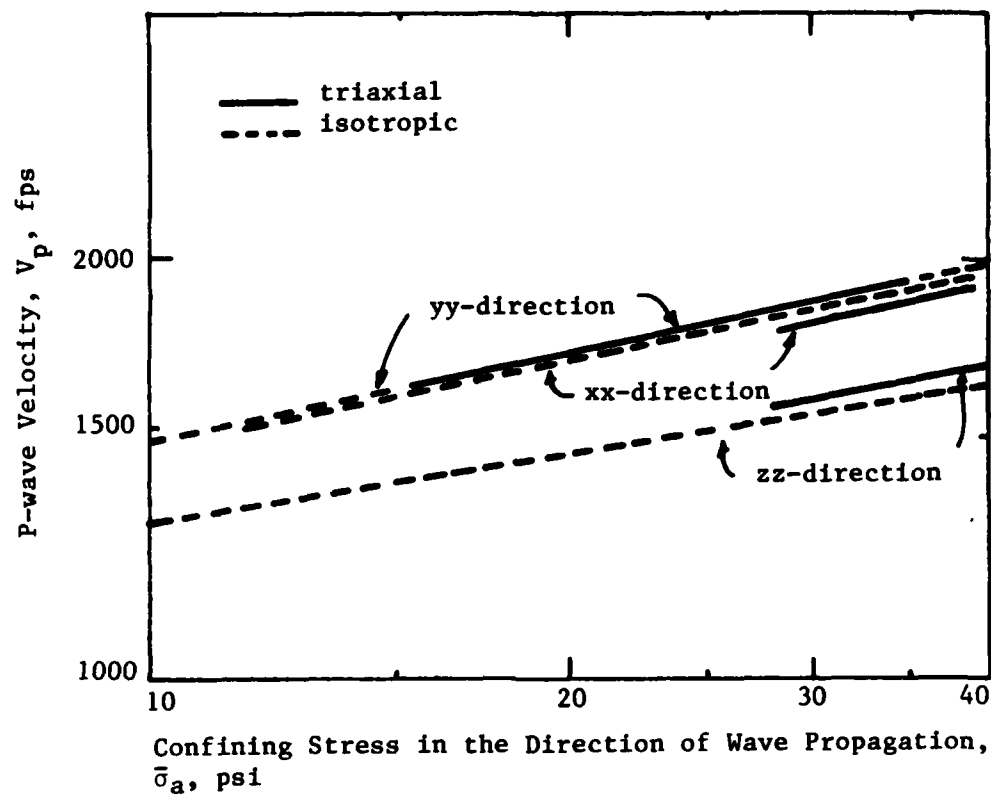


Fig. 7.5 - Comparison of Wave Velocities Under Isotropic and Triaxial Confinements

TABLE 7.1

Comparison of Constants and Slopes for Equations  
 Relating  $V_p$  to  $\bar{\sigma}_0$  for Isotropic Confinement\*  
 and  $V_p$  to  $\bar{\sigma}_a$  for Triaxial Confinement\*\*

DIRECTION	$C_1$		$m$	
	ISOTROPIC	TRIAXIAL	ISOTROPIC	TRIAXIAL
X (NS)	308	287	0.22	0.22
Y (EW)	280	282	0.23	0.23
Z (TB)	371	272	0.17	0.21

$$*V_p = C_1 \bar{\sigma}_0^m \quad (\text{Isotropic Confinement Eq. 4.2})$$

$$**V_p = C_1 \bar{\sigma}_a^m \quad (\text{Triaxial Confinement, same as Eq. 6.1 for Biaxial Confinement})$$

## CHAPTER EIGHT

### SUMMARY AND CONCLUSIONS

#### 8.1 SUMMARY

One sample of dry sand was tested in this study. The sand was the same as that used by Kopperman et al (1982) and Knox (1982) in similar earlier studies. The sample was constructed with a special raining device (Section 2.3) constructed as part of the project. With this raining device, it was possible to construct a uniform sample with a void ratio of  $0.64 \pm 0.03$  and dry density of  $101.8 \text{ pcf} \pm 2.0 \text{ pcf}$  ( $1629 \text{ kg/m}^3 \pm 32 \text{ kg/m}^3$ ).

Tests with various combinations of principal stresses were performed with the sand sample, namely: isotropic confinement ( $\bar{\sigma}_1 = \bar{\sigma}_2 = \bar{\sigma}_3$ ), biaxial confinement ( $\bar{\sigma} > \bar{\sigma}_2 = \bar{\sigma}_3$  or  $\bar{\sigma}_1 = \bar{\sigma}_2 > \bar{\sigma}_3$ ), and triaxial confinement ( $\bar{\sigma}_1 > \bar{\sigma}_2 > \bar{\sigma}_3$ ). In each test, velocities of P-waves propagating along each principal axis were measured, and the results were used to study the effects of confinement on P-wave velocity.

## 8.2 CONCLUSIONS

From the results of P-wave velocity measured under various isotropic, biaxial and triaxial confinement states, the following conclusions have been reached.

1. Under isotropic confinement, the relationship between P-wave velocity and isotropic confining pressure can be expressed in the form used by Hardin and Richart (1963):

$$V_p = C_1 \bar{\sigma}_o^m \quad (8.1)$$

where:  $V_p$  = P-wave velocity, in fps,

$\bar{\sigma}_o$  = isotropic confining pressure, in psf,

$C_1$  = constant ( $C_1 = V_p$  when  $\bar{\sigma}_o = 1$  psf), and

$m$  = slope of the curve.

2. The effect of stress history on P-wave velocity is small and can be neglected.

3. Due to structural anisotropy, the sand sample under isotropic confinement can be treated as a cross-anisotropic material with the horizontal plane as the plane of symmetry. It takes five independent constants to determine completely the cross-anisotropic model.

Under biaxial confinement with different horizontal confining stresses or under triaxial confinement, stress anisotropy couples with structural anisotropy to produce a completely anisotropic model for the sand sample.

4. Under biaxial confinement, the relationship between P-wave velocity and confining stress in the direction of wave propagation,  $\bar{\sigma}_a$ , can be expressed by:

$$V_p = C_1 \bar{\sigma}_a^m \quad (8.2)$$

It should be noted that Eq. 8.2 (instead of Eq. 8.1) can also be used for isotropic confinement because the mean effective principal stress,  $\bar{\sigma}_0$ , is equal to the principal effective stress in the direction of wave propagation,  $\bar{\sigma}_a$ . Besides, Eq. 8.2 had been verified for biaxial conditions with one or two effective principal stresses varying.

5. Under triaxial confinement, the same equation (Eq. 8.2) can be used to express the relationship between P-wave velocity and confining stress in the direction of wave propagation.

6. For this sand sample, the general equation relating P-wave velocity and confining stress in the direction of wave propagation can be expressed by Eq. 8.2, independent of stress state. The

values obtained for the constant and slope in Eq. 8.2 for various confinements are summarized in Table 8.1. For this sand, the general equation can be written as:

$$v_p = 334 \bar{\sigma}_a^{0.20} \quad (8.3)$$



TABLE 8.1

Summary of Constants and Slopes for Eq. 8.2\*  
 Relating  $V_p$  to  $\bar{\sigma}_a$  for Various Confinements

STRESS STATE	DIRECTION					
	X (NS)		Y (EW)		Z (TB)	
	$C_1$	m	$C_1$	m	$C_1$	m
ISOTROPIC	308	0.22	280	0.23	371	0.17
BIAXIAL	330	0.21	295	0.22	327	0.18
TRIAXIAL	296	0.22	331	0.21	272	0.21
AVERAGE	314	0.21	273	0.23	316	0.19

$$*V_p = C_1 \bar{\sigma}_o^m$$

APPENDIX A

STRAIN CALIBRATION FOR STRAIN SENSOR

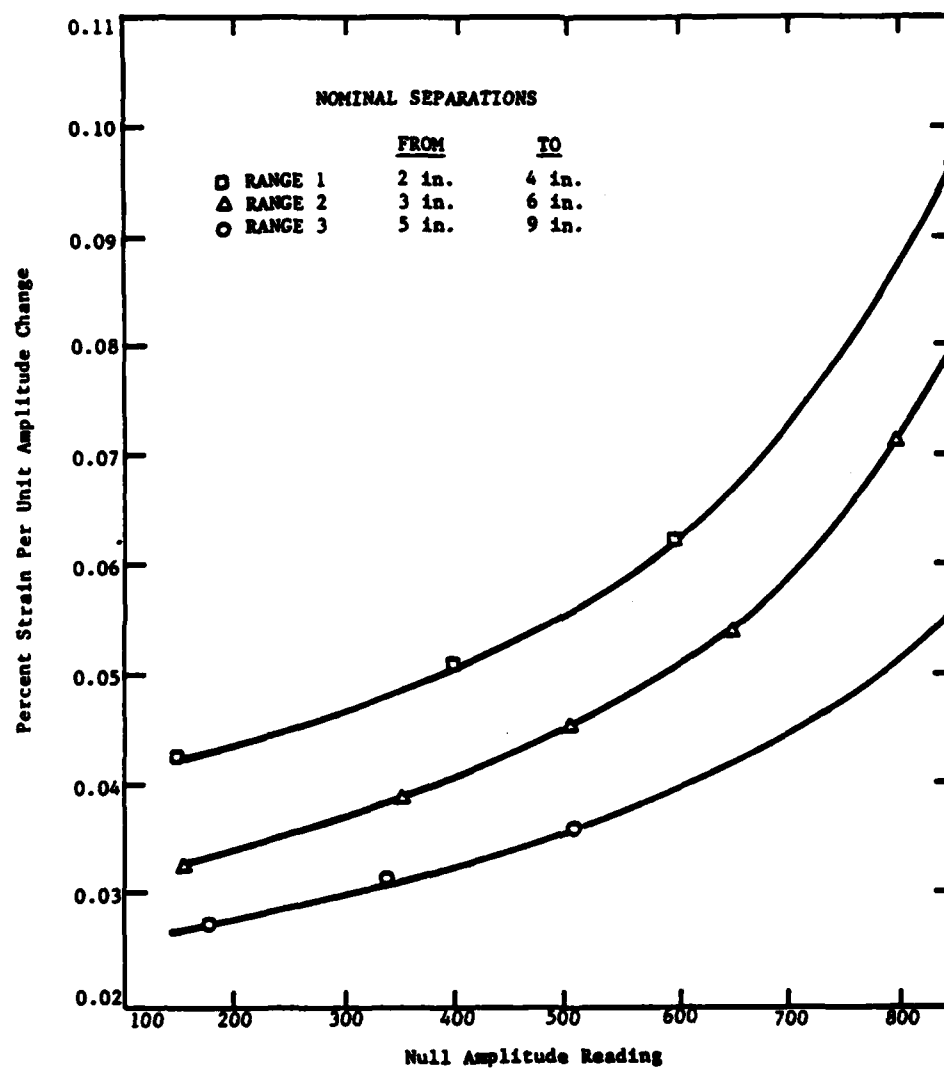


Fig. A.1 - Strain Calibration for Strain Sensor SN-2

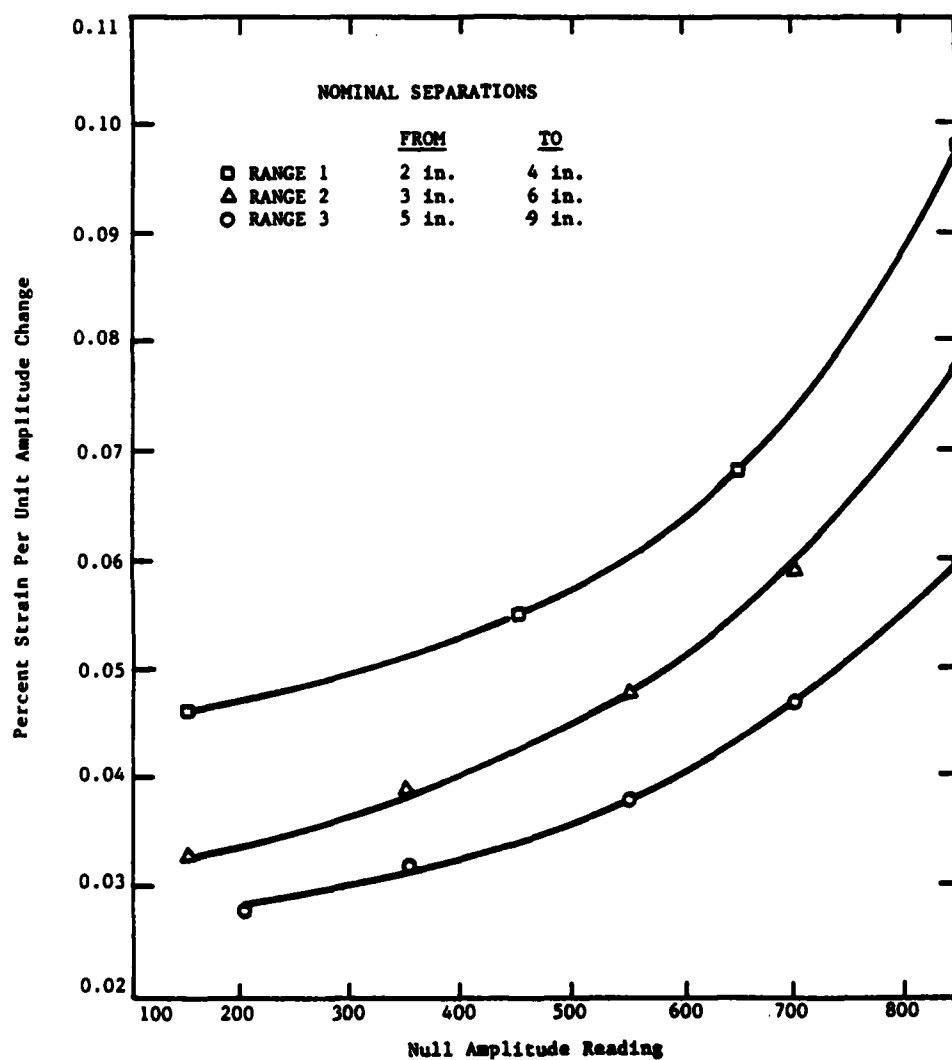


Fig. A.2 - Strain Calibration for Strain Sensor SN-3

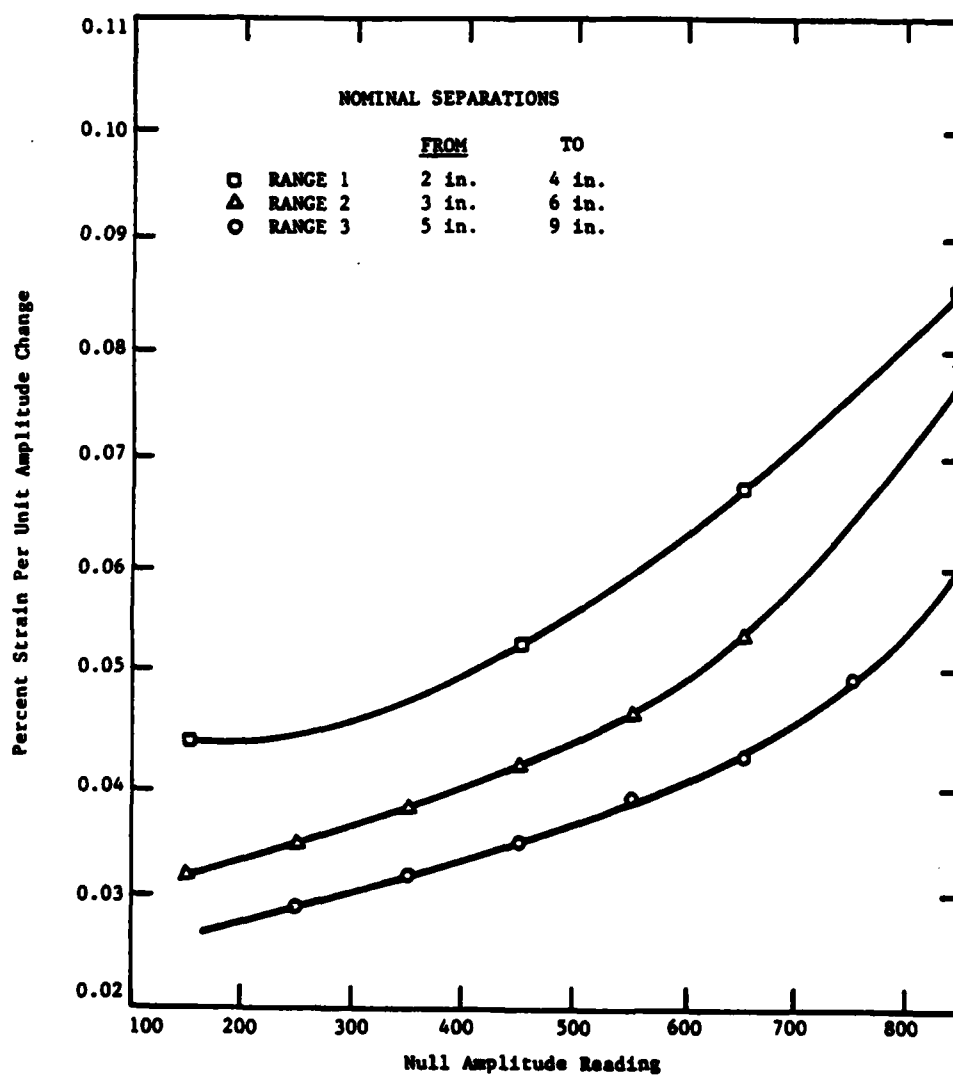


Fig. A.3 - Strain Calibration for Strain Sensor SN-4

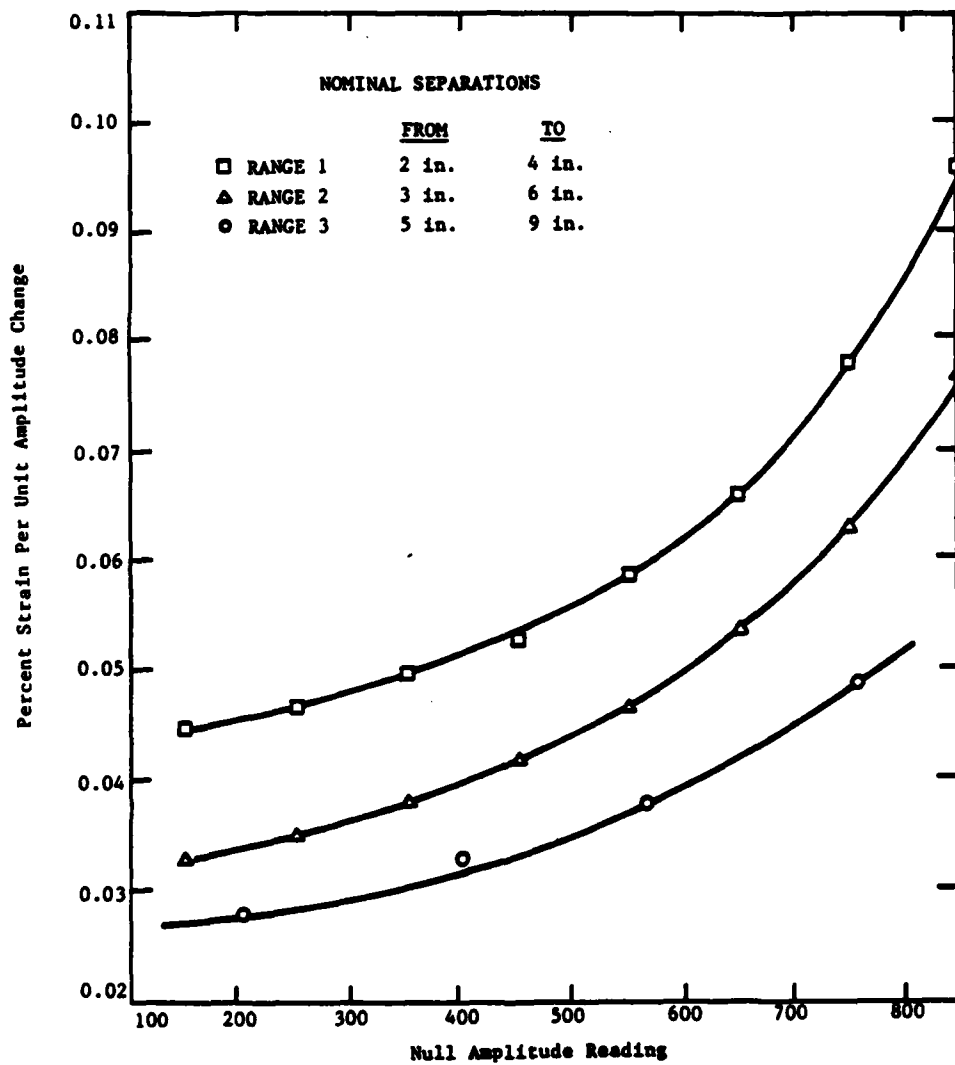


Fig. A.4 - Strain Calibration for Strain Sensor SN-5

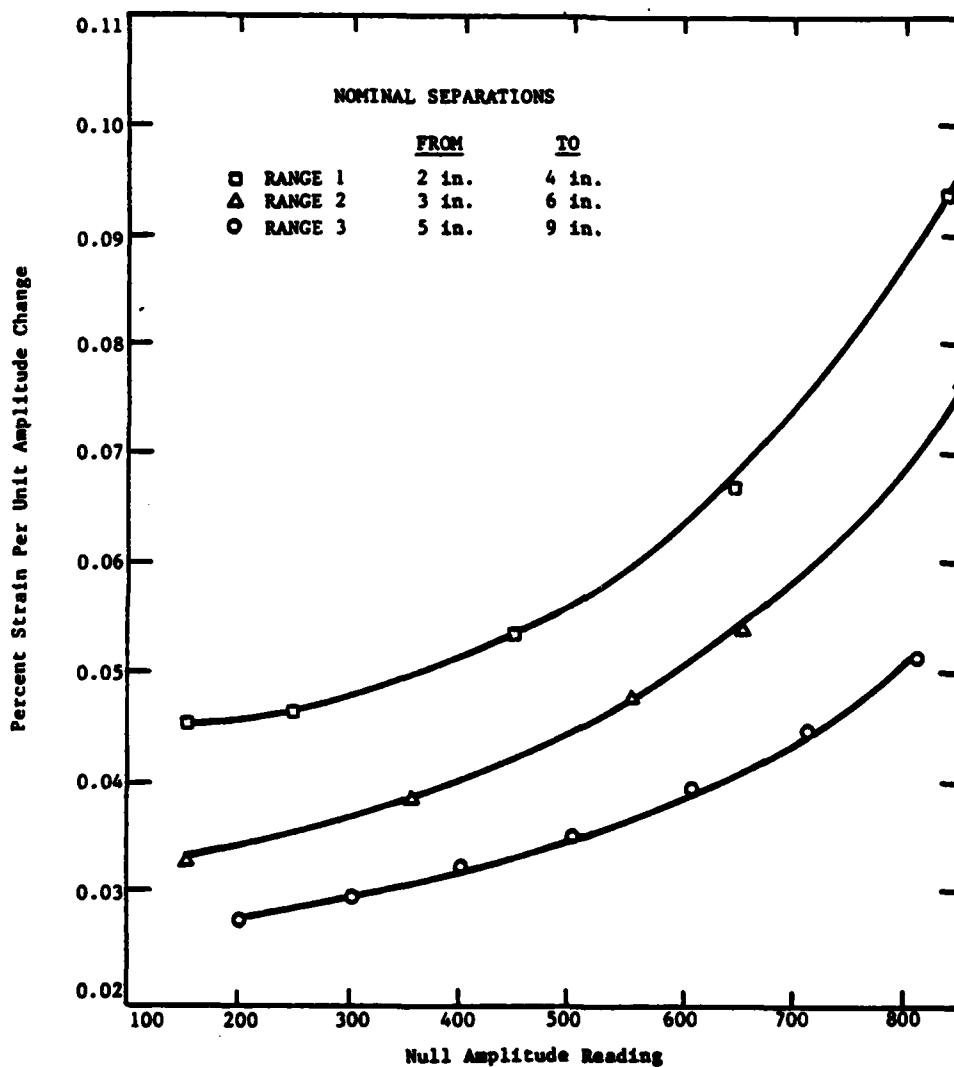


Fig. A.5 - Strain Calibration for Strain Sensor SN-6

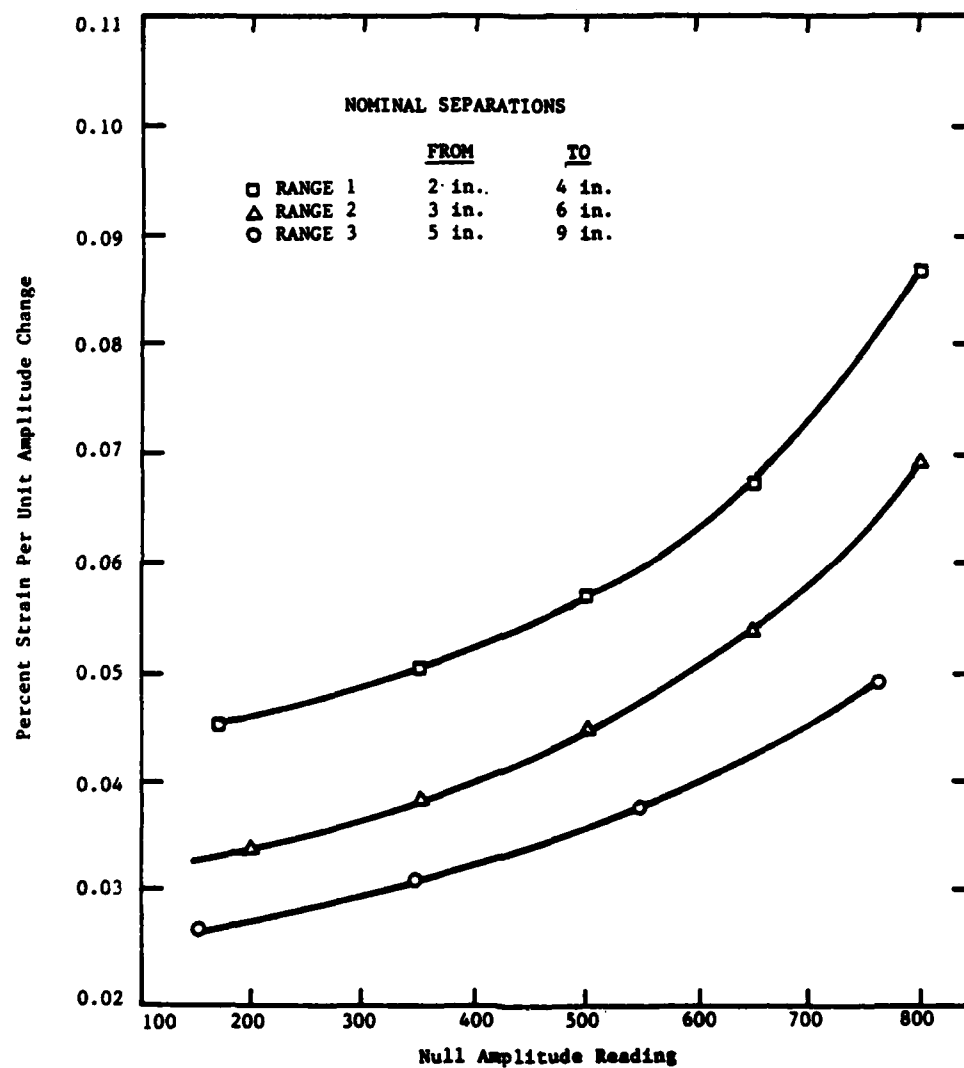


Fig. A.6 - Strain Calibration for Strain Sensor SN-7



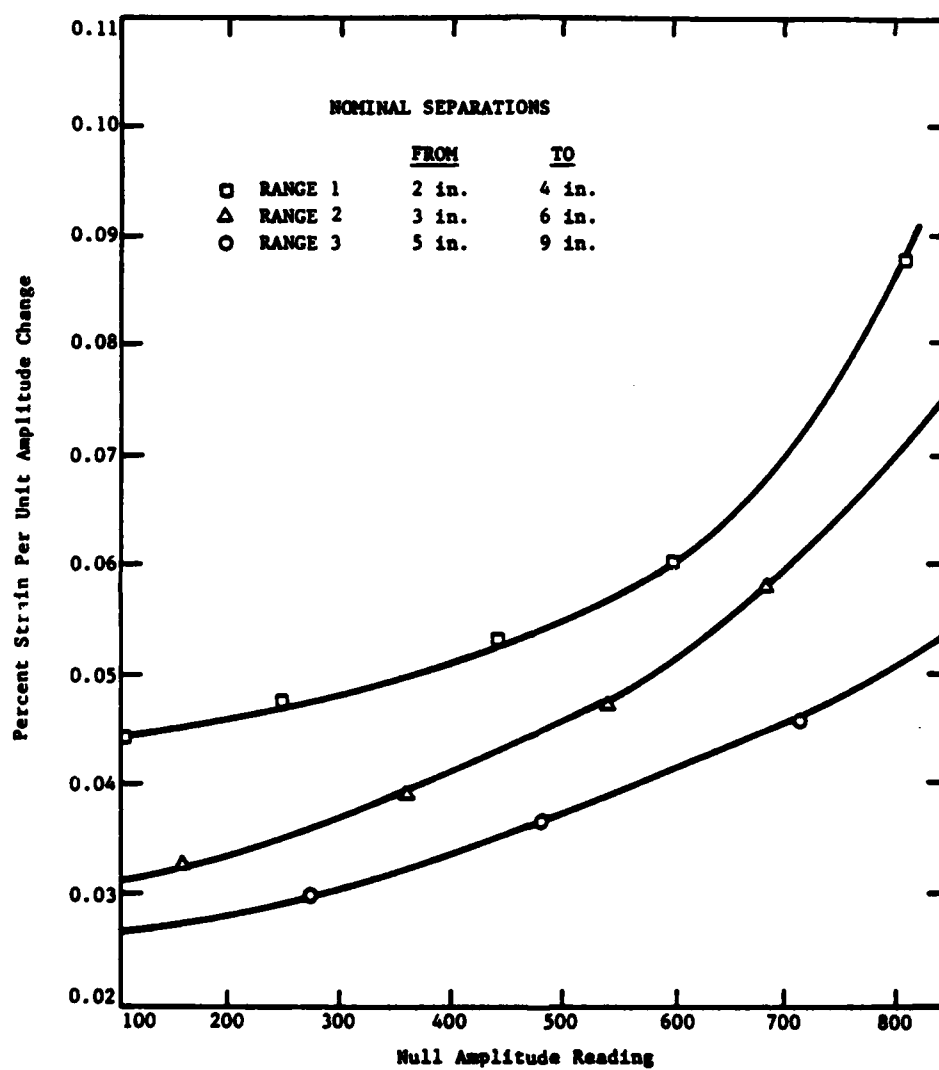


Fig. A.7 - Strain Calibration for Strain Sensor SN-8

## REFERENCES

1. Bachman, R.T. (1983), "Elastic Anisotropy in Marine Sedimentary Rocks," Journal of Geophysical Research, Vol. 88, No. B1, pp. 539-545, January 10, 1983.
2. Beckwith, T.G., Buck, N.L. and Marangoni, R.D. (1981), Mechanical Measurements, Addison-Wesley, 730 pp.
3. Desai, C.S. and Christian, J.T. (1977), Numerical Methods in Geotechnical Engineering, McGraw-Hill, 783 pp.
4. Drnevich, V.P. (1975), "Constrained and Shear Moduli for Finite Elements," Journal of the Geotechnical Engineering Division, ASCE, Vol. 101, No. GT5, May 1975, pp. 459-473.
5. Hardin, B.O. (1978), "The Nature of Stress-Strain Behavior of Soils," Proceedings of the Earthquake Engineering and Soil Dynamics Conference, ASCE, Pasadena, CA, June 19-21, 1978, Vol. I, pp. 3-90.
6. Hardin, B.O. and Drnevich, V.P. (1972a), "Shear Modulus and Damping in Soils: Measurement and Parameter Effects," Journal of the Soil Mechanics and Foundations Division, ASCE, Vol. 98, SM6, June, pp. 603-624.
7. Hardin, B.O. and Drnevich, V.P. (1972b), "Shear Modulus and Damping in Soils: Design Equations and Curves," Journal of the Soil Mechanics and Foundations Division, ASCE, Vol. 98, No. SM7, July, pp. 667-692.
8. Hardin, B.O. and Richart, F.E., Jr. (1963), "Elastic Wave Velocities in Granular Soils," Journal of the Soil Mechanics and Foundations Division, ASCE, Vol. 89, No. SM1, February, pp. 33-65.
9. Haupt, W.A. (1973), Discussion of "In Situ Shear Wave Velocity by Cross-Hole Method," Journal of the Soil Mechanics and Foundation Division, ASCE, Vol. 99, No. SM2, February, pp. 224-228.
10. Hoar, R.J. and Stokoe, K.H., II (1978), "Generation and Measurement of Shear Waves in Situ," Dynamic Geotechnical Testing, ASTM STP 654, pp. 3-29.
11. Knox, D.P., Stokoe, K.H., II, and Kopperman, S.E. (1982), "Effect of State of Stress on Velocity of Low-Amplitude Shear Waves Propagating Along Principal Stress Directions in Dry Sand," Geotechnical Engineering Report GR82-23, Civil Engineering Department, The University of Texas at Austin.

12. Kopperman, S.E., Stokoe, K.H., II, and Knox, D.P. (1982), "Effect of State of Stress on Velocity of Low-Amplitude Compression Waves Propagating Along Principal Stress Directions in Dry Sand," Geotechnical Engineering Report GR82-22, Civil Engineering Department, The University of Texas at Austin.
13. Lee, S.H., Stokoe, K.H., II, and Chu, H.Y. (1984), "Effects of Structural and Stress Anisotropy on Velocity of Low-Amplitude Shear Waves Propagating Along Principal Stress Directions in Dry Sand," (In Progress).
14. Mulilis, J.P., Seed, H.B., Chan, C.K., Mitchell, J.K. and Arulanandan, K. (1977), "Effects of Sample Preparation on Sand Liquefaction," Journal of the Geotechnical Engineering Division, ASCE, Vol. 103, No. GT2, Feb. 1977, pp. 91-108.
15. Podio-Lucioni, A. (1968), "Experimental determination of the dynamic elastic properties of anisotropic rocks, ultrasonic pulse method," Ph.D. Thesis, University of Texas at Austin, 1968.
16. Richart, F.E., Jr., Hall, J.R., Jr., and Woods, R.D. (1970), Vibrations of Soils and Foundations, Prentice-Hall, 414 pp.
17. Suddhiprakarn, C., Roesset, J.M. and Stokoe, K.H., II, (1983), "Effects of Rigid Inclusions on Wave Propagation," Geotechnical Engineering Report GR 83-3, Civil Engineering Department, The University of Texas at Austin.
18. Woods, R.D. (1978), "Measurement of Dynamic Soil Properties," Proceedings of the Earthquake Engineering and Soil Dynamics Conference, ASCE, Pasadena, CA, June 19-21, 1978, Vol. I, pp. 91-178.

**END**

**FILMED**

**4-85**

**DTIC**